

Czech Technical University in Prague
Faculty of Information Technology
Department of Digital Design



**Physical Fault Injection and Monitoring Methods
for Programmable Devices**

by

Tomáš Vaňát

A dissertation thesis submitted to
the Faculty of Information Technology, Czech Technical University in Prague,
in partial fulfilment of the requirements for the degree of Doctor.

Dissertation degree study programme: Informatics

Prague, February 2017

Supervisor:

doc. Ing. Hana Kubátová, CSc.
Department of Digital Design
Faculty of Information Technology
Czech Technical University in Prague
Thákurova 9
160 00 Prague 6
Czech Republic

Co-Supervisor:

RNDr. Jozef Ferencei, CSc.
Department of Nuclear Spectroscopy
Nuclear Physics Institute of the
Czech Academy of Sciences
Řež 130
250 68 Řež
Czech Republic

Copyright © 2017 Tomáš Vaňát

Abstract

With continuously decreasing dimensions of electronic chips, their sensitivity to the effects caused by ionizing radiation increases. Quantification of this sensitivity is an important parameter for electronics which is being used in areas with increased ionizing radiation background and recently, it is gaining importance also for commercial chips. This thesis deals with methods how such devices can be tested using accelerated beams of particles, simulating the effects caused by the ionizing radiation over a whole lifespan of these devices in a reasonably short time.

A method of detecting faults for evaluating the fault cross section of any field programmable gate array (FPGA) was developed and is described in the thesis. The incidence of single event effects in FPGAs was studied for different probe particles (proton, neutron, gamma) using this method. The existing accelerator infrastructure of the Nuclear Physics Institute in Rež was supplemented by more sensitive beam monitoring system to ensure that the tests are done under well defined beam conditions. The bit cross section of single event effects was measured for different types of configuration memories, clock signal phase and beam energies and intensities. The extended infrastructure served also for radiation testing of components which are planned to be used in the new Inner Tracking System (ITS) detector of the ALICE experiment and for selecting optimal fault mitigation techniques used for securing the design of the FPGA-based ITS readout unit against faults induced by ionizing radiation.

Keywords:

FPGA, dependability, single event effect, SEE, single event upset, SEU, accelerated lifetime testing, ALT, bit cross section, proton beam monitoring, dose, radiation hardness test, ALICE ITS Upgrade.

Acknowledgements

First of all, I would like to express my gratitude to my dissertation thesis supervisor Hana Kubátová, co-supervisor Jozef Ferencei and Filip Křížek. They have been a constant source of encouragement and insight during my work and helped me with numerous problems and professional advancements.

Special thanks go to the whole staff of the NPI cyclotron in Řež, led by Jan Štursa, the FNG team led by Milan Štefánik, people participating in the ITS Upgrade Project and summer students and colleagues at NPI in Řež, who were participating in the project.

I would also like to express thanks to my colleagues from Digital Design and Dependability group for their valuable comments, advices and help.

Finally, my greatest thanks go to my family members and especially to my beloved girlfriend, for their infinite patience and care.

Measurements were carried out at the CANAM infrastructure of the NPI ASCR Rez supported through MŠMT project No. LM2011019, id 60 and 313. The work has been also supported by the following grants: LM2015058, GA16-05179S, GA102/09/1668, LG15052 and internal grants of the university (SGS)

Contents

Abbreviations	vii
1 Introduction	1
1.1 Programmable Hardware and Ionizing Radiation	1
1.2 Motivation	2
1.3 Problem Statement	3
2 Background	5
2.1 Programmable Hardware - FPGAs	5
2.2 Ionizing Radiation	10
2.2.1 Radiation Related Quantities and Units	10
2.2.2 Energy Loss of Proton in Matter	13
2.3 Radiation-Induced Errors in Programmable Hardware	15
2.3.1 Single Event Effects (SEE)	16
2.3.2 Total Ionizing Dose Effects (TID)	20
2.3.3 Displacement Damage Dose Effects (DDD)	22
2.4 High-Energy Physics	23
2.4.1 CERN	24
2.4.2 ALICE	25
2.4.3 ITS Upgrade	27
2.5 Cyclotron	32
2.5.1 General Principle of Cyclotron Operation	33
2.5.2 U-120M Principle of Operation	34
2.6 Fast Neutron Generator	40
2.7 Gamma Source	40
2.8 Used Equipment and Tools	43
2.8.1 Ionization Chamber	43
2.8.2 Timepix	44
2.8.3 Simulations	45

3	Related Work	47
3.1	Beam Monitoring	47
3.2	FPGA Radiation Testing	48
3.3	Fault-Tolerant Design Techniques	49
4	NPI Infrastructure Extensions	51
4.1	Target Setup for Proton Irradiation	51
4.1.1	Energy and Beam Profile Adjustment	54
4.1.2	Flux Measurement	60
4.1.3	Estimation of the Energy Loss in Target Silicon Chip	64
4.2	Target Setup for Neutron Irradiation	66
4.2.1	Initial Calibration Measurement	67
4.3	Target Setup for Gamma Irradiation	69
5	Dependability and Characterization Measurements	71
5.1	SEE in FPGAs	71
5.1.1	Testing Circuit Design	71
5.1.2	SEE Measurements	75
5.1.3	Total Dose Effects	81
5.1.4	Discussion of Results from FPGA Measurements	82
5.2	ITS Readout Unit Tests	85
5.3	ALPIDE Measurements	85
5.3.1	Delay Scan	85
6	Conclusions	91
6.1	Contributions of the Dissertation Thesis	92
6.2	Future Work	93
	Bibliography	95
	Reviewed Publications of the Author Relevant to the Thesis	105
	Remaining Publications of the Author Relevant to the Thesis	107
	Remaining Publications of the Author	109

Abbreviations

ALICE	A Large Ion Collider Experiment
ALPIDE	ALICE Pixel Detector
ASIC	Application-Specific Integrated Circuit
BJT	Bipolar-Junction Transistor
BT	Bismaleimide Triazine
CANAM	Center of Accelerators and Nuclear Analytical Methods
CERN	Conseil Européen pour la Recherche Nucléaire European Organization for Nuclear Research
CLK	Clock (signal)
CMOS	Complementary MOSFET, Technology of logical circuits implementation
CPLD	Complex Programmable Logic Device
DDD	Displacement Damage Dose
DFP	D Flip-Flop
FET	Field-Effect Transistor
FF	Flip-Flop
FNG	Fast Neutron Generator
FPGA	Field Programmable Gate Array
GND	Ground (potential)
HDL	High-level Description Language
HEP	High-Energy Physics
IB	Inner Barrel (of ITS)
IC	Integrated Circuit
ITS	Inner Tracking System
JTAG	Joint Test Action Group
kerma	Kinetic Energy Released per unit Mass
LET	Linear Energy Transfer
LHC	Large Hadron Collider
LINAC	Linear Accelerator
LVDS	Low Voltage Differential Signal

ABBREVIATIONS

LUT	Look-Up Table
MAPS	Monolithic Active Pixel Sensor
MBU	Multiple Bit Upset
MOS	Metal-Oxide-Semiconductor
MOSFET	Metal-Oxide-Semiconductor Field-Effect Transistor
NIEL	Non-Ionizing Energy Loss
NMOS	MOSFET with N-type conductive channel (on P bulk)
NPI	Nuclear Physics Institute of the Czech Academy of Sciences in Řež
OB	Outer Barrel (of ITS)
p	Proton
PCB	Printed Circuit Board
PKA	Primary Knock-on Atom
PLA	Programmable Logic Array
PMMA	Poly methyl methacrylate (Acrylic glass)
PMOS	MOSFET with P-type conductive channel (on N bulk)
PMT	Photomultiplier
QCD	Quantum Chromodynamics
QGP	Quark-Gluon Plasma
RF	Radio Frequency
RST	Reset (signal)
RU	Readout Unit
SEB	Single Event Burnout
SEE	Single Event Effect
SEFI	Single Event Functional Interupt
SEGR	Single Event Gate Rupture
SEL	Single Event Latch-up
SET	Single Event Transient
SEU	Single Event Upset
SHE	Single Hard Error
SRAM	Static Random Access Memory
TID	Total Ionizing Dose
VCC	Collector Voltage (power supply potential in BJT technology)
VDD	Drain Voltage (power supply potential in FET technology)

Introduction

The work on this dissertation thesis began as a research in the field of dependability of programmable hardware. The initial problem was to find out which types of faults can be observed in the real life of FPGAs and how do they differ from assumptions, which are being widely used for verifying fault-tolerant design techniques. Due to proposed methods of testing, the subject of the thesis is related not only to programmable hardware and dependability but also to the field of nuclear physics and particle accelerators. Besides dependability studies of FPGAs in radiation environment, the work on the thesis required to build and develop an infrastructure for tests in the environment of ionizing radiation. The infrastructure was used also for testing of components for actual projects, where such tests were required.

1.1 Programmable Hardware and Ionizing Radiation

Programmable hardware in general is a digital electronic circuit which function is determined by a content of its configuration memory. That memory can be only one-time programmable, or reprogrammable, which allows the electronic circuits to be reconfigured during their lifetime. Information in the reprogrammable memory is usually stored in a form of an electric charge defining its output state. Based on the architecture, there are many types of programmable logic circuits, like PLA (Programmable Logic Array), CPLD (Complex Programmable Logic Device), but at present, the most advanced and probably the most used are Field Programmable Gate Arrays (FPGA), which will also be the main concern of this thesis. With decreasing dimensions of transistors in these integrated circuits, the amount of electric charge needed to change their state decreases. That generally makes the circuits more vulnerable to ionizing radiation.

Ionizing radiation is a stream of particles which have the ability to ionize matter, i.e. their kinetic energy is high enough to separate electrons from atoms — ionize them. It can ionize directly through the electromagnetic interaction or indirectly, when directly ionizing radiation is emitted after an interaction of an electrically neutral particle in material. The most common types of indirectly ionizing particles are neutrons and photons. Ionizing

radiation naturally comes to the Earth from the Space in a form of cosmic rays, it is generated in decays of naturally abundant radionuclides, or can be made artificially, for example in particle accelerators, nuclear reactors and X-ray machines.

If ionizing radiation penetrates into an electronic chip, where information is kept in a form of electric charge, it causes that multitude of new charge carriers is created. That might then affect the function of the electronic circuit. This effect is commonly called a Single Event Effect (SEE) and can be further classified in several categories. One of them is a bit flip in a memory, called Single Event Upset (SEU). Single Event Effects are usually reversible, unless they bring a circuit into an undefined state, causing a damage to a component which was not designed to sustain such a condition. The ionizing radiation can also change mechanical and electrical characteristics of the material, which can result in changing of a threshold voltage, timing characteristics or dielectric strength. These effects are usually irreversible and permanent. In a common environment, these effects are very rare and can be ignored in most of applications.

Radiation tolerant electronics must be used in applications, where higher intensity of ionizing radiation is expected and where its failure can have fatal consequences. This includes e.g. space applications, aircraft electronics and electronic devices used in high-energy physics experiments. This is also the case of experiments that are placed at the Large Hadron Collider (LHC) in CERN [1]. The LHC experiments have detectors and associated electronics placed around the points where two beams of protons or heavy ions with energies of several TeV collide. Thereat a lot of high-energy particles capable of direct and indirect ionization is produced. All detector components and electronics have to be selected and designed considering the high radiation load and tested for the expected doses.

1.2 Motivation

Since 2012, I have been involved in the project of ALICE Inner Tracking System (ITS) Upgrade [2], participating in the working groups responsible for development of electronics and silicon sensors. ALICE [3] is a large high-energy physics experiment located at the LHC accelerator in CERN [1]. In 2020, the ALICE collaboration plans to replace its current inner tracker detector with a new silicon pixel detector. The new ITS detector will consist of seven coaxial cylindrical layers of pixel sensors, surrounding the point of collisions. The project of the new detector aims to improve the tracking precision, increase the data readout speed and lower the material budget. The readout electronics of the new ITS will be placed close to pixel sensors, in the high-radiation area, to minimize the cable length because of the signal distortions and to lower the power consumption of the signal drivers. The requirements for fast data readout and processing, reconfigurability, small series and reasonable price results in using an FPGA chip as a main component of the readout system.

All electronic components of the ITS detector and readout unit have to be tested for radiation hardness. Especially for FPGAs and other components prone to SEE, it is necessary to know the SEE rate in the target environment, so that the firmware design

techniques can be adjusted to the expected types of faults and their rate. The possible way how to test the components and measure SEE rates is using accelerated life testing methods and fault injection techniques generating faults, that are expected to occur during the real operation.

The Nuclear Physics Institute of the Czech Academy of Sciences in Řež (NPI) offers an infrastructure for irradiation using beams of high-energy protons or neutrons. However, at the time when I started to work on the project, there were several limitations, which made the testing complicated. There was a complete absence of on-line monitoring and dosimetry for the required range of proton beam intensities necessary for radiation hardness studies of electronics, absence of easy sample positioning and remotely controlled manipulation, absence of automated beam stopping, energy adjustment etc.

The significant part of the presented work is devoted to realization of suitable hardware and software environment for reliable accelerated life testing (ALT). Detailed description of this environment together with experience gained during a few years of its development is provided. This should allow the continuation of electronics radiation hardness studies supported by the on-line dosimetry in the future and make the infrastructure attractive also for other potential users. The other part of this work is devoted to testing electronic components using the existing infrastructure and developed extensions.

1.3 Problem Statement

Goals of this thesis can be summarized as follows:

- Develop a method how to measure single event effects cross section and radiation hardness in FPGAs. The methods should be as close to real environment as possible, should be usable for any FPGA and should allow to measure SEE cross section in the configuration memory and D-flip-flops separately. Such characteristics of an FPGA are useful for developers of fault-tolerant systems, especially in radiation environment.
- Develop a dosimetry system for measuring low proton fluxes at the NPI cyclotron within the range of energies available there. Low proton flux below $10^7 \text{ cm}^{-2} \text{ s}^{-1}$ is needed for testing delicate electronic components and the existing cyclotron monitoring is not sensitive enough to measure them.
- Verify both the dosimetry system and the FPGA testing methods by experiments.
- Compare the behavior of FPGAs based on different technologies in radiation environment.

Background

This chapter reviews basic theoretical concepts of Field-Programmable Gate Arrays (FPGA). In order to have better understanding how ionizing radiation affects FPGAs, we give a short overview about ionizing radiation, its interaction with matter and its dosimetry. Used equipment and tools are also introduced.

2.1 Programmable Hardware - FPGAs

An FPGA is an advanced logic circuit, which can be programmed to perform any combinatorial or sequential logic function [4, 5]. The basic building blocks of an FPGA are look-up tables (LUT), D-flip-flops (DFF) and a routing network with switches. The look-up table represents any combinatorial function of n boolean variables, where n is the number of LUT's inputs. The implementation of a LUT is usually a memory with 1-bit wide data stored and 2^n address space. A typical number of LUT inputs in nowadays chips is four or six, but other versions are also possible. The D-flip-flops are used as memory elements for creating sequential circuits. Usually a LUT and a DFF are physically adjacent elements creating a basic logic cell. Such a cell is shown in Fig. 2.1. Inputs of the LUT (A, B, C and D) correspond to variables of the represented function. Its output (LUT-OUT) can be direct, or can be used as an input (D) of the DFF. This DFF input can be brought in also directly from the routing network (FF-D), depending on the multiplexer settings (BYPASS-LUT). DFF has a clock input (CLK) that can be enabled or disabled (FF-EN) and the data output (FF-OUT) that can be forced to 1 (SET) or to 0 (RESET), which is often used to define the initial state. The real logic cells in modern FPGAs can be much more complex [6].

The described architecture, however, is not the only possible. For example the logic cell of the flash-based ProASIC3 device from Microsemi [7] (formerly Actel) shown in Fig. 2.2 can act either as a LUT with 3 inputs X1, X2 and X3, or as a latch with a clear or set input, or as a D-flip-flop with an enable and clear or set inputs, depending on the state of configurations switches.

2. BACKGROUND

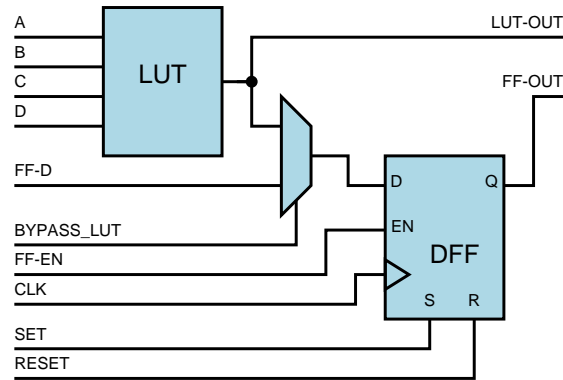


Figure 2.1: Simplified schematics of a logic cell of a generic FPGA. See text for explanation.

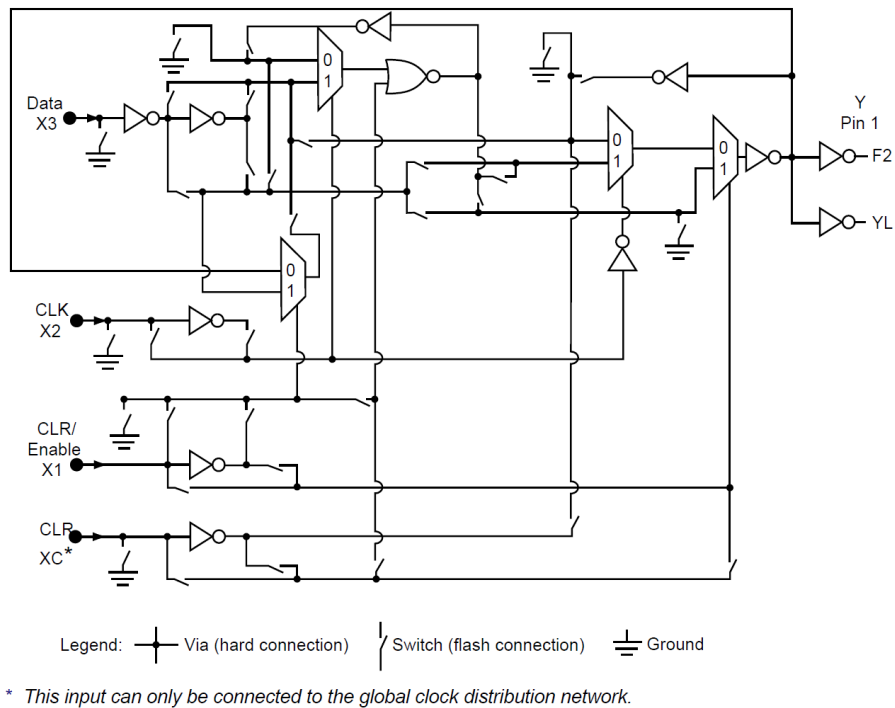


Figure 2.2: Alternative architecture of a logic cell, used in the ProASIC3 chip. See text for details. Credit: [7].

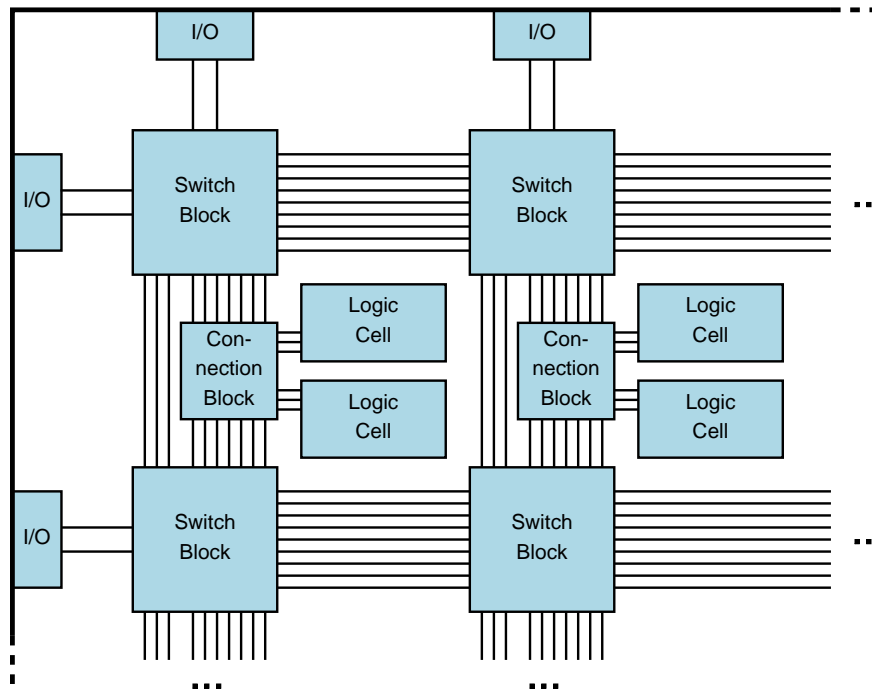


Figure 2.3: Simplified schematics of a generic, the so-called island FPGA topology. Logic cells are connected to a routing network through connection blocks. Switch blocks define the interconnection of the routing network and input/output pins of the chip.

A few basic logic cells are usually grouped together. The group is connected to a routing network that can conduct signals¹ all over the chip, as shown in Fig. 2.3. This forms a massive regular structure that can create any logical circuit, for which there are enough resources in the chip. Modern FPGAs contain also various types of specialized blocks like multipliers, digital signal processing cores, block memories, communication interfaces, clock management and many others performing some frequently used functions that would be hard, inefficient or even impossible to implement using the standard FPGA fabric [5]. By efficiency is meant higher speed, lower power consumption and lower area occupancy. Blocks impossible to implement in the FPGA fabric are e.g. those processing analog signals or those requesting a special timing characteristics.

The function of each element and their interconnection is determined by programmable switches. Their configuration is loaded into the FPGA chip usually using JTAG [8] or some other suitable interface. The configuration file is often called a bitstream, because of its structure — it is a sequence of bits, representing states of the programmable switches in a

¹By a signal is meant an interconnection of different elements. Depending on their type, signals can gain different values, typically represented by a voltage level. For example a logic signal can be either false or true, represented by a zero or a power supply voltage level. An implementation of the signal is a conductive path, i.e. a wire.

defined order. The bitstream is typically prepared from a circuit description in a high-level description language (HDL) and a set of constraints on timing, I/O pin assignment, their configuration, etc. Specialized software tools provided either by chip vendors or third-party companies are used for this purpose. The process of converting the description of the circuit into a bitstream is done in several steps and its complexity grows exponentially with the circuit size — it is a so-called NP-complete problem [9]. Thus, heuristic methods are used to for this purpose and performance of bitstreams generated from the same source by different tools may vary.

Depending on the implementation of programmable switches, there are currently three types of FPGAs available on the market [6]:

- *SRAM-based* [5]: Switches are implemented as a pass transistors or a multiplexers controlled by the state of a Static Random Access Memory (SRAM) bit. The configuration needs to be loaded from a nonvolatile, usually external memory every time the chip is powered on. In some FPGAs, the configuration memory can be partially or completely changed on request during the operation [10]. One of the possible implementations of a configuration switch is shown in Fig. 2.4.
- *Flash-based* [11, 12]: Switches are a floating gate transistors that can be turned off by injecting charge onto the floating gate. Turning it back on is possible by erasing (turning back on) a whole block of transistors and programming the block again. The number of erase cycles is limited, depends on the particular technology and can be in the range of tens or hundreds of thousands erase cycles. The configuration remains stored even after powering the chip off and is ready immediately when the chip is powered on. A floating gate transistor switch used in Microsemi flash-based FPGAs is shown in Fig. 2.5.

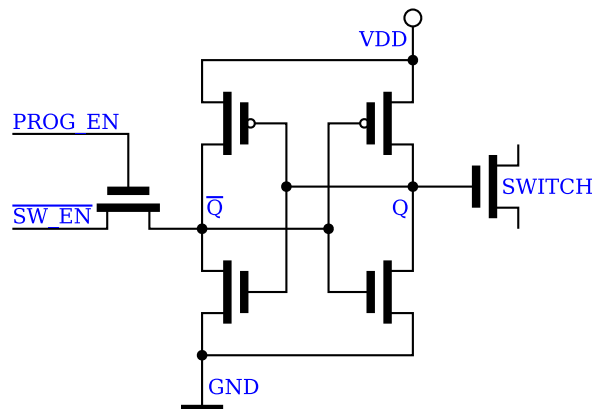


Figure 2.4: Possible realization of a configuration switch in a SRAM-based FPGA, based on a 5-transistor SRAM cell [13]. The value of the $\overline{SW_EN}$ signal is stored up in a cell of 4 transistors when the $PROG_EN$ input is active. The gate of the $SWITCH$ transistor is then driven with a negation of the stored value.

- *Antifuse-based* [14]: A switch is turned on using a high-current pulse which creates a low resistance path in a polysilicon pads between two metal layers. This process is irreversible, so an antifuse based device is one-time programmable only. Naturally, the configuration remains when the chip is powered off. A structure of an antifuse device is shown in Fig. 2.6.

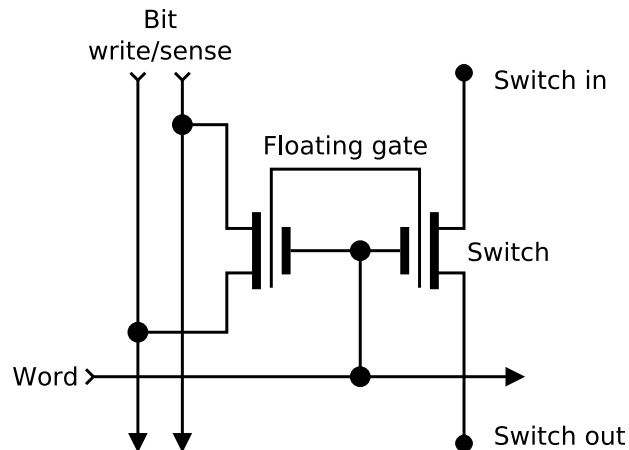


Figure 2.5: The right-hand side transistor is a floating gate controlled switch. Programming of the floating gate is done through the left-hand side transistor. Credit: [7].

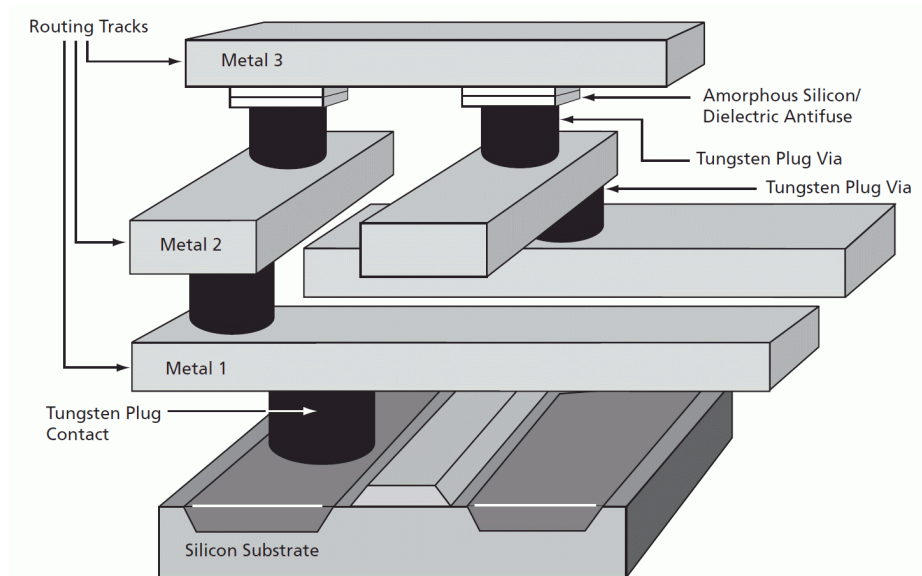


Figure 2.6: Interconnection structure in an antifuse device. The top metal layer is connected via one-time programmable antifuse switches. Source: [15].

2.2 Ionizing Radiation

Ionizing radiation is formed by particles which are able to ionize atoms. The underlying mechanism how the radiation interacts with the matter depends on the type and energy of ionizing particles as well as on the properties of the target material. According to the way how the ionizing radiation interacts with matter, ionizing radiation can be divided into two groups: directly ionizing radiation and indirectly ionizing radiation.

Directly ionizing radiation [16] is formed by charged particles, e.g. α , β , protons, deuterons or ions. When these particles pass through the matter, they deliver their energy mostly to electrons in the matter. If the transferred energy is higher than the binding energy of an electron, it can be released from the atom, creating a pair of free electron and an ion. If the delivered energy is less than the binding energy, it excites the electron to a higher energy level.

Indirectly ionizing radiation [16] is formed by particles without an electric charge, e.g. neutrons or photons. They can transfer their energy by colliding with atoms or another particles only. If the collision is inelastic, a part of the particle's energy is used to excite the atom or nucleus which can then release a charged electron, proton or another particle. Released secondary charged particles are then able to ionize directly.

2.2.1 Radiation Related Quantities and Units

In this section, units and quantities relevant for this thesis are listed and described.

2.2.1.1 Energy

The main principle of ionizing radiation is exchanging energy between particles. The unit of energy according to the International System of Units (SI) is the joule [J]. In particle physics, the electronvolt [eV] is rather used. One electronvolt is defined as the energy gained or lost by a single electron moving across an electric potential difference of one volt. The electron has an elementary charge $e \doteq 1.602 \times 10^{-19}$ C. Volt is joule per coulomb [17]. Thus

$$1 \text{ eV} \doteq 1.602 \times 10^{-19} \text{ C} \times 1 \frac{\text{J}}{\text{C}} \doteq 1.602 \times 10^{-19} \text{ J}. \quad (2.1)$$

2.2.1.2 Stopping Power

The amount of energy lost per unit of distance by a charged particle traveling through the matter is called the Stopping Power S :

$$S = -\frac{dE}{dx} [\text{J m}^{-1}, \text{ eV m}^{-1}], \quad (2.2)$$

where dE is the energy lost by the particle while traversing the distance dx in the matter. It varies for different particles and materials. The stopping power is not constant along the trajectory. Its values for a given material, particle and its energy are experimentally

measured and can be found for example in [18], [19] or [20]. Detailed description of stopping power for protons is presented in Section 2.2.2.

2.2.1.3 Linear Energy Transfer (LET)

Very similar and closely related to the stopping power is the Linear Energy Transfer (*LET*).

$$LET = \frac{dE}{dx}. \quad (2.3)$$

LET is the energy dE imparted to the target material by a charged particle of specified energy per the traversed distance dx . The difference between *LET* and the stopping power is, that *LET* does not include the energy which leaves the target e.g. by radiative losses [21]. So *LET* is only the energy which stays in the target volume, while the stopping power is the total kinetic energy lost by the particle. The sign difference between *S* and *LET* is given by convention, since *LET* relates to the energy accepted by the target material whereas *S* measures the energy loss of the particle projectile.

2.2.1.4 Fluence

The particle fluence Φ is a quantity referring to how many particles (dn) passed through an element of area da

$$\Phi = \frac{dn}{da} [\text{cm}^{-2}]. \quad (2.4)$$

2.2.1.5 Flux

The particle flux F is a fluence per time unit dt :

$$F = \frac{d\Phi}{dt} [\text{cm}^{-2} \text{s}^{-1}]. \quad (2.5)$$

In some applications, charged particle flux is integrated over transverse plane and the resulting particle flow is expressed in terms of a current I in amperes [A], as a transferred charge per time. In such a case one ignores the transverse beam profile. Since $I = \frac{Q}{t}$, where Q is the total charge and t is the time, we can easily recalculate between amperes and particles per second if we know the charge of particles. In case of protons or electrons, the charge is 1.602×10^{-19} C. The expression of the particle flow in terms of a current is obviously not applicable in the case of uncharged particles (e.g. neutrons or gammas).

2.2.1.6 Activity

Activity is an important characteristics of a radioactive source. It determines the number of radioactive decays in the source per one second. The unit of activity is becquerel [Bq] and its dimension is equivalent to s^{-1} or Hz.

The radioactive decay is a stochastic process. The time evolution of the activity of a given source is characterized by a so-called half-life denoted as $T_{1/2}$. It is a period of time,

2. BACKGROUND

during which the activity falls by factor $1/2$. The number of radioactive nuclei in the source N as a function of time t follows the so-called law of radioactive decay:

$$N = N_0 \times 2^{-\frac{t}{T_{1/2}}}, \quad (2.6)$$

where N_0 is the original number of radioactive nuclei in the source at $t = 0$.

2.2.1.7 Dose

Dose (D) is defined as an energy dE absorbed in an element of mass dm ,

$$D = \frac{dE}{dm}. \quad (2.7)$$

In the SI, the unit of dose is the gray [Gy], defined as an absorption of one joule of radiation energy per kilogram of mass.

$$1 \text{ Gy} = 1 \frac{\text{J}}{\text{kg}} = 1 \frac{\text{m}^2}{\text{s}^2}. \quad (2.8)$$

The other frequently used unit for dose is the rad [rad]. The rad is an old unit, defined in the CGS (Centimeter–Gram–Second) system. Despite that, it is still being widely used in the high-energy physics community. The relationship between rad and gray is very simple:

$$1 \text{ rad} = 0.01 \text{ Gy}. \quad (2.9)$$

Related quantity is the dose rate which gives the absorbed dose per unit of time, e.g. [Gy/s] or [rad/s].

2.2.1.8 Equivalent Dose

The unit of equivalent dose (H) is the sievert [Sv] which has the same dimension as the gray.

$$1 \text{ Sv} = 1 \frac{\text{J}}{\text{kg}} = 1 \frac{\text{m}^2}{\text{s}^2} \quad (2.10)$$

The sievert is used in terms of health effects of the absorbed dose on a human body. It respects different effects of various kinds of radiation on biologic tissues. These effects are quantified by means of the so-called quality factor Q (dimensionless), which is used to weight the dose D , obtained by the tissue to get the equivalent dose in sieverts. For photons, electrons and positrons the quality factor Q equals 1 and thus the corresponding equivalent dose is equal to the dose in grays. For protons above 2 MeV, the quality factor is 5, for neutrons it ranges from 5 to 20 depending on their energy. Alpha particles and heavy ions have the quality factor 20 [22].

Again, an equivalent dose rate is also used. The [Sv/hour] unit is used to characterize a health risk when handling radioactive material or as a characterization of radiation environment.

2.2.1.9 Kerma

Kerma (K) stands for Kinetic Energy Released per unit Mass. It is a variation of the dose and is likewise measured in grays [Gy]. It is used mostly in case of non-directly ionizing radiation and it is defined as

$$K = \frac{\sum dE_k}{dm}, \quad (2.11)$$

where $\sum dE_k$ is a sum of initial kinetic energies of all charged particles released by non-charged, indirectly ionizing particles in target material of a mass dm [23].

2.2.1.10 Cross Section

The cross section σ [cm^2] reflects the incidence likelihood of interaction per one beam and per one target particle. It can be interpreted as a size of the sensitive area perpendicular to the direction of incoming point-like particles. Once the area is hit, the reaction (event) occurs. The cross section is defined as

$$\sigma = \frac{N}{F \times n_t}, \quad (2.12)$$

where N is the interaction rate [s^{-1}] at the given particle flux F [$\text{cm}^{-2}\text{s}^{-1}$] and n_t is the number of target particles.

In high-energy physics, cross section is often expressed in terms of a non-SI unit called barn [b]:

$$1 [\text{b}] = 10^{-28} [\text{m}^2]. \quad (2.13)$$

The cross section is used also for the description of the likelihood of an interaction between a beam particle and an electronic device (integrated circuit) causing a single event effect, see Section 2.3.1.

2.2.2 Energy Loss of Proton in Matter

Most of the radiation hardness tests discussed in this thesis were done using proton beam provided by the NPI cyclotron U-120M. Therefore, in this section we describe proton interaction in matter in more detail. The protons can interact in matter by these processes [23]:

- inelastic scattering with atomic electrons of the target material,
- elastic scattering with nuclei of the target material,
- nuclear reaction,
- Cherenkov radiation,
- bremsstrahlung.

2. BACKGROUND

The cyclotron U-120M provides proton beams with energies less than 40 MeV. In this energy domain, the last two listed processes are not relevant for proton energy loss. The process which has the highest probability to take place is the proton interaction with atomic electrons. Since the proton is about 2000-times heavier than the electron, such collisions do not change the direction of the proton momentum significantly. In general, protons can either excite or ionize atoms in the matter depending on the size of momentum transferred in the inelastic collision.

Protons can also interact with nuclei. Since the proton has a mass usually less than the mass of a target nucleus, only a small part of the proton energy is transferred to the recoil of a nucleus. Chances to induce a nuclear reaction grow when the proton energy is high enough to overcome the Coulomb barrier of a nucleus. However, due to the finite range of the nuclear force (\approx fm) and tiny dimensions of nuclei (\approx 10 fm), the probability of a nuclear reaction is much smaller compared to the electromagnetic interaction.

Due to the probabilistic nature of proton interactions in matter, the resulting total energy loss for each proton projectile is randomly distributed. The mean stopping power is to good accuracy parametrized by the Bethe-Bloch formula [24], which takes into account properties of the target material and of the incoming particle,

$$-\frac{1}{\rho} \left\langle \frac{dE}{dx} \right\rangle = K z^2 \frac{Z}{A} \frac{1}{\beta^2} \left[\frac{1}{2} \ln \frac{2m_e c^2 \beta^2 \gamma^2 T_{\max}}{I^2} - \beta^2 - \frac{\delta}{2} \right], \quad (2.14)$$

where ρ is the material density, Z is the proton number of the given material, A is the atomic mass of the material, z is the charge of the incoming particle, $\beta = \frac{v}{c}$ is the ratio of the incident particle velocity and the speed of light, $\gamma = (1 - \beta^2)^{-\frac{1}{2}}$ is the Lorentz factor, m_e is the mass of the electron, T_{\max} is the maximum transferred kinetic energy to a free electron in a single collision, I is the mean excitation energy and δ is a correction for the effects caused by density. The constant K equals

$$K = 4\pi N_A r_e^2 m_e c^2, \quad (2.15)$$

where N_A is the Avogadro number and $r_e = \frac{e^2}{4\pi\epsilon_0 m_e c^2}$ is the classical radius of the electron.

As can be seen from Fig. 2.7, the density normalized stopping power $\left\langle -\frac{dE}{dx} \right\rangle \frac{1}{\rho}$ is about the same for most materials, and gets smaller with Z [17].

The Bethe-Bloch curve has a pronounced minimum at $\beta\gamma \approx 3$. For smaller $\beta\gamma$, the decreasing energy of the projectile particle leads to increase of its stopping power. This behavior is driven by the β^{-2} dependence of $\left\langle -\frac{dE}{dx} \right\rangle \frac{1}{\rho}$. The particle will thus have the largest energy losses close to the end of its trajectory. Let us point out that a 30 MeV proton has $\beta = 0.247$ and $\beta\gamma = 0.255$.

The assumptions under which the Bethe-Bloch formula was derived get invalid for particles with very low velocities and other parameterizations have to be used to describe $\left\langle -\frac{dE}{dx} \right\rangle$. The dependence of the stopping power on the path length exhibits a pronounced maximum close to the end of particle trajectory known as the Bragg peak [25].

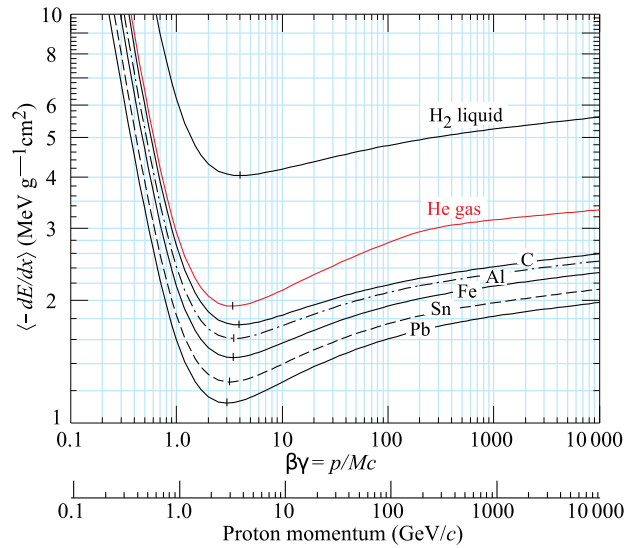


Figure 2.7: Density normalized mean stopping power of protons in liquid hydrogen, gaseous helium, carbon, aluminum, iron, tin, and lead. Credit: [17].

2.3 Radiation-Induced Errors in Programmable Hardware

Radiation in semiconductor electronics can cause following effects [26]:

- Immediate effects induced by a transfer of electric charge to matter by a single particle or by a particle shower, causing unexpected currents, influencing the function of the circuit. We call them single event effects (SEE), they are usually reversible and can be further classified in several categories, which will be described later.
- Long-term effects caused by a gradual degradation of the material due to ionization and interaction of ionizing particles with atoms of the material. These effects cause usually irreversible changes and can be further divided into two categories:
 - Total ionizing dose effects (TID) which result from the ionization that can change e.g. the number of free charge carriers in semiconductor and which can affect e.g. a shift of threshold voltages.
 - Displacement damage dose effects (DDD) which are caused by inelastic collisions of incoming particles with atoms of crystal lattice. These collisions may displace atoms from the crystalline structure or cause a nuclear reaction that changes atoms to other element with different properties.

The discussed characterization of semiconductor electronics related effects follows [27].

2.3.1 Single Event Effects (SEE)

The single event effect is caused by bringing an electrical charge into the depletion layer at the P-N junction of a semiconductor device by ionizing particles. The free electrical charge carriers are created along the trajectory of the ionizing particle. The mean energy needed to create one electron-hole pair in silicon is $w = 3.6 \text{ eV}$ [17]. The mean number of created electron-hole pairs N_p along the trajectory x can be calculated from the Linear Energy Transfer (LET) for a given ionizing particle and target material integrated over that trajectory as follows:

$$N_p = \frac{1}{w} \int LET \, dx. \quad (2.16)$$

However, not all deposited charge influences the circuit. Only the part of it, which is collected by the reverse-biased P-N junction of the semiconductor creates current and voltage spikes that can propagate to the circuit. Their effect depends on factors such as the size of the junction, back-bias voltage, substrate type, material doping etc. An example of a SEE time-flow in an N-channel metal-oxide-semiconductor (NMOS) transistor is shown in Fig. 2.8 and can be described as follows:

- a) A charged particle passes nearby the reverse-biased P-N junction and creates free electron-hole pairs;
- b) Electrons attracted by the positively charged drain are drifting towards it, extending the depletion region and creating a transient current and voltage pulse;
- c) After the initial rapid pulse is over, remaining charge keeps diffusing into the depletion region until it gets collected or recombined;
- d) The last panel shows a time flow of a P-N junction current induced by a SEE. The dashed vertical lines indicate borders between the regimes a), b), c) shown on the corresponding panels.

More information on the mechanism of charge collection, time evolution of the depletion region and time relevant scales can be found in [26, 28].

The sensitivity of a given electronic component (e.g. memory) to the SEE for a specific particle with given energy is expressed in terms of a cross section σ , determining the mean number of SEE events per particle fluence. A device cross section is defined as:

$$\sigma_{\text{device}} = \frac{\varepsilon}{\Phi} [\text{cm}^2]. \quad (2.17)$$

For a memory it is more convenient to define a bit cross section:

$$\sigma_{\text{bit}} = \frac{\varepsilon}{\Phi \times n} [\text{cm}^2 \text{ bit}^{-1}]. \quad (2.18)$$

Here Φ is particle fluence (i.e. the number of particles per unit area), ε is the number of SEE events and n is the number of vulnerable memory bits in the device.

SEE are further divided into several categories, depending on where the charge is deposited and what kind of effect they cause.

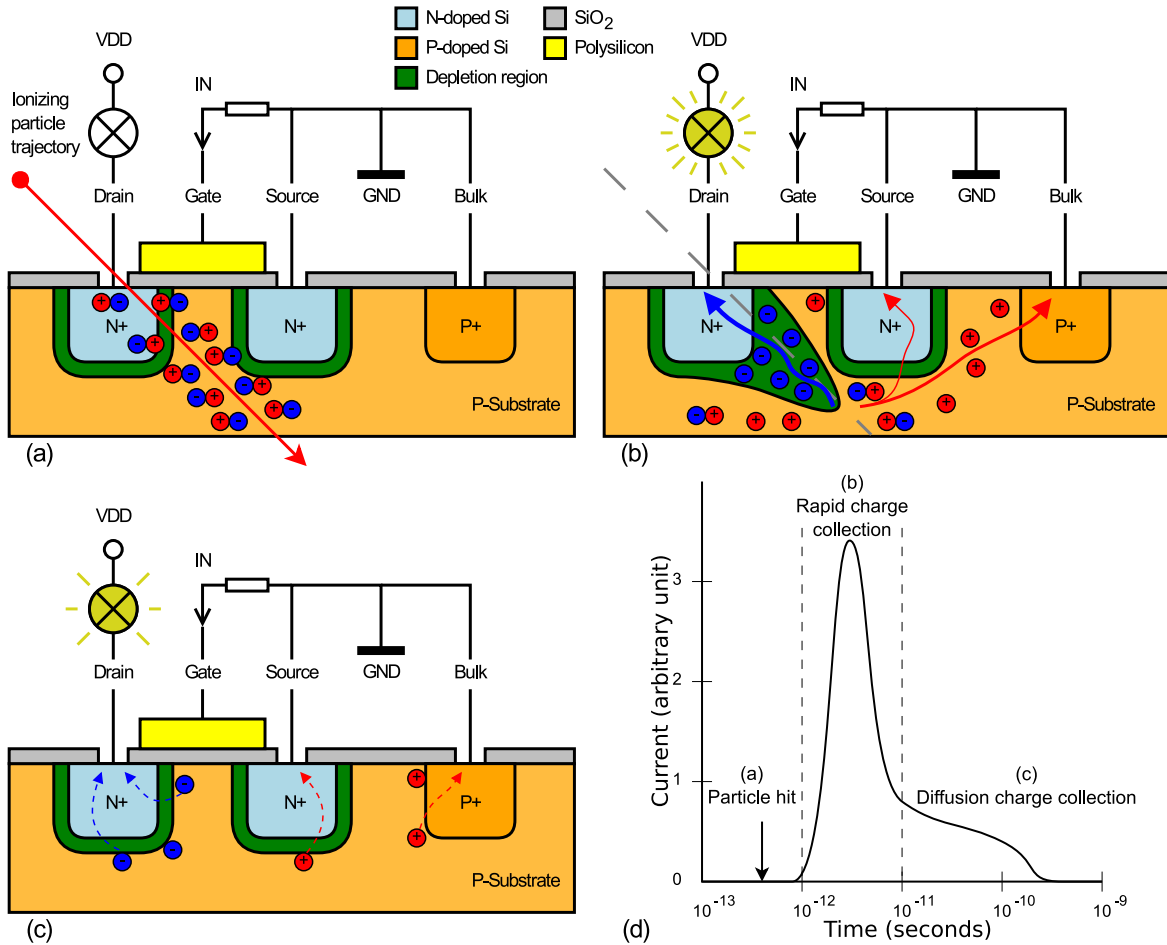


Figure 2.8: Mechanism of a SEE in a NMOS transistor [26]. See text above for detailed description of individual panels.

2.3.1.1 Single Event Transient (SET)

SET is a type of SEE where the deposited charge causes a short voltage glitch followed by a current glitch on a signal connection, which changes its value for some time [29]. It does not affect the stable state of the signal driver, so the signal value returns back to normal condition after the deposited charge goes off. On asynchronous and analog signals, the glitch propagates further through the circuit. On synchronous signals it is often stopped at the next flip-flop, unless it comes at the same time as the clock signal does. Then the wrong signal value can be captured by that flip-flop and in the next clock cycle, the wrong value also propagates further to the circuit.

2.3.1.2 Single Event Upset (SEU)

If the collected charge is greater than the critical charge required to change a state of the flip-flop (e.g. SRAM memory or DFF), and is located in a sensitive transistor of that flip-flop, it causes a change of the value stored in the affected flip-flop. This is called a SEU [26]. The induced flip can happen both from 0 to 1 or from 1 to 0. It is not a destructive event and the correct value can be restored simply by rewriting it back. However, until this is done, the wrong value remains in the memory element and affects the circuit. A principle of changing a bit value in SRAM cell is illustrated in Fig. 2.9 and is following:

- a) A particle hits an off-state transistor;
- b) Charge is collected by the collector of the left-hand side NMOS transistor and creates current I , which charges gates of the right-hand side transistors;
- c) The right-hand side transistors toggle and enable the current to charge the gates of the left-hand side transistors;
- d) The left-hand side transistors toggle and the circuit reaches stable condition.

2.3.1.3 Multiple Bit Upset (MBU)

MBU is induced by the same mechanism as a SEU, but results in more memory bits flipped [27]. MBU can be caused by two or more independent particles as a multiple SEUs coming within one period of resolution, i.e. a clock period or a period of a mechanism that checks the circuit for errors and corrects them. A Single Event Multiple Upset (SEMU) can be considered as a special case of MBU, when multiple bits, typically in physically adjacent memory cells, are flipped as a result of one particle hit. One particle can affect more cells if its trajectory passes through more transistors, or when transistors are too close and the charge deposits to several of them. The high-energy particle can also interact with an atom of the chip matter such that secondary ionizing products of the reaction are spalled over multiple memory cells [30].

2.3.1.4 Single Event Functional Interrupt (SEFI)

SEFI is a special case of any SEE resulting in an interruption or modification of the circuit function. If the SEE affects a stored data only and the circuit keeps working, it is not considered a SEFI. Also when a fault occurs in a fault tolerant system and the system is able to work correctly even with the fault, it is again not a SEFI. However, when the result of a SEE is that the circuit performs an incorrect transaction and stays stuck in a wrong or an undefined state, or the circuit function is changed, it is considered as a SEFI. To restore the function of the circuit, a reset or a reconfiguration has to be done.

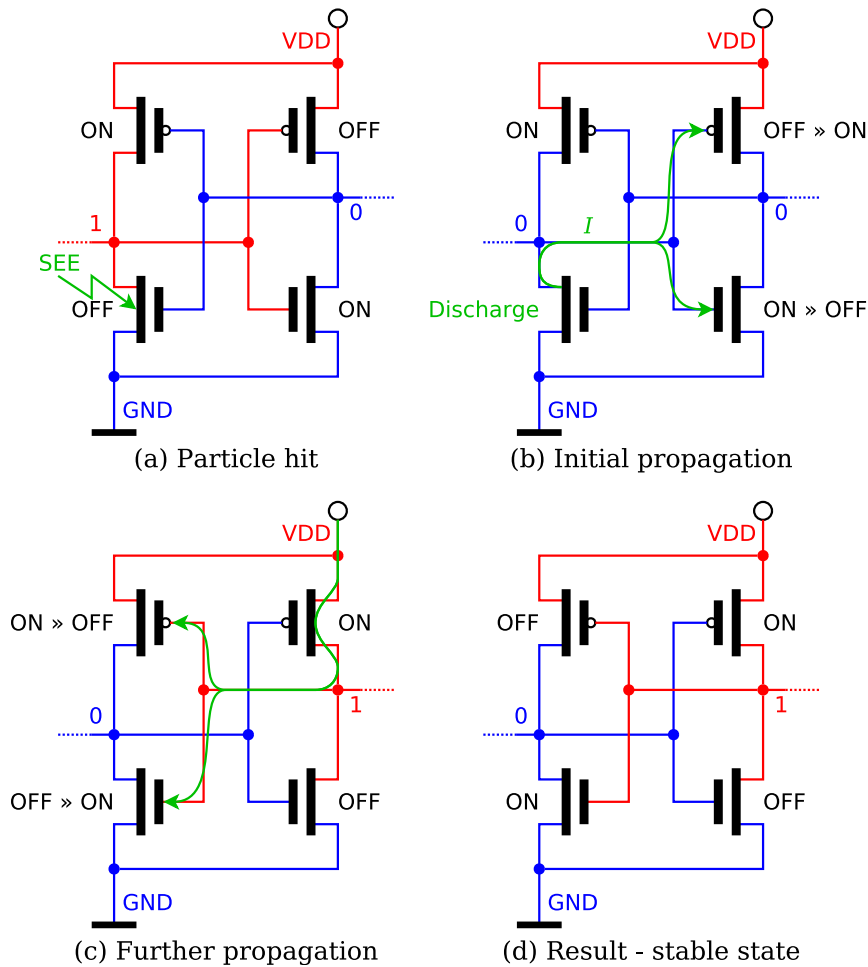


Figure 2.9: Simplified mechanism of a SEU in the SRAM cell [27]. Note, that SEU can be created only when a transistor in the non-conducting state is affected.

2.3.1.5 Single Event Latch-up (SEL)

When ionization is high enough to affect a large area of a parasitic N-P-N-P structure between N-type and P-type transistors, a so-called SEL can occur. The mechanism is illustrated in Fig. 2.10. Because the parasitic structure is similar to a thyristor, once triggered, the structure sustains in a conductive (low-resistance) state because of its positive feedback. When the resistance of the path created between the power supply and the ground is too low and current density exceeds the carrying capacity limits of the path, excessive heat is generated until some part of the path breaks and the circuit gets permanently damaged. If the current path is interrupted before this happens, the latch-up can be recovered. Interruption of the path is done typically by power cycling the chip. When the latch-up occurs within signals, changing the signal value is sufficient. The latch-up can be detected by a sudden increase of the current consumption.

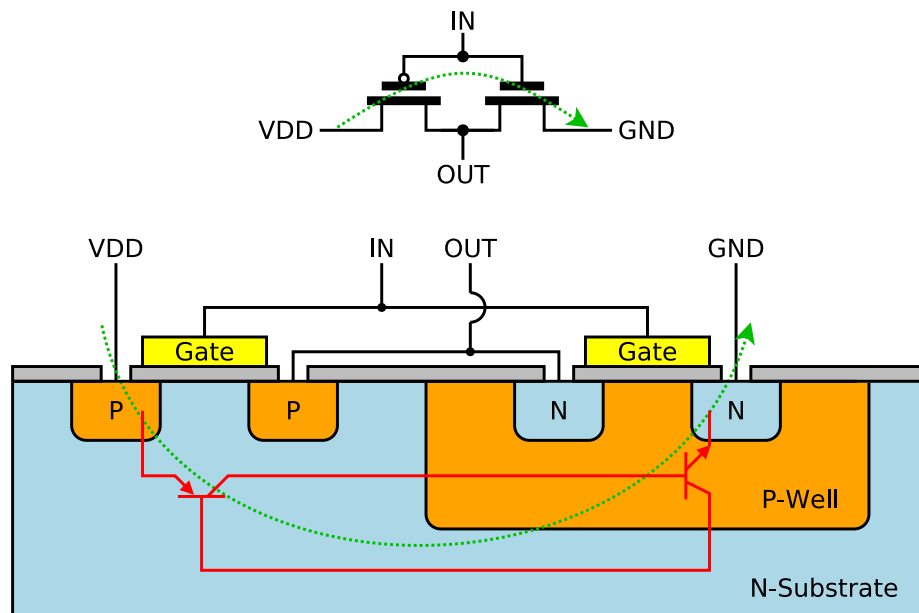


Figure 2.10: Principle of a Single Event Latch-up (SEL) in an inverter. Parasitic transistors are sketched in red and the green arrow is a conductive path through them.

2.3.1.6 Single Hard Error (SHE)

SHE is a common name for a non-recoverable change of the circuit function due to a permanent damage of its part. It can be

- **Single Event Burnout (SEB)** to which for example a destructive latch-up can lead. SEB occurs when the circuit is destructed by excessive heat generated by high current induced by any of the above mentioned errors.
- **Single Event Gate Rupture (SEGR)** which occurs, when the gate oxide breaks. The result is an increased gate leakage current, eventually leading to a complete failure. It is more likely to happen when a particle hits a gate, stressed by a high voltage, e.g. a power MOSFET or an EEPROM/flash transistor during an erase/write operation.

2.3.2 Total Ionizing Dose Effects (TID)

The overall dose delivered to the material by ionizing particles is called the Total Ionizing Dose (TID). The charge created by ionizing radiation can accumulate inside the target material and change its properties. In metal-oxide-semiconductor (MOS) devices, the charge accumulation in the bulk material or the gate oxide creates leakage paths and causes a threshold voltage shift [31]. Since the holes are not as mobile as electrons, they become trapped in the gate oxide, where they gradually increase its positive charge. The

Figure 2.11 shows a non-irradiated PMOS transistor in the *on* state (a), and the same transistor after the critical amount of charge was accumulated in the gate oxide (b). The accumulated charge results in creation of a conducting channel, even when the transistor should be *off*. The result is the same as if additional positive voltage was applied to the gate — in NMOS it lowers the threshold voltage and in PMOS it increases it.

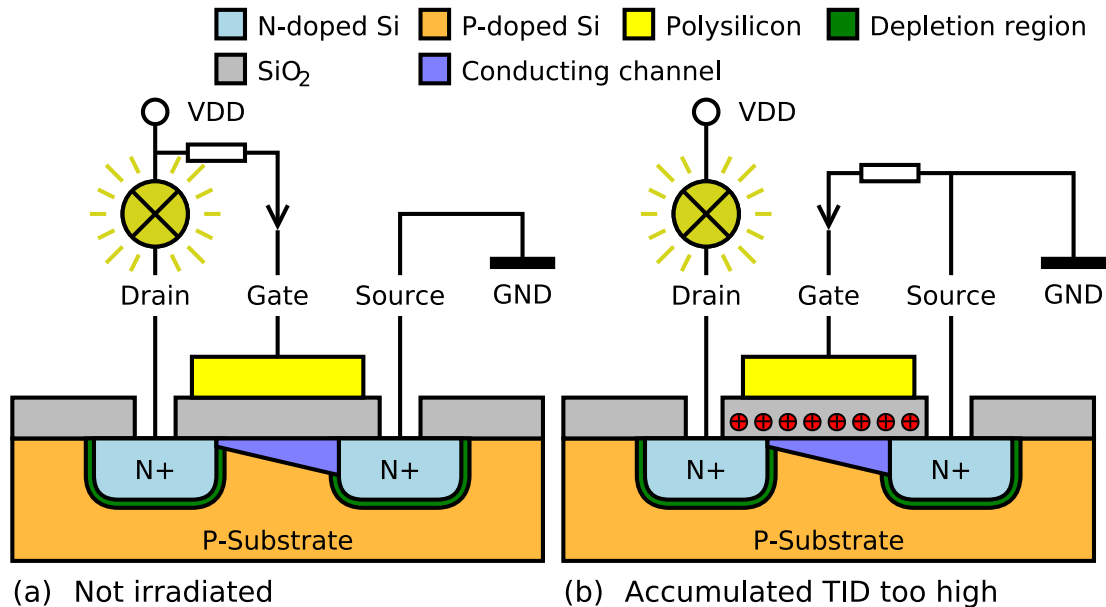


Figure 2.11: Schematic of the non-irradiated N-channel transistor in a regular *on* state (a) and a radiation-induced charge trapped in the gate oxide, which keeps the transistor *on* even when the gate-source voltage (U_{GS}) is smaller than the original threshold voltage (U_{TH}) and the transistor should be *off* (b).

The material degradation depends among others on the dose rate and voltage applied during irradiation. Although an annealing process, when the trapped charge slowly diffuses away from the gate oxide, can be observed, TID damage is considered as irreversible. The annealing is never complete. Main contributing particles to TID are protons, electrons, ions and gamma. Testing the devices for TID hardness is often done by gamma radiation, usually from a ⁶⁰Co source. It is a widely available and cheap source, but since its gamma photons (1173 keV and 1332 keV) cannot cause nuclear reactions in silicon, it tests just the TID hardness. For applications where other types of material damage also matter, a different method has to be used.

TID is quantified in terms of dose and is measured in rads or grays. To calculate the TID from the known particle fluence, we need to know how much energy do particles deposit in the irradiated material. That depends on the particle type, its energy and the length of its trajectory in the target material. The energy deposition can be numerically simulated using software tools such as Geant4 [32] for general geometry, or SRIM [20] for thin layers.

2.3.3 Displacement Damage Dose Effects (DDD)

A displacement damage occurs when a particle penetrates into a crystal lattice of semiconductor and causes a permanent displacement of an atom from its regular position. That leaves an empty position and a surplus atom elsewhere in the crystal, as illustrated in Fig. 2.12. The overall amount of displacement effects is characterized by the displacement damage dose [33].

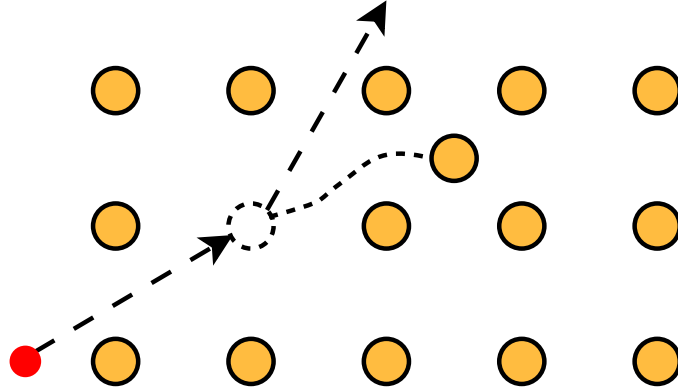


Figure 2.12: Illustration of a displacement damage in a crystalline lattice leading to the interstitial-vacancy pair formation.

The atom released from its position in the lattice by the incident particle is often referred to as a Primary Knock-on Atom (PKA) [23]. PKA creates a vacancy-interstitial pair, which recombines (in 90%), or migrates and forms a stable defect (interstitial, vacancy, divacancy, vacancy-interstitial Frenkel defect or vacancy-interstitial Schottky defect). However, the original PKA can only be displaced when the transferred energy exceeds the binding energy.

The displacement can be caused by neutrons, protons and high-energy electrons and photons. Electrons usually produce isolated point defects, since they are light and can transfer only a small energy to the PKA. With increasing energy of protons (> 10 MeV) and neutrons (> 1 MeV) the chance of an inelastic collision increases. Such interactions can produce a cascade of lattice defects, grouped in clusters. Protons have smaller chance to cause a displacement when compared to neutrons. The majority of proton energy is lost by ionization and thanks to their positive charge they are repelled from the positively charged atomic nucleus by electric forces [34, 23].

The degradation by displacement damage is a long-term process and often has features similar to the TID, although it is based on a different physical mechanism. A typical effect of the DDD is degradation of the bipolar transistor gain and increase of its leakage current, as the places of knocked-out atoms serve as new recombination centers, especially for the minority carriers in the base of bipolar transistors. Also optoelectronic components (LEDs, CCDs, optical sensors, transceivers, optocouplers and solar cells) are very sensitive to the displacement damage [35].

The part of energy deposition of a particle, lost in inelastic collisions with atoms of target material, is expressed in terms of a Non-Ionizing Energy Loss (NIEL) or a displacement damage cross section σ_D [36]. The unit of NIEL is $[\text{keV cm}^2 \text{g}^{-1}]$ and the unit of σ_D is $[\text{MeV mb}]$. NIEL can be also referred to as a displacement kerma. Numerous observations have led to the result that DDD effects by energetic particles in the bulk of any material can be described as being proportional both to NIEL and to σ_D [36]. For silicon, the relation between σ_D and NIEL, using the molar mass of the silicon and the Avogadro constant, is:

$$100 \text{ MeV mb} = 2.144 \text{ keV cm}^2 \text{g}^{-1}. \quad (2.19)$$

The DDD value is often given also as an equivalent fluence of 1 MeV neutrons [1 MeV n eq]. According to [37], 1 MeV neutron in silicon has a value of $\sigma_D = 95 \text{ MeV mb}$ thus its NIEL is $2.037 \text{ keV cm}^2 \text{g}^{-1}$. Displacement damage effects of different particles with given energy can be recalculated to 1 MeV n eq using a hardness factor k , which can be found e.g. in [36]. Figure 2.13 shows a value of this factor for different energy of neutrons. For some applications, 1 MeV electron or 10 MeV proton equivalent fluence is also used. Irradiation tests for DDD can be performed by neutrons or, if ionization damage does not matter, by protons.

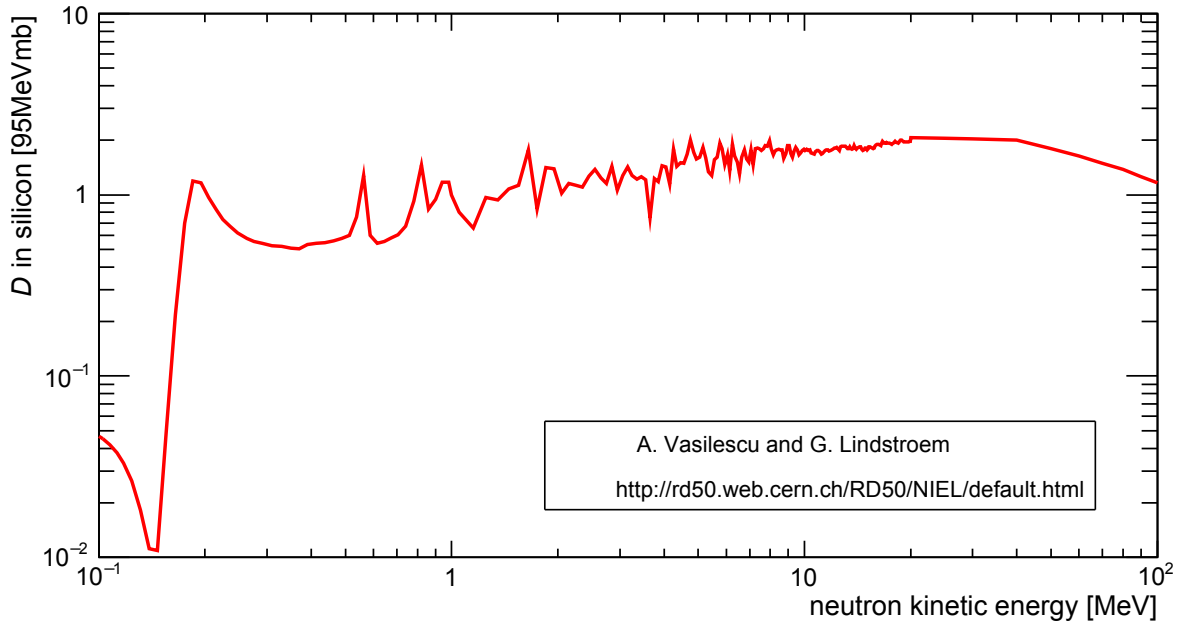


Figure 2.13: Displacement damage of neutron in silicon as a function of neutron kinetic energy, normalized to 1 MeV n eq. Data from [36].

2.4 High-Energy Physics

The environment of physics experiments, especially in the high-energy physics, can be very unfriendly to electronics due to high radiation background, magnetic fields, electromagnetic interference, temperature (high or low) and other environmental parameters deviating from the common conditions where most of electronic devices are intended to operate. Thus a preparation of these experiments requires usage of special electronic components, special design techniques and a lot of testing. In this section we will describe the LHC and the related CERN accelerator complex, the ALICE experiment and its Inner Tracking System.

2.4.1 CERN

The European Organization for Nuclear Research (CERN) is one of Europe's first joint ventures. At present, CERN has 22 member states. The organization provides an infrastructure for research, focused primary on fundamental questions in physics of the micro-world. Thus it is often referred to as the European Laboratory for Particle Physics. Numerous experiments and facilities are run here for this purpose, including the world's largest accelerator — 27 km long circular Large Hadron Collider (LHC) [1]. The purpose of a particle collider is to study internal particle structure and relevant interactions. With increasing energy of the particles, their so-called de Broglie wavelength gets shorter. Shorter wavelength of particles then allows more detailed resolution of their inner structure, when they collide. LHC is able to accelerate protons or lead ions to kinetic energies in order of TeV. Two counter-rotating particle beams cross each other in 4 points of collisions, around which experiments called ALICE, ATLAS, CMS and LHCb are built. ATLAS and CMS study the Higgs boson properties and search for physics beyond the Standard Model. LHCb is oriented on physics in the b quark sector. ALICE investigates properties of the quark-gluon plasma — a state of matter which is believed to have existed in the early Universe, about 1 μ s after the Big Bang.

Figure 2.14 shows the CERN's accelerator complex. Before particles get into the LHC, they are pre-accelerated by a cascade of smaller accelerators. Protons are taken from a bottle filled with a pure hydrogen. Hydrogen is ionized and the resulting protons are accelerated by the linear accelerator Linac 2, where they reach a kinetic energy of 50 MeV. Their energy is then gradually increased in Proton Synchrotron Booster (PSB, to 1.4 GeV), Proton Synchrotron (PS, to 25 GeV), Super Proton Synchrotron (SPS, to 450 GeV) and finally they are injected to the LHC. Acceleration of heavy ions (lead) differs only in the first two steps. They are produced in Linac 3, which delivers them into LEIR (Low Energy Ion Ring), where the ion bunches are compressed into shorter ones and accelerated. From LEIR they continue to PS. The LHC contains two rings in which the beam circulates clockwise and anticlockwise. Both beam pipes are laid next to each other in a common cryostat. To make the particles circulate, their trajectory has to be bend by super-conducting magnets providing a magnetic field of 8 T. The LHC is currently able to accelerate particles up to 6.5 TeV per elementary charge ($1 e$) in each direction, reaching the center of mass collision energy of 13 TeV for protons.

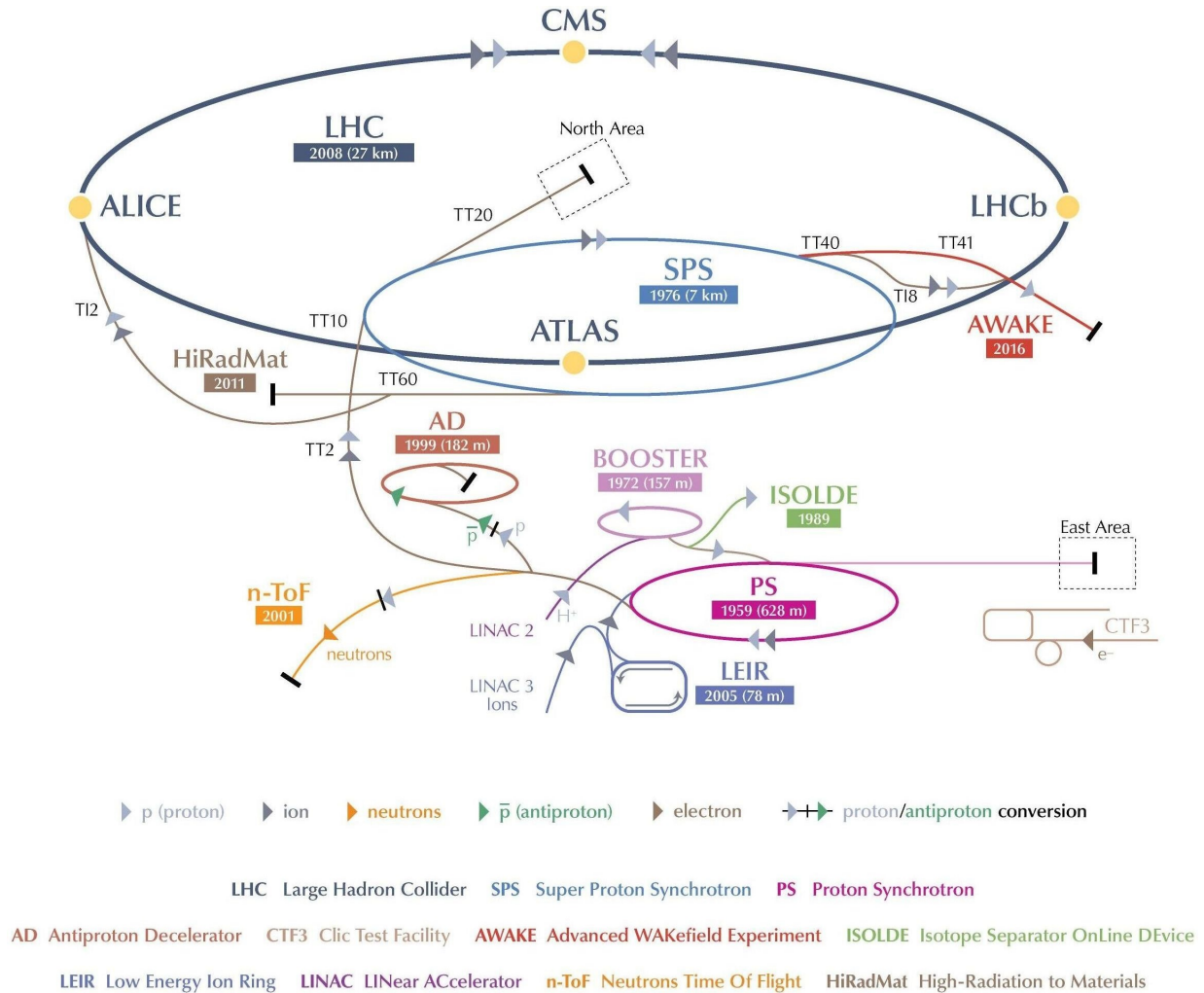


Figure 2.14: CERN's accelerator complex. Credit: CERN.

2.4.2 ALICE

A Large Ion Collider Experiment (ALICE) [3] is run by a collaboration of 173 institutes from 37 countries. ALICE studies properties of strongly interacting matter in the regime of high-energy densities and temperatures ($\approx 10^{12}$ K). Under these extreme conditions, protons and neutrons “melt”, releasing the quarks and gluons from their bonds in hadrons. This state is called the quark-gluon plasma (QGP) [38]. QGP is created by colliding ultrarelativistic² lead nuclei at the LHC. The existence of such a phase follows from the fundamental theory of strong interactions, Quantum Chromodynamics (QCD) [39]. The ALICE collaboration studies the quark-gluon plasma indirectly, via tracking thousands of particles created as the plasma expands and cools.

²With a speed very close to the speed of light, when almost all its energy is stored in the form of a momentum.

2. BACKGROUND

The ALICE detector is 26 m long, 16 m high, and 16 m wide and weights about 10 000 tons. It is illustrated in Fig. 2.15. The heaviest part of the detector is the solenoid magnet (red), which bends trajectories of charged particles, allowing to measure their transverse momentum (p_T). A view to the inside of the opened solenoid magnet is shown in Fig. 2.16. The detector consists of 18 subdetectors, each working on a different principle. Together they are capturing snapshots of final state products of the collisions. The innermost sub-detector is called the Inner Tracking System (ITS). ITS currently consists of six concentric layers of silicon pixel, drift and strip detectors, surrounding the collision point. Its main functions are tracking of charged particles, measurement of primary interaction vertex (generated directly in the beam collisions) and measurement of secondary interaction vertices from the decay of short-lived particles.

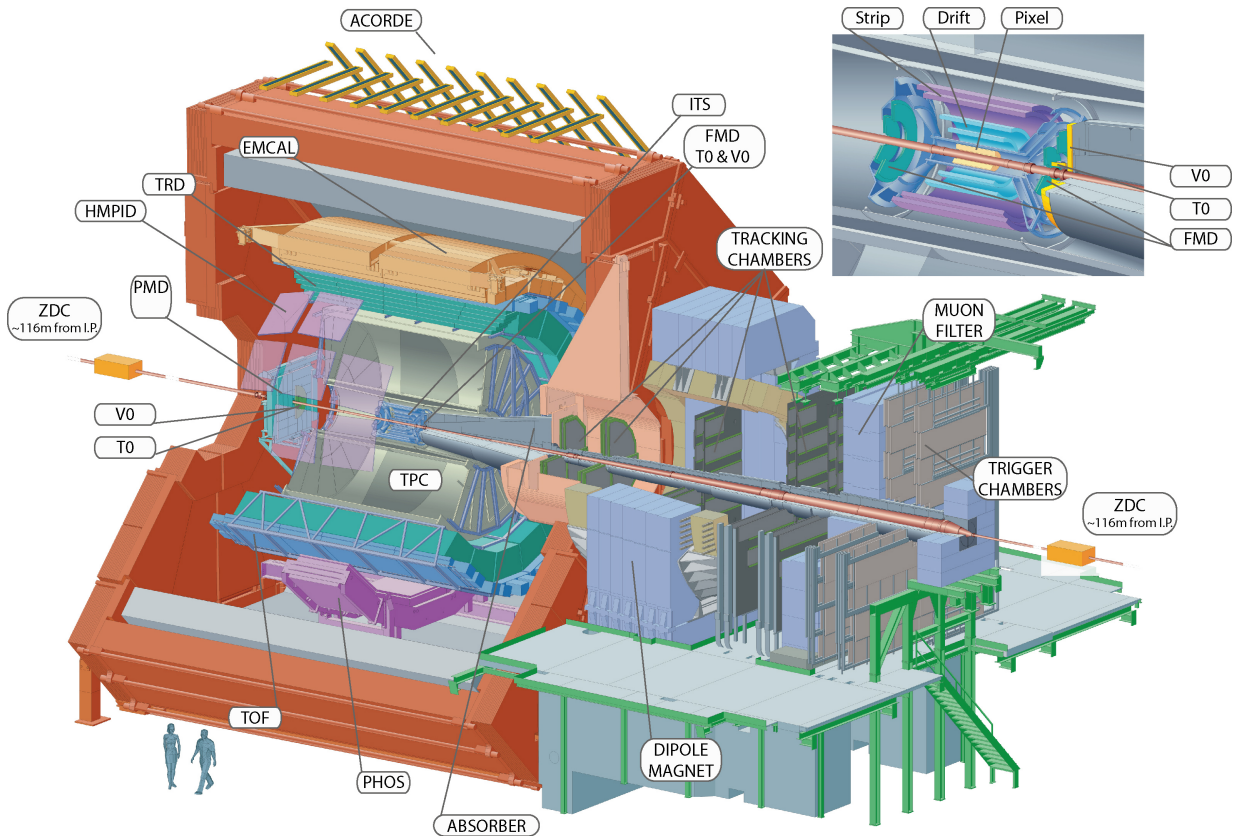


Figure 2.15: Current ALICE detector schematic. The ITS subdetector is in the center of the red magnet. The detail in top right corner shows the current structure of the subdetector. Credit: The ALICE Collaboration.



Figure 2.16: ALICE detector with the solenoid magnet door opened for maintenance. Credit: The ALICE Collaboration.

2.4.3 ITS Upgrade

In 2019 and 2020, CERN plans to interrupt operation of the LHC to give an opportunity to the machine and experiments for maintenance and upgrades. Several major upgrades are planned also for the ALICE experiment [40]. One of them is a complete replacement of the current ITS subdetector [2]. The new ITS will:

- Improve impact parameter resolution of charged particle tracks by a factor of 3 in a plane transverse to the beam and by a factor of 5 along the beam axis;
- Improve tracking efficiency and the transverse momentum resolution down to 50 MeV;
- Allow fast data readout — over 100 kHz in proton-proton collisions and 50 kHz in lead-lead collisions;
- Allow fast insertion and removal of the detector for maintenance during end of year technical stop.

The upgraded ITS, shown in Fig. 2.17, comprises 7 concentric cylindrical layers of silicon pixel sensors. Radii of the cylinders range from 22 mm to 400 mm. The detector layers are divided into the Inner Barrel (3 layers next to the beam), the Middle Barrel (2 layers)

2. BACKGROUND

and the Outer Barrel (2 farthest layers). The beam pipe is led through the axis of the ITS detector. The point of particle collisions, the so-called beam diamond, is in the center of the detector. In the region of ITS, the beam pipe will be made of beryllium, which allows to make its walls very thin, thus minimizing the influence on the products of collisions, but at the same time firm enough to hold the pressure gradient between the vacuum inside the pipe and the surrounding air. The ITS layers are azimuthally segmented in units called staves, which are mechanically independent. The staves within each group of layers have the same mechanical design. On both sides they are fixed to the endcap wheels, which serve as precision supporting structures. Cooling pipes and cabling enter from one side of the detector only, simplifying its maintenance. A carbon fiber construction helps to keep the material budget of the whole detector as low as possible.

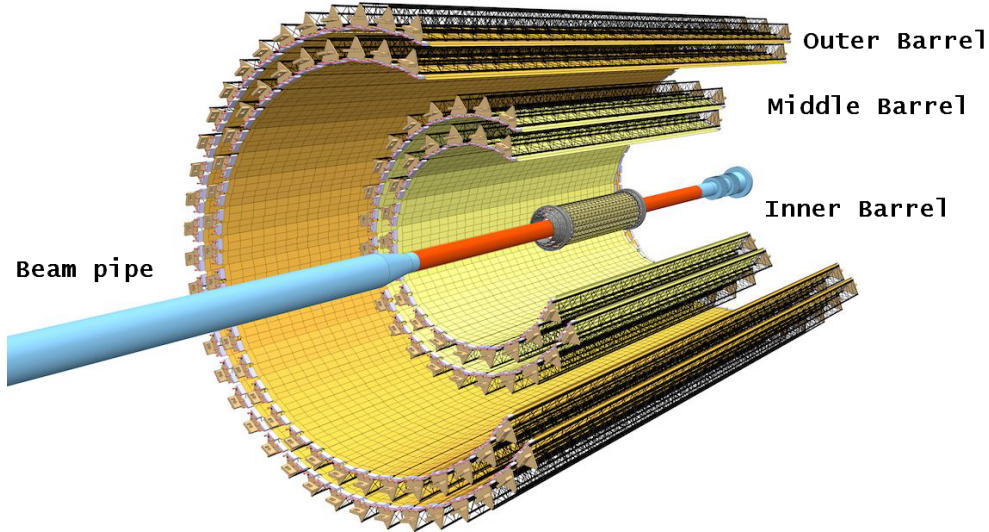


Figure 2.17: Layout of the upgraded Inner Tracking System detector. Credit: The ALICE Collaboration.

The basic sensor units of the upgraded Inner Tracking System detector are the so-called ALPIDE chips [41], which are based on silicon Monolithic Active Pixel Sensor (MAPS) technology. It is an ASIC chip specifically designed for the ALICE experiment, implemented in $0.18\ \mu\text{m}$ TowerJazz CMOS Imaging Technology [42]. The chip size is $15\ \text{mm} \times 30\ \text{mm}$ and its thickness is thinned down to $50\ \mu\text{m}$ for Inner Barrel sensors and $100\ \mu\text{m}$ for Middle and Outer Barrel sensors. The reason for thinning is again driven by the need of low material budget, to minimize its influence on detected particles. Figure 2.18 shows the structure of the chip. It is built on a high-resistivity silicon epitaxial layer, which creates the sensor active volume. On the top of this layer, there is a matrix of charge collection diodes with a pitch of about $30\ \mu\text{m}$, each creating one pixel. The white area represents a depletion region, where the created charge drifts to the diode junction. In the rest of the sensor volume, charge spreads by slow diffusion. The size of the depletion region can be

increased by applying a back-bias voltage to the substrate. Its range can be from 0 down to -6 V. The electronics that performs signal amplification, digitization and zero suppression is also built on the same chip. Its transistors are shielded by a deep P-well, preventing the deposited charge to be collected by them rather than by the collection diode. Chips are equipped with a high-speed serial data interface and a bidirectional control bus for configuration and monitoring. Only the information on whether or not a particle was crossing a pixel area will be read out. The total number of ALPIDE sensors in the upgraded ITS is 24 120. They create a detection surface of 10 m^2 , which is segmented into 12.5 billion pixels.

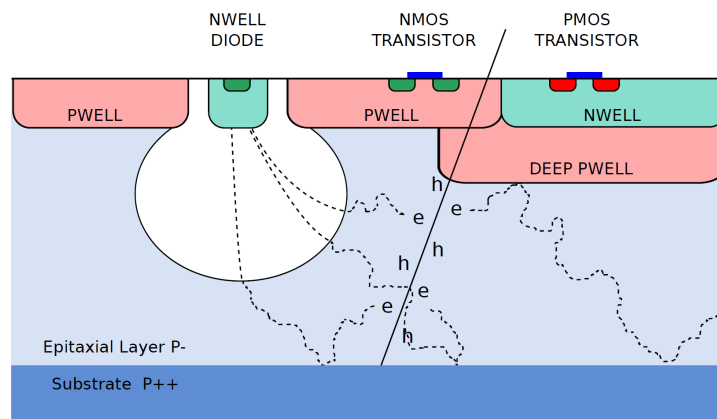


Figure 2.18: Cross section of the Monolithic Active Pixel Sensor used in ALICE ITS. Credit: The ALICE Collaboration.

Pixel sensors are glued and wire-bonded to the Flexible Printed Circuit (FPC), constituting a module. These modules are glued to staves, which provide them mechanical fixing and cooling. In the Inner Barrel, each staff contains one module equipped with 9 pixel sensors which share common clock and control signals. Each of the sensors has its own high-speed serial output running at 1.2 Gbit/s . Its diagram is shown in Fig. 2.19. The Inner Barrel consists of 48 staves and has 432 sensor chips. The length of the Inner Barrel Module is approximately 29 cm . Estimated radiation load of chips in the Inner Barrel is $\approx 2.7\text{ Mrad}$ during 4 years of operation, including the safety factor of 10 [2].

The Middle and Outer Barrel modules contain 2 rows of 7 silicon sensors. Because of its bigger radius, the density of detected events and the output data rate is expected to be much lower than in the Inner Barrel. To optimize the number of connections, each row has one master sensor which propagates clock and control signals to the other sensors in the row and collects their data via a shared inter-chip bus. As seen in Fig. 2.20, the module has two data outputs, one from each row, both running at 400 Mbps . The Middle Barrel contains 54 staves in two layers, 80 cm long with 4 modules per staff. The Outer Barrel contains 90 staves in two layers, 150 cm long with 7 modules per staff. Together there are 23 688 pixel sensors utilized in all layers of the Middle and Outer Barrel. Their estimated

2. BACKGROUND

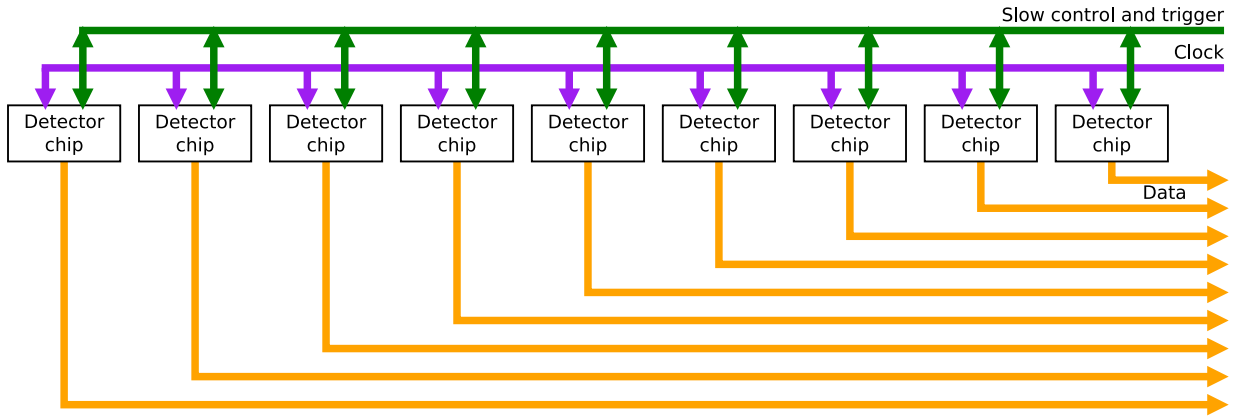


Figure 2.19: Block diagram of the Inner Barrel module. Source: [A.2].

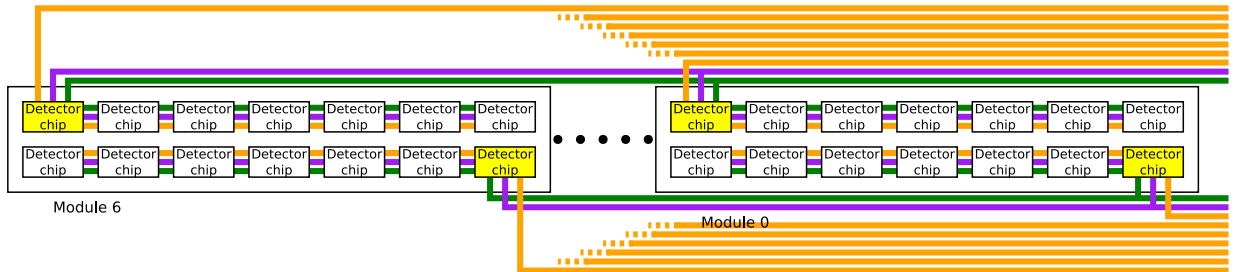


Figure 2.20: Block diagram of the Outer Barrel modules. Source: [A.2].

radiation load is ≈ 100 krad during 4 years of operation, including again the safety factor of 10 [2].

The behavior of the detector chips in the environment of the experiment has to be tested in advance. This task has two parts. On the one hand it is necessary to know how the data from the detector looks like when a given particle traverses it. On the other hand it is necessary to ensure, that the response stays the same during the lifetime period, as well as other characteristics like power consumption which should not go beyond the specifications.

Because of the limited cooling possibilities in the narrow space of ITS detector barrels, the power consumption and accompanying heat production needs to be kept as low as possible. Hence also the power available for the signal drivers is limited and it is desirable to keep the cables reasonably short to minimize the signal distortions. Therefore the readout and control system of the ITS detector will be placed as close to the detector as possible. It will be installed in the so-called ALICE Miniframe, located approximately four meters in front of the detector, two meters from the beam pipe. Here the racks with Readout Unit (RU) [A.1, A.2] boards will be placed. The expected radiation load for the RU is lower than for the detector itself, but it is still considerable. Estimated TID is about 10 krad per 4 years of operation.

	Inner Barrel	Middle and Outer Barrel
ALPIDE chip thickness	50 μm	100 μm
Spatial resolution	5 μm	10 μm
Power density	< 300 mW/cm ²	< 100 mW/cm ²
Primary vertex resolution	< 30 μm	
Detection efficiency	> 99 %	
Fake hit rate	< 10 ⁻⁶ per event per pixel	
Average track density	15–35 cm ⁻²	0.1–1 cm ⁻²
TID radiation in 4 years	2700 krad	100 krad
NIEL radiation in 4 years	1.7×10^{13} 1 MeV n eq/cm ²	10^{12} 1 MeV n eq/cm ²

Table 2.1: Overview of ITS properties after the upgrade [2].

2.4.3.1 Readout Unit

The RU will receive data from the detector chips, distribute a synchronization signal to them, control the settings of ALPIDE chips and control power supplies. The RU will also perform some basic data processing, e.g. filtering and compression. Processed data will be sent via optical links out from the experimental cavern to the Online and Offline Computing System (O²) [43], where the data from ITS will be merged with data from other subdetectors and processed. The whole ITS readout system will have to process about 1 Tbit of data per second from 432 1.2Gbit/s and 3384 400 Mbit/s data lines and operate 624 control and 624 clock lines. Hence, a large system consisting of hundreds of RU modules has to be built.

The option that the RU modules will be controlled by an FPGA is the most preferred one. Developing a radiation-tolerant ASIC chip would not be convenient, since the price would be too high and the flexibility low. During the detector lifetime, it is expected, that some of the data processing algorithms might change, as the evolving environment of the experiment requires. RU will process digital data from the thousands of detector chips in parallel. The estimated number of RU modules is 192. Those are typical characteristics of a system suitable to be controlled using FPGAs. However, the system should also meet some dependable requirements. It will be placed in a radiation environment, which is known to be unfriendly to programmable hardware and semiconductor electronics in general. It is undesirable that a failure corrupts and stops the whole data taking. The minimal estimated lifetime of the readout unit is 4 years, which is a period of the LHC run during which large service and maintenance interventions are not possible or are complicated. All components which will be used in the RU need to be properly tested and characterized for operation in a radiation environment and magnetic field.

2.5 Cyclotron

The Nuclear Physics Institute of the Czech Academy of Sciences (NPI) is located in Řež. The largest experimental facility in the NPI is the isochronous cyclotron U-120M, shown in Fig. 2.21. It is an experimental cyclotron built in 1970s. In 1990s, the cyclotron was upgraded [44, 45, 46] adding the so-called negative mode acceleration which allowed to increase the external proton current and enabled production of medical radionuclides. The cyclotron provides extracted proton beam in the energy range from 6 to 37 MeV with maximal current reaching few tenths of μA ($\approx 2.5 \times 10^{14}$ protons/s). Nowadays, the cyclotron is operated mostly in the negative mode, used for high proton flux radionuclide production. Morning transportation of radionuclides to hospitals requires that their production is run during evening or night, which leaves ample time for physics oriented studies during the day time.



Figure 2.21: The U-120M cyclotron in NPI Řež. On the left-hand side we can see the beam pipe for the negative mode with focusing magnets around it. Credit: [47].

Cyclotron operation is supported by the Ministry of Education, Youth and Sports of the Czech Republic through a dedicated grant CANAM (Center of Accelerators and Nuclear Analytical Methods), which offers to scientists and industry a possibility to use a unique experimental infrastructure in nuclear physics and neutron science [47].

2.5.1 General Principle of Cyclotron Operation

A cyclotron is a circular particle accelerator. The concept was proposed several times during 1920s [48], but the first operational machine was build and patented by Ernest Lawrence in 1932 [49]. A scheme of a typical cyclotron is shown in Fig. 2.22. A central vacuum chamber contains a hollow cylinder, split into two electrodes called Dees³. The electrodes are placed between the poles of a strong electromagnet. The magnetic field is perpendicular to the plane of the sketch in Fig. 2.22. The Dees are electrically insulated form each other and a narrow gap is in between them. Each Dee is connected to a one pole of alternating (sine) voltage power supply, creating an electric field gradient in the gap.

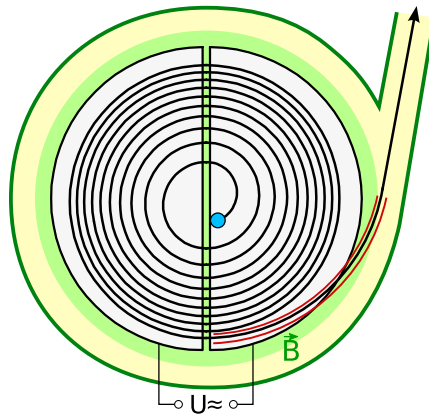


Figure 2.22: Principle of cyclotron operation. Credit: [48].

Charged particles are injected to the vacuum chamber slightly aside of its center. Due to the Lorentz force, particles follow a circular trajectory inside the Dee until they reach its edge. In the gap between the Dees, particles are accelerated by the electric field. The particles with increased speed now travel with the same angular velocity on a circular trajectory of a greater radius. The cyclotron accelerates particles only when the frequency and the phase of the electrical field in the gap are the same as the frequency and the phase of particles on their orbit. The radius of particle orbit follows from the equilibrium between the Lorentz force and the centrifugal force

$$B q v = \frac{m v^2}{r}, \quad (2.20)$$

where q is a particle charge, B denotes magnetic field, v is particle velocity, m is particle mass and r is the radius of the circular trajectory. Expressing the velocity as

$$v = 2\pi r f, \quad (2.21)$$

we obtain a formula for the cyclotron frequency

$$f = \frac{B q}{2\pi m}. \quad (2.22)$$

³The half-cylinder electrodes are called Dees, since their shape is similar to a letter "D". Generally a cyclotron can have any number of dees and corresponding acceleration gaps.

As the speed of particle increases, relativistic effects start to play a role and accelerated particles get heavier. To keep the cyclotron frequency constant, the magnetic field has to be adjusted and increases with radius. An alternative to this concept is a synchrocyclotron, where the relativistic effects are compensated by varying the frequency of the electric field [48].

It is apparent, that the flow of particles in a cyclotron is not continuous. Particles group into the so-called bunches according to the phase of the alternating electric field — they are accelerated only when there is a corresponding voltage in the gap. Each time (phase) slot when a bunch of particles would meet the criteria for successful acceleration is called a bucket. Not all buckets have to contain a particle bunch, but a bunch can be placed only into a bucket. If a particle appears out of the phase with the accelerating electric field (i.e. out of the bucket) it either synchronizes to the phase provided that the phase difference between the particle and the nearest bucket phase is not too big, or it follows a wrong trajectory in the magnetic field and is lost.

2.5.2 U-120M Principle of Operation

Unlike a generic cyclotron, the U-120M cyclotron in NPI has only one Dee electrode, powered by a resonator to which a radio-frequency (RF) electric field is brought from a generator by a waveguide [50]. The role of the second Dee is taken by the walls of the vacuum chamber which is on the ground potential. The magnetic field of approximately 1.8 T is provided by one main electromagnet and 15 correction coils, which are correcting the magnetic field shape to compensate the relativistic effects. All magnets are adjustable and so is the resonator and generator frequency. That allows the cyclotron to operate at various energies ranging from 6 to 36 MeV. The corresponding generator frequencies vary approximately from 10 to 26 MHz. However, changing the energy takes some time (approximately 0.5 hour), since all parameters have to be tuned manually.

2.5.2.1 Positive and Negative Modes

The arrangement of the cyclotron allows to operate in a so-called *positive* or *negative* accelerating modes. In the positive mode shown in Fig. 2.23a, the cyclotron directly accelerates positively charged light ions H^+ (protons), D^+ (deuterons, ${}^2H^+$), ${}^3He^{+2}$ or ${}^4He^{+2}$ (α). The beam is extracted using a magnetic kicker and a series of three electrostatic deflectors at the last orbit. Because the magnetic field cannot form a sharp edge and because the real orbits are not perfectly discrete and their density at the outer edge is very high, the extraction is ineffective and a major part of the beam is lost at the deflectors or at the exit beam pipe walls.

In the negative mode shown in Fig. 2.23b, the magnetic field orientation is inverted and negative ions H^- or D^- are accelerated in the same anticlockwise direction. To extract them, an approximately 35 μm thick carbon stripping foil is put into the beam trajectory at the outer orbit. On this stripping foil, ions lose both valence electrons. The resulting particles (H^+ or D^+ , respectively) are charged positively, therefore the Lorentz force bends

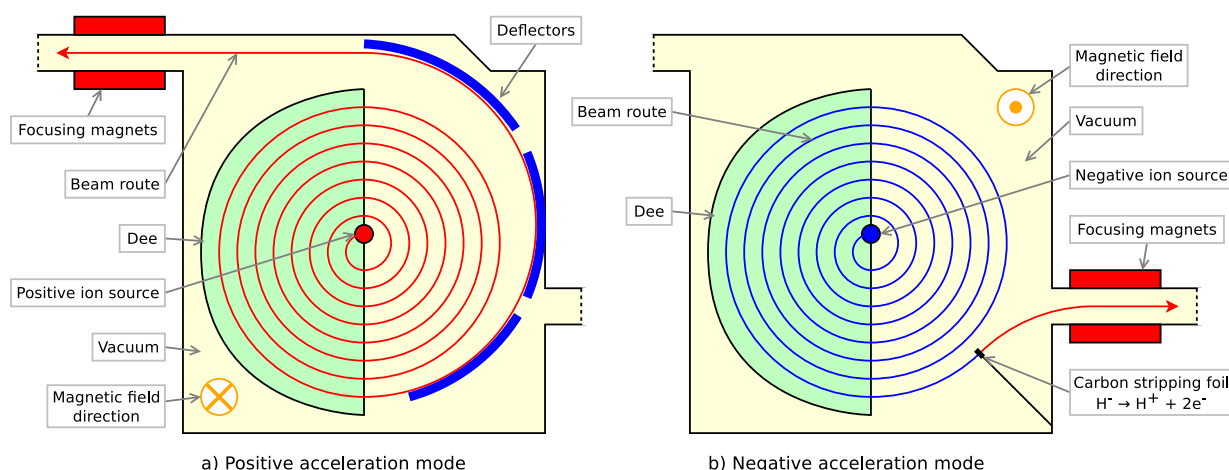


Figure 2.23: Acceleration modes of the U-120M cyclotron.

their trajectory in an opposite direction out from the acceleration chamber. In the negative mode, the efficiency of beam extraction exceeds 90 %.

In both accelerating modes, cyclotron delivers a beam of positively charged ions. Each mode has its own beam pipe to which the particles are extracted. Inside a beam pipe, dedicated beam optics directs the beam into the beam pipe axis using a series of focusing quadrupole magnets. The beam pipe for the positive mode (Line A) passes the beam through a monochromator magnet, which selects a very narrow energy spectrum. Then the beam is directed to the so-called Experimental Hall where it is divided into three target areas. The beam pipe of the negative mode (Line H) ends with one target area next to the machine. The floor plan of the experimental hall with the cyclotron and its beam pipes is shown in Fig. 2.24.

Changing the configuration between the positive and the negative mode of the cyclotron is a time consuming process. The acceleration chamber has to be filled with air and opened. The positive mode requires the deflectors to be installed. For the negative mode they have to be removed and the carbon stripping foil has to be installed. Also the ion source has to be changed. Finally, the vacuum has to be restored after closing the chamber, which is radioactive. Moreover, it takes another day to restore the ideal vacuum conditions, necessary for the stable cyclotron operation.

Because of the regular radiopharmaceutical production, which is unavailable in the positive mode, the cyclotron works most of the year in the negative mode. Switching to the positive mode is done a few times per year for about one week and is planned long time (months) in advance. The positive mode is used mostly to study nuclear reactions. On the other hand, proton beam from the negative mode is available nearly every day, during the daytime when there is no production of medical radionuclides.

2. BACKGROUND

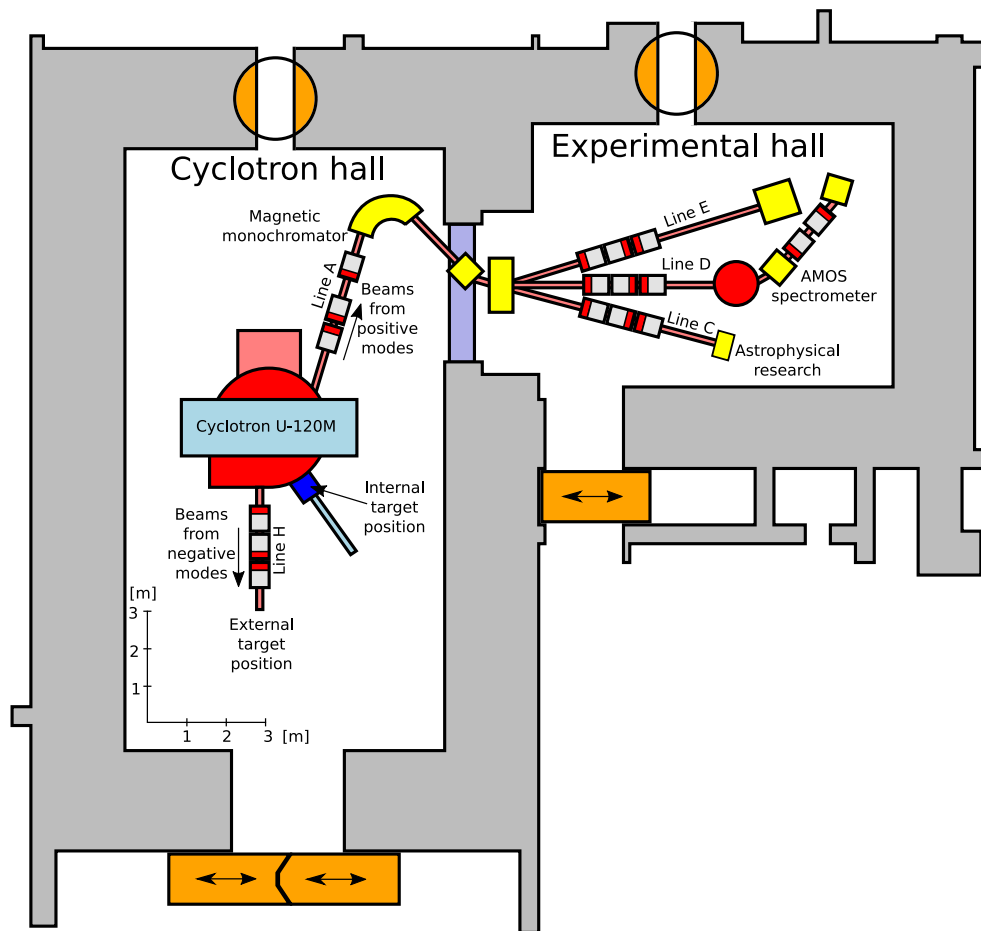


Figure 2.24: Schematic floor plan of the U-120M cyclotron and associated experimental infrastructure.



Figure 2.25: Ion source of the U-120M cyclotron, used for the negative acceleration mode. The plasma chamber is on the left-hand side.

2.5.2.2 Ion Source

The ion source of the cyclotron is placed under the acceleration chamber, inside vacuum. It is a so-called Penning type ion source [51]. Its photo is shown in Fig. 2.25. The ion source contains a plasma chamber (left side of the photo) in which an electric arc regulated by a high-voltage constant-current power supply is burning. The plasma chamber contains two holes. Through the first one, a gas which is being ionized inside the chamber is blown inside. Through the second one, the ions are pulled by the RF electric field into the acceleration chamber of the cyclotron. More information on the ion source operation and performance can be found in [52].

2.5.2.3 Cyclotron Filling

The RF resonator works near its breakdown limit. To protect it against discharges, a so-called filling scheme is used [50]. A dedicated 150 Hz generator is used for this purpose. The duty cycle (percentage) of the ≈ 6.7 ms (i.e. $\frac{1}{150\text{ Hz}}$) period of the modulation signal from the generator is set by a cyclotron operator. This signal modulates the output of the radiofrequency generator, see Fig. 2.26. The resulting effect is, that the ion extraction and acceleration works only when the modulation signal is on. Maximum allowed duty cycle (filling) depends on the generator frequency, corresponding to energy of accelerated particles, and on the number of particles present in the acceleration chamber (ion source output intensity). For the lowest energies (≈ 10 MHz generator frequency) the filling can reach rather high values ($\approx 65\%$), but for the maximum energy, it cannot go over 25% for low intensities and over $\approx 10\%$ for the highest intensities. This aspect has to be taken into account in cases, when instantaneous peak particle flux plays a role. With an average flux of 10^7 protons/cm²/s and 5% filling, the peak instantaneous flux is 2×10^8 protons/cm²/s.

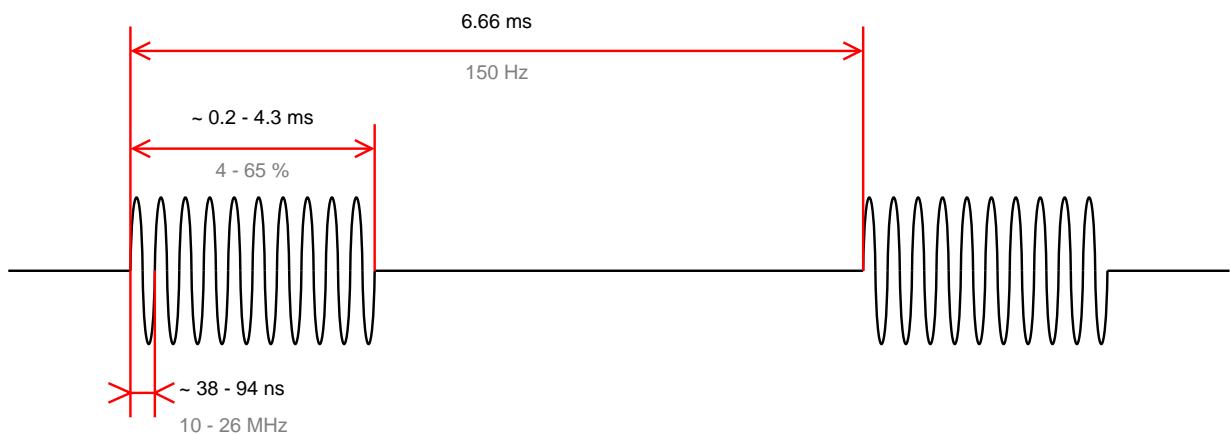


Figure 2.26: Diagram of the U-120M cyclotron filling scheme. The cyclotron radiofrequency (≈ 10 – 26 MHz, depending on beam energy) is switched on only during the adjustable duty cycle of the modulator (150 Hz). The available duty cycle range depends on the beam energy and intensity. Time flow in the diagram is not to scale.

2.5.2.4 Targets

Various target fittings for irradiated liquids, gases and small solid samples (< 1 cm) are usually connected directly to the end of the beam pipe. Because they are designed to be exposed to very high particle fluxes producing heat, they include water cooling.

For irradiation of bigger targets, like electronic boards, it is necessary to bring the beam out from the vacuum pipe into air. This is done through a $55\ \mu\text{m}$ thick aluminum beam pipe exit window, separating the vacuum space inside the machine from the outer environment. Target can be then placed farther from the exit window. There are two effects related to bringing the beam into the air. Beam protons lose energy as they interact with the air, and in addition the beam profile width increases as a result of associated multiple scattering.

As noticeable from the cyclotron floor plan in Fig. 2.24, the negative mode target area is placed next to the machine, while the positive mode target area is located in the Experimental Hall, which is farther from the cyclotron and shielded by a wall. Experiments performed in the negative mode, directly in the cyclotron hall, have to take into account, that the machine operation requires strong magnetic and radiofrequency electric fields. In addition beam losses inside the acceleration chamber and beam pipes generate low energy neutron background. These neutrons behave similarly to gas and penetrate deep through the matter until they are absorbed or decay. Experiments using the positive mode have the advantage of the shielded room, where these backgrounds are much lower.

Under the target area of the negative mode, there is a basement, where some of the cyclotron technologies are placed. This basement is connected with the target area by a hole through the floor. The hole is about 5 cm in diameter and is about 1 m long. The basement area is partially shielded from the neutron background as well as from the electromagnetic interference. It can serve as a bunker for electronic devices supporting the target setup. A prerequisite is, that these devices can be connected with the target setup using at least 5 m long cables, that can fit through the 5 cm hole. However, some neutron background is still present in the basement area and it is not safe that humans stay there, while the cyclotron is running.

2.5.2.5 Beam Intensity

The cyclotron was designed to deliver high proton beam currents ranging from about 10^8 to 10^{14} protons/s (15 pA–20 μA). All control and measurement devices are adapted to these intensities. The original means how the flux could be adjusted were:

Adjusting the filling factor. This parameter changes the time structure of the beam. It is based on a principle of pulse-width modulation. It can be safely used for applications, where only total fluence is important or where the time resolution is bigger than the modulation period. For other cases it has to be taken into account.

Adjusting the current in the ion source. This should be the optimal way how to change the flux. The current in the ion source regulates the number of ions on the input to the acceleration process. However, the high-voltage power supply of the cyclotron ion source is able to regulate the current down to about a few hundreds of mA, corresponding to the proton current in order of 10^8 protons/s and with a step of approximately 10^7 – 10^8 protons/s. Moreover, the dependence of the flux on the ion source current is not linear. Better regulation of the cyclotron current in the low-intensity regime is expected to be achieved with a new HV power supply, which will be available in 2017. It is expected that it will allow the proton current to go as low as 10 protons/s.

Progressive investigations showed, that lower intensities can be reached by changing also other parameters. Their common feature is that they decrease the efficiency of the acceleration process.

Adjusting the gas pressure in the ion source. There is a certain value of gas pressure in the plasma chamber of the ion source, at which the efficiency of ion production is the highest. Changing the pressure to some other value lowers the efficiency of H^- ion production.

Displacing the ion source exit window relative to the acceleration chamber input window. The displacement lowers the efficiency of ion extraction from the ion source. A side effect is, that the ions, which miss the input window, burn the edges of the ion source holes and shorten lifetime of the ion source assembly. The displacement also changes the X position of the extracted beam since the particles follow a different trajectory in the acceleration chamber.

Adjusting vacuum quality. Lowering the vacuum quality inside the acceleration chamber increases the probability of beam–gas remnant interaction. This leads to reduction of beam intensity but gives rise to neutron background.

Inserting a beam probe electrode into beam trajectory in the vacuum chamber. There are three probes for energy and intensity measurement installed inside the acceleration chamber. They are movable along the radial direction with a very small step. When they are partially inserted into the last orbit of the accelerated beam, a part of the beam is lost on them. Beam interacting with the probes nevertheless increases the neutron background.

Turning off the beam focusing quadrupole magnets. The quadrupole magnets focus the beam inside the beam pipe. If they are off, the beam gets wider and a significant part of it (up to 90%) hits the walls of the beam pipe and is lost. However, this method can be used only for lower beam intensities when the net beam losses are not high enough to overheat and damage the beam pipe fittings. Again, the neutron background increases

when the magnets are off. Moreover, later we have discovered that this method also lowers the mean energy of the beam by about 4 MeV, thanks to the partial beam reflections.

Closing the beam pipe collimator. The collimator is placed in the beam pipe. By closing it (narrowing the gap), the edges of the beam profile are cut and the total intensity decreases. As a side effect, the neutron background increases.

The cyclotron equipment allows to measure and monitor the beam intensity on several places. All methods are based on measuring the electric current generated by a charge deposition. For example a beam probe, when inserted to the beam, stops beam particles and their charge is conducted from the probe in a form of electric current. During this measurement the output beam is stopped and the target is not irradiated. In the negative mode, also current from the stripping foil can be measured. Because two electrons are stripped off from each H^- ion, the measured electric current is two times higher than the resulting proton current. This method can be used continuously and works also while the target is irradiated. However, both measurement methods were developed and calibrated to monitor the cyclotron under usual operating conditions, when the acceleration process is optimal and the proton current reaches several μA . For low currents in order of nA, pA or even fA, these monitoring methods are useless, because the measured current is not only below the resolution of installed ammeters, but also below the noise level, generated by the RF circuits.

2.6 Fast Neutron Generator

The Fast Neutron Generator (FNG) [53, 54] available in NPI, is an apparatus, attached to the negative mode beam pipe of the U-120M cyclotron, see Fig. 2.27. It may contain a beryllium (Be), lithium (Li) or heavy water (D_2O) target, which is bombarded by an intensive proton beam from the cyclotron. Protons interact with the nuclei of the target material, producing neutrons. Different target materials result in different energy spectrum of generated neutrons. So far we used only the Be target with the white neutron energy spectrum ranging up to 35 MeV and having the mean energy of 14 MeV, see Fig. 2.28.

2.7 Gamma Source

The NPI has also an intensive ^{60}Co gamma source that is located at the Department of Dosimetry, see Fig. 2.29. Activity of the source measured on 23rd of April 2014 was 123.4 TBq. The ^{60}Co has a half-life of 1925.5 days. With more than 99.95% chance, the decay of ^{60}Co nucleus produces 2 photons — one with an energy of 1173 keV and the other with an energy of 1332 keV. The ^{60}Co source has a form of a cylinder 21 mm high and 25 mm in diameter and is installed inside the apparatus consisting of a massive shielding case with the radioactive emitter placed inside and a remotely controlled shutter, allowing

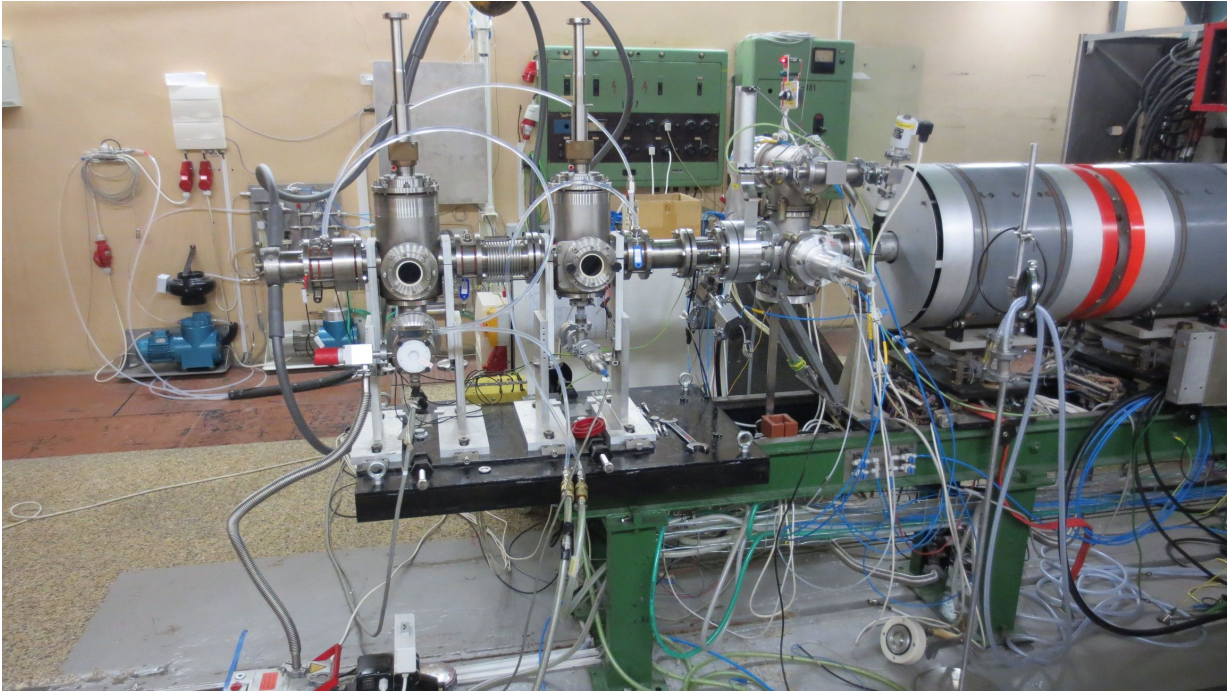


Figure 2.27: Fast Neutron Generator attached to the cyclotron beam pipe. The beryllium target is installed at the left most end of the FNG apparatus where the dark gray cooling pipes are.

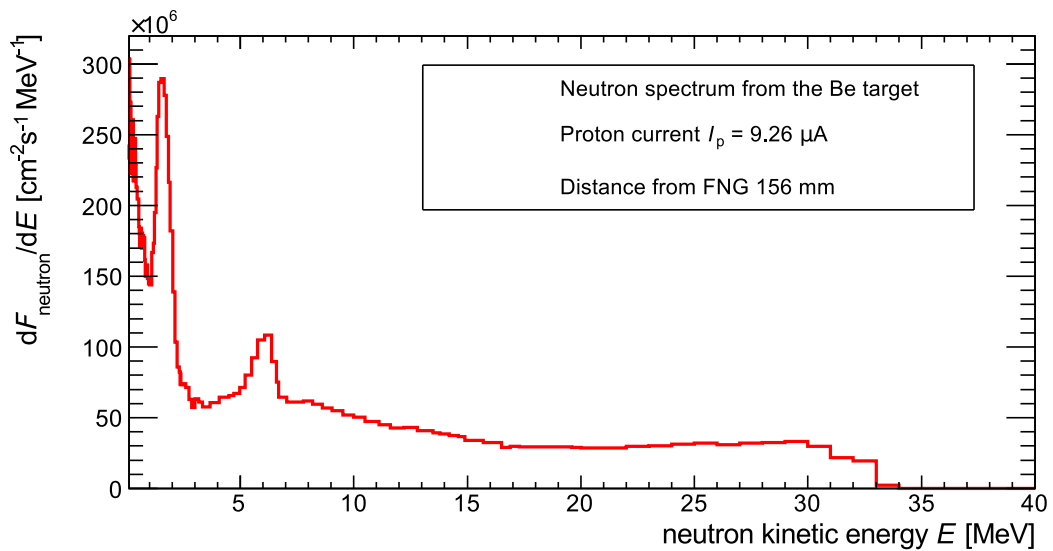


Figure 2.28: Energy spectrum of neutrons, produced by the beryllium-based fast neutron generator, bombarded by 35 MeV protons. Measured at 156 mm from the FNG target. Data taken from [54].

2. BACKGROUND



Figure 2.29: Picture of the gamma irradiation apparatus with an irradiated target (FPGA board) in front of it.

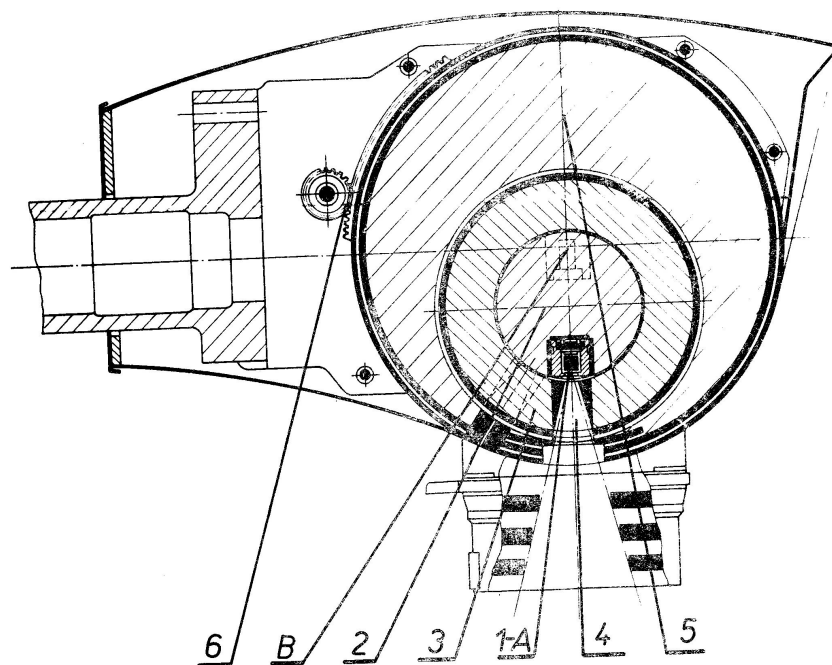


Figure 2.30: Cross section of the NPI ^{60}Co source apparatus. The radioactive emitter is marked 1-A. Courtesy: Richard Wagner.

the exposition of the irradiated sample to the emitter. The scheme of the apparatus from the top side is shown in Fig. 2.30. The case is mounted on an adjustable stand, so it can easily accommodate to the particular target. The ^{60}Co source is located in a dedicated shielded room, where the target setup can be prepared while the shutter is closed and the emitter shielded. After closing the room, the shutter is opened and the target is exposed to the gamma radiation.

2.8 Used Equipment and Tools

For our measurements we used several available tools, which will be described in this chapter. In particular, it is a PTW Farmer 30010 ionization chamber [55] for the flux measurement, a silicon pixel detector Timepix [56] with the USB interface FITPix [57] for the calibration of the ionization chamber and software tools Geant4 [32] and SRIM [20] for numerical simulations of the proton flux behavior. The Timepix/FITPix was kindly provided by the Institute of Experimental and Applied Physics of the Czech Technical University in Prague.

2.8.1 Ionization Chamber

An ionization chamber is a gas-filled ionizing radiation detector. The principle of its operation is to collect all charge generated by ionizing radiation in the working gas of the chamber. The charge is collected by applying an electric field between two electrodes, surrounding the sensitive volume of the ionization chamber. The electric field created in the gas prevents the generated electrons and ions to recombine. They are attracted to the electrode of opposite polarity and generate electric current that can be measured by a sensitive ampere-meter. The collected charge is proportional to the obtained ionizing dose and depends on the type of working gas, its pressure and volume. The value of voltage applied on electrodes influences the collection speed and thus the working regime of the ionization chamber. A schematic of the ionization chamber operation principle is shown in Fig. 2.31.

For our measurements we use the PTW Farmer 30010 ionization chamber [55], shown in Fig. 2.32. It is a commercially available thimble ionization chamber produced by the PTW company for medical radiation therapy. The detection volume of the chamber is cylindrical, approx. 24 mm long and 7 mm in diameter. It has coaxial arrangement of an internal aluminum wire electrode, surrounded by a graphite wall electrode and a protective acrylic glass (PMMA) film. Working gas of the chamber is the air at atmospheric pressure — it is an open chamber. Mean energy necessary to create one electron-ion pair in atmospheric air equals 34 eV [58]. The sensitive volume of the ionization chamber is 0.6 cm^3 . Nominal working voltage of the chamber is 400 V. Collection time of ions at the nominal voltage is about 0.14 ms [55].

The current from the chamber is read out by the UNIDOS E device, a microprocessor controlled universal dosimeter [59]. The device integrates the ionization current for a selec-

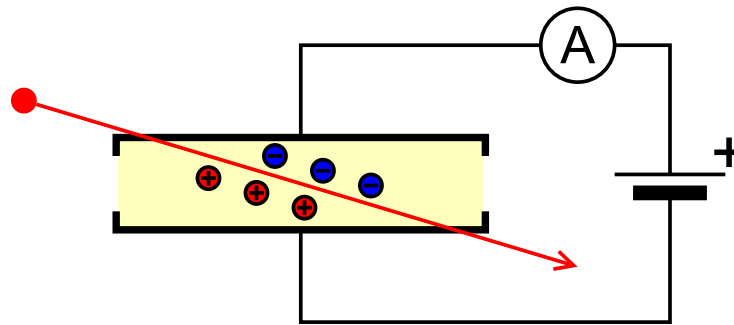


Figure 2.31: Principle of a ionization chamber. Charge, released by a traversing ionizing particle (red arrow), drifts in electric field between electrodes and is collected in a form of electric current.

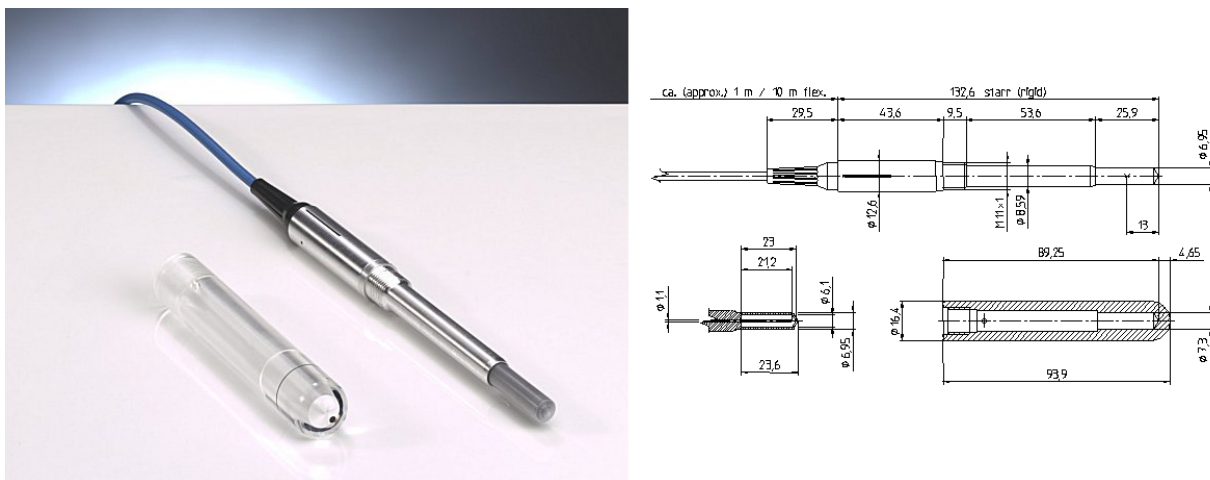


Figure 2.32: PTW Farmer 30010 Ionization Chamber. Left: Picture of the chamber and its protective cover. Right: Technical drawing of the chamber and the cover. Dimensions are in mm. Source: [55].

ted time (1–10 000 s) and calculates the average current, or accumulated charge. UNIDOS E allows to set the voltage on the ionization chamber electrodes in the range from 0 to 400 V and with 50 V steps.

2.8.2 Timepix

Timepix [56] is a hybrid silicon pixel detector, developed by an international collaboration hosted by CERN. The principle of detection is similar to the ALPIDE chips, but the electronics is not on the same silicon chip as the detector. It is on a separate chip, bonded from below to the detection layer. The electronics of the Timepix detector is more complex relative to the ALPIDE chip and allows two basic measurement modes: *Time Over Threshold*

(TOT) or *Time of Arrival* (TOA). In the TOT mode, the detector measures how long a voltage pulse generated by ionizing radiation in each pixel was above a discrimination threshold level. The measured time corresponds to energy deposited by the ionizing radiation in the pixel area. In the TOA mode, Timepix measures the time between a trigger signal arrival and a leading edge of the pulse, exceeding the discrimination threshold level. The granularity of the detector is 256×256 pixels and each pixel is a square with $55 \mu\text{m}$ long side. The total sensitive area of the chip is 1.982 cm^2 . TOA and TOT values are measured for each pixel separately and the discrimination threshold is adjustable. Because of the chip complexity, it is very slow in comparison with the ALPIDE chips. The shortest acquisition time is 1 ms and the readout of one frame takes about 10–200 ms. The detector is operated through a FITPix USB interface [57], see Fig. 2.33.



Figure 2.33: Timepix detector with a FITPix USB interface. The detector chip can be seen through a window on the left-hand side.

2.8.3 Simulations

Final states of interactions that a particle undergoes in matter are not deterministic and they can be described just in terms of probability. Numerical simulations based on Monte Carlo methods offer a cheap and effective way how to study the transport of particles through the matter. Based on an output of a large number of random trials made by the simulation, we can determine the distribution of desired values and effects. Simulations are useful to confirm our understanding of measured values by giving approximately similar results as observed by the measurement. They can be used to calculate the beam energy, dose etc. To perform simulations, two tools were used: SRIM and Geant4.

2.8.3.1 SRIM

SRIM stands for Stopping and Range of Ions in Matter [20]. It is an application for Windows which can simulate passage of ions through different layers of material. SRIM allows to describe the geometry of experimental setup just in terms of planar material

layers. These layers are characterized by their thickness and material composition. Particle trajectories through the layers are calculated in all three dimensions. User can select material of each layer from a database of elements and common compounds, or define new material. Because the original intended usage of the SRIM was to simulate ion implantation in thin layers, only ions including protons (H^+ ions) can be traced. The behavior of neutrons, electrons or photons cannot be simulated using this tool.

2.8.3.2 Geant4

Geant4 [32] is a set of C++ libraries for simulation of particle transport and interaction in matter. Relative to SRIM, Geant4 can take into account detailed setup geometry, wider class of physical processes and extensive list of particle projectiles. The simulation traces all primary and secondary particles, which have energy above certain value given by the employed physics model. We use the QBBC physics list, which was originally developed for radiomedical applications. Other models like PAI give similar results. The simulation settings such as a geometry of the target, beam profile, projectile type etc. are described in a C++ code. Simulation is performed by compiling and running the code. The user can take all advantages of the programming language — create and call own functions, read the state of the particle in any step etc.

Related Work

The following chapter overviews different irradiation facilities and methods of beam monitoring used in them. Several projects where tests of electronic components for devices operating in increased ionizing radiation had to be made are also presented. Finally a brief overview of fault mitigation techniques is presented.

3.1 Beam Monitoring

The on-line monitoring of proton beam intensity in other irradiation facilities (e.g. [60, 61]) is usually based on ionization chambers [62, 63, 64, 65, 66] or on scintillators and pulse counting in case of very low fluxes [67, 68]. Placing the ionization chamber or a scintillator into the beam route in front of the target is not an issue in facilities which provide proton beams with energy over 100 MeV. The material of the ionization chamber or a scintillator does not influence the resulting energy too much as well as the irradiated target does not stop the particles and the scintillator can be placed also behind it. Other method how to measure the flux is using a Faraday cup [69, 70, 71], which is an electrically isolated conductive absorber, where all particles of the beam are stopped and their charge is measured in a form of electric current. However, since the Faraday cup stops the beam it can not be used in front of the target. Some facilities use the radiation sensitive film, which is either monitored using a camera [72], or evaluated after the irradiation [73]. An Offline method using activation foils [74, 75] is also possible, but it provides only an average flux or integrated fluence, respectively. The usual uncertainty of the flux measurements in the facilities described above is about 10–20%. A setup for irradiation of ProASIC3 FPGA at Northeast Proton Therapy Center (NPTC) in Boston, described in [76] is shown in Fig. 3.1 to illustrate that the behavior of FPGAs in the radiation is of a common interest. An overview of relevant irradiation facilities around the world is in [77].

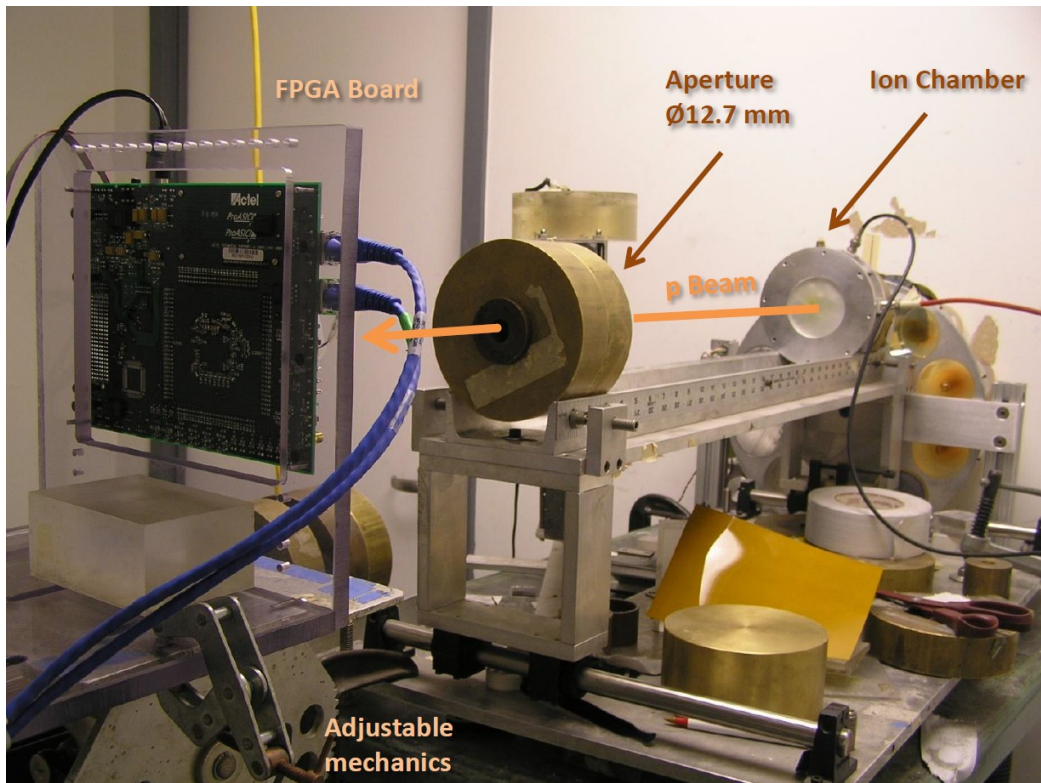


Figure 3.1: Setup for irradiation of ProASIC3 FPGA at Northeast Proton Therapy Center (NPTC) in Boston. Picture taken from [76].

3.2 FPGA Radiation Testing

FPGA manufacturers test their products among others also for radiation induced errors. Such tests are essential for devices, which are certified to be used in aircraft industry or space applications, but are often done also for commercial-grade FPGAs.

Xilinx describes their testing process in [78]. These tests are focused mainly on radiation in the common environment, where the low-intensity space neutron radiation is the most significant. Several sets of tested FPGAs were put on various places around the world with different levels of radiation background and SEUs were counted in them. To obtain enough data for SEU cross section evaluation and to shorten the required time of the measurement, each set contained hundreds of FPGAs. In total, about million device hours of operation was measured. Another test was done using accelerated life testing (ALT) methods which employed a high energy neutron source of known intensity and energy spectrum. Both methods turned out to provide equivalent cross sections.

Other manufacturers such as Microsemi (formerly Actel) do similar tests (e.g. [79, 80]) mostly using ALT only. Manufacturer-independent tests [81, 82, 83, 84, 85] are performed usually by users of the components — designers of final products intended to be used in mid and high radiation environment.

Similar issues regarding dependability of electronics in radiation environment that are investigated within the ALICE ITS Upgrade project, have to be solved also by other experiments in the field of experimental particle physics, e.g. [86, 83, 87, 88, 76]. In such projects, both individual components and the final device are tested progressively during the development process using ALT. Based on the results of each test, the next design steps are adjusted to meet the required dependability criteria. The first task is to select a suitable component, which will survive the total expected ionizing and displacement damage dose without changing its performance characteristics. Another important factor is a SEE rate, especially of potentially destructive events like latch-ups, whose rate has to be negligible. Single event upsets are unavoidable in digital circuits, but it is preferred to keep their number as low as possible. Based on their rate, a convenient design technique to increase fault tolerance is usually used for critical parts of the design.

3.3 Fault-Tolerant Design Techniques

The choice of the right technique and scale of securing the design depends on the system dependability requirements. Different methods are suitable for cases when

- the system can fail completely, but the fault has to be indicated within a defined delay and (automatically) recovered in a given time,
- the function of the system can be interrupted and can stay not available for a given time, preventing that wrong data appears on the output,
- the system needs to stay always on, synchronized and providing valid data words on the output, but allowing that an acceptably small fraction of data content can be wrong,
- or when both the function and the output need to stay correct all the time.

Selecting the proper technique depends also on how often faults occur and how many faults may occur at the same time.

The most common technique to mitigate faults used in a complex systems is a Triple Modular Redundancy (TMR) [89] together with the bitstream scrubbing or another type of fault correction [90].

Bitstream scrubbing [91] is a technique used to detect and correct faults. It is based on reading the content of the configuration memory periodically and searching for faults in it. That can be done for example by comparing it with the golden bitstream, or if the bitstream contains some error detection code by verifying that code. When a fault is detected, the configuration can be reloaded partially or completely. Some FPGAs offer the availability to repair the fault using an error correction code in the bitstream, thus it is not necessary to store the golden bitstream for reloading. Scrubbing does not detect the fault immediately, therefore using it alone is possible only in systems where presence of a failure for a given time does not matter. The readout period and the time required for the

correction defines the maximal time for which the fault will be present. If the bitstream scrubber is implemented internally in the FPGA or in another way which is vulnerable to faults, it is necessary to take the possibility of the scrubber failing into account.

If a failure of the system even for a short time is not acceptable, another technique, usually a **TMR**, has to be implemented. The TMR utilizes three modules performing the same function, but not necessarily in the same way. Their inputs are connected in parallel and their outputs are connected to a voter, which compares them and selects the majority, i.e. if one module gives a different result than the other two, it is considered faulty and not used. At the same time, the module with a different output can be marked as corrupted and its recovery can be initiated. The recovery has to be done before another fault occurs in another module, because then the majority for the voter would be lost. The level on which the TMR is used can differ from individual registers, over small functional blocks up to the whole system. However, the TMR has also disadvantages. The most significant one is that it requires more than three-times larger resources (area and power) than the unsecured system, while the increase of the reliability is always lower than two times [89]. On the other hand TMR provides a straightforward solution to increase system dependability and there are several more or less automated tools to generate the TMR-secured design from the non-secured one [92].

If the uninterrupted function of the system is not required and an immediate fault detection but not correction is sufficient, **duplex** can be used. The concept is the same as in the case of TMR, except that there are only two modules. When the output of the two modules differ, the voter detects a failure, but can not determine which module is faulty.

Although more effective techniques of securing the design against faults exists [93], they are not so widely used, since they often require more designer's effort to implement them and suitable automated tools are not available yet. They are often based on an encoding which allows to detect if the output is correct or not, or even allows to correct errors in the output word.

NPI Infrastructure Extensions

Within the scope of the ITS Upgrade project, we have tested radiation hardness of different electronic components and response of detector chips using the proton beam from the NPI U-120M cyclotron. These experiments often required on-line measurement of a very low beam currents. Standard procedures and tools used by cyclotron operators described in Section 2.5.2.5 turned out to be unusable. Therefore, we developed a new method of proton current measurement, which allows to perform an on-line measurement of proton flux, fluence and dose accumulated in irradiated samples. The method works for fluxes down to several fA. This chapter describes our approach in detail.

4.1 Target Setup for Proton Irradiation

Because of the easier availability, we work with the negative mode of the U-120M cyclotron. In this mode, the beam is delivered to the area next to the machine. The space available for an experimental setup is approximately 4 m long and 2–3 m wide. The maximal diameter of the beam at the beam pipe exit window is limited by the exit window size of ≈ 16 mm. Vertical beam position above the experimental hall floor is 121 cm and it should not vary by more than few mm within the experimental area. On the other hand, the horizontal angle of the beam axis is not always aligned in the same way and may differ between irradiation campaigns. It depends on many factors, e.g. ion source position, energy of accelerated particles or settings of the focusing magnets.

Since the area in front of the negative mode output is used also by other users (e.g. radiopharmaceutical production, FNG), we needed to develop an experimental setup which can be prepared elsewhere in advance and then easily transported to the experimental area in a reasonably short time [A.4]. Figure 4.1 shows the logical connection of all basic devices that we use for sample positioning and proton flux measurement. Figure 4.2 presents a simplified sketch of our typical setup including the beam route from the beam pipe to the irradiated sample.

To be able to scan the beam position at the target setup and to be able to adjust the irradiated sample into beam center conveniently, we use a remotely controlled movable

4. NPI INFRASTRUCTURE EXTENSIONS

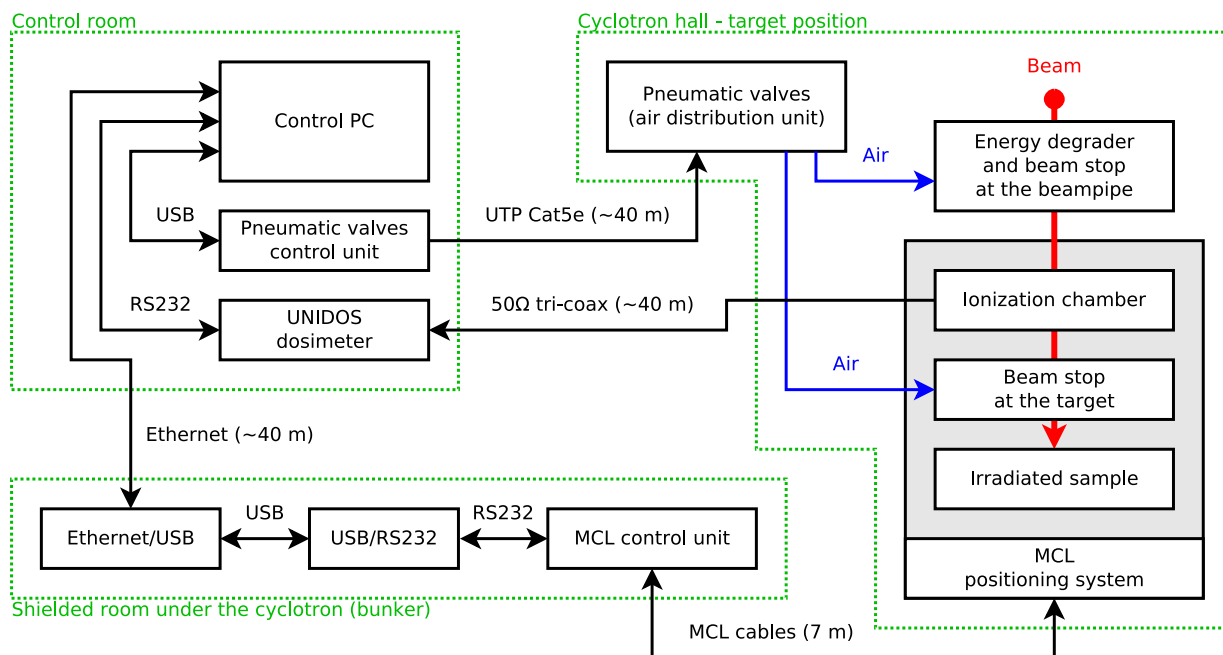


Figure 4.1: Logical connection of the components required for sample positioning and on-line flux measurement in our basic irradiation setup.

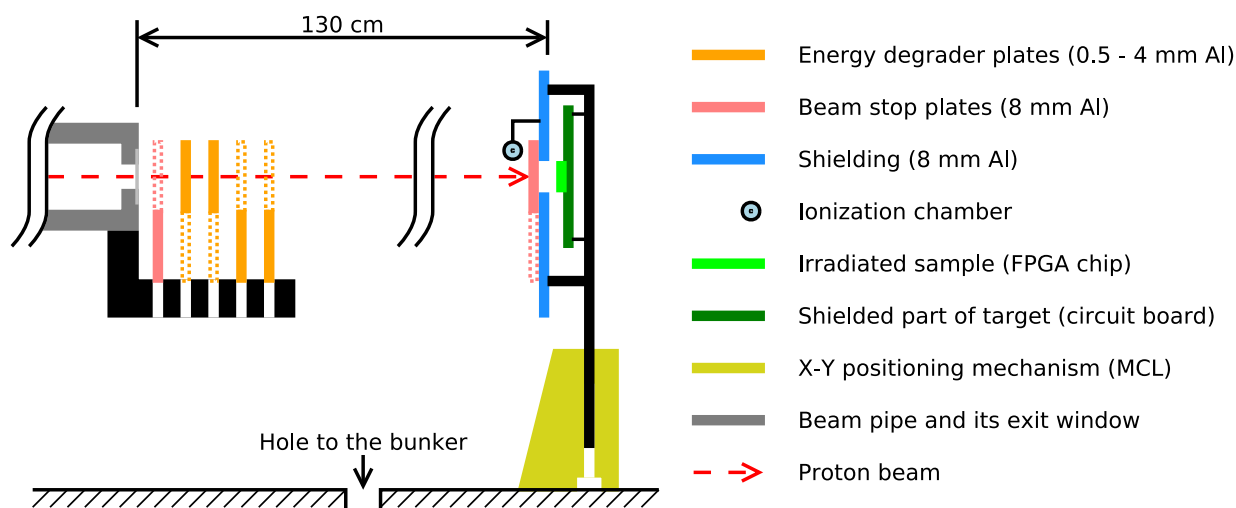


Figure 4.2: Sketch of the beam route through absorber plates to the irradiated sample. The sample, ionization chamber and a beam stop plate are mounted on a positioning mechanism.

platform (MCL cross table [94]). It is capable of moving in 2 axes (X and Y) in the range of 10 cm in each axis with a step of 1 μm and high precision of the position repeatability. It is mounted on a transportable stand and equipped with a set of adjustable aluminum bars, used for attaching the irradiated sample. The cross table contains only mechanical parts, stepper motors and limit switches. Its controller is placed in a separate case, connected by 7 m long cables. The MCL stage can be controlled and monitored using a serial port (RS-232). The controller is placed in the bunker under the cyclotron hall, shielded from radiation. The stand with the irradiated sample is placed in the beam axis, 130 cm away from the beam pipe exit window. It is a trade-off position, where the beam in the air gets wide enough to ensure uniformity of proton distribution across the target, but at the same time the energy loss of protons is still reasonably low (≈ 2 MeV).

The exact position of the beam and its profile is determined by the PTW Farmer 30010 ionization chamber described in Section 2.8.1. The ionization chamber is attached on the moving platform next to the irradiated sample, but not covering it. The distance in the transversal plane between the sample and the chamber for the particular setup is measured before each irradiation. I have developed a laser aiming device for this purpose as well as for the coarse positioning of the setup frame with the MCL cross table to the target position. The laser beam points in the direction of the beam axis, which allows us to determine the approximate position of the beam spot on the setup. After fixing the frame at the approximate target position, we move the cross table such that the laser beam aims to the center of the ionization chamber and we read its coordinates. Then the irradiated sample is moved into the laser beam and coordinates are read again. The difference of these two positions gives us the relative position of the sample and the ionization chamber with a precision of at about 1 mm.

Once the cyclotron is tuned and the beam is extracted, we can start the procedure of the beam profile scanning. Scanning is done by stepwise moving the whole target setup fixed to the cross table through the beam along x and y axes respectively. In each step, the current from the ionization chamber is measured. The measured beam profile is parametrized by a Gaussian function, see Fig. 4.7. This gives us the coordinates of the cross table for a position when the ionization chamber is in the center of the beam and also the information on beam profile. From the known relative position of the ionization chamber and the irradiated sample, we can determine the coordinates of the platform, when the irradiated sample is in the center of the beam and move it there. When the sample is at the position of the beam center, the ionization chamber measures the flux at the edge of the beam spot, but since the profile is known, it is possible to recalculate the values to the flux in the beam center.

To prevent that the sample is irradiated while the beam is being adjusted and scanned, a pneumatically-controlled sliding aluminum beam stop plate can be inserted between the irradiated sample and the ionization chamber. Another beam stopper is at the beam pipe exit window, together with a set of energy degrader plates, which can lower the proton energy and increase the transverse width of the beam if needed.

All equipment is controlled and monitored from one PC by software [95] based on ROOT package [96]. It can automatically scan the beam profile and fit the Gaussian curve

through the measured data points, monitor the beam intensity, calculate the dose obtained by the sample and control the beam stoppers and degrader plates. The screenshot of the software GUI is in Fig. 4.3. It logs all data for further analysis. In following subsections, key parts of the setup and their operation are described in more detail.

4.1.1 Energy and Beam Profile Adjustment

Changing the energy of protons by tuning the cyclotron is a time-consuming process. It requires adjustment of several parameters, e.g. the generator frequency, current to magnets and tuning the resonator circuit for the new frequency. Then it takes some time until all affected components reach new stable temperature and the beam intensity stabilizes. Therefore we introduced a new energy degrader unit to simplify and speed up the process.

The idea of the energy degrader was inspired by a similar systems, which are being used in other irradiation facilities. The energy degrader consists of a series of aluminum plates of different thickness, which effectively slow down passing protons. By inserting the plates into the beam trajectory, energy of protons is lowered correspondingly to the thickness of the particular plate or their combination. The cyclotron can then always run with the configuration for maximum energy and the energy degrader plates can be used to instantly lower the mean energy of the beam. Useful side-effect of inserting the plates into the beam is the increase of the beam width due to multiple scattering.

The energy degrader unit can be attached to the end of the beam pipe, just behind the exit window. It has 5 positions for plates, which are easily exchangeable. I have designed the degrader plates to be made of aluminum since it does not get activated by long-lived isotopes when irradiated with the proton beam. In addition, aluminum provides also convenient stopping power for 35 MeV protons when compared to copper which is commonly used at facilities with higher beam energies¹. A Comparison of the mean proton beam energy reduction in Al and Cu is shown in Fig. 4.4.

Degrader plates are 0.5, 1, 2, 4 and 8 mm thick. The 8 mm plate serves as a beam stop, which quickly shields the irradiated setup including the ionization chamber from the beam, cf. Fig. 4.4. The other 4 plates are used to lower the proton energy. The order of plates in the direction of the beam is: 8 mm (beam stop), 0.5, 1, 2 and 4 mm. Their position (in or out of the beam) is defined by pneumatic drives, which are controlled remotely. By combining them, we have the possibility to set up to 32 combinations, but not all are being used now. The change of the beam energy as a function of the degrader plates configuration was simulated using Geant4 and SRIM, see Fig. 4.5, Fig. 4.6 and Table 4.1.

The transverse profile of the beam for different configurations of the energy degrader was measured using the ionization chamber. The beam was scanned along x and y axis in steps of 10 mm. Figure 4.7 shows the measured values of ionization chamber current I_{ch}

¹Copper provides quite high stopping power for protons, but the big disadvantage of the material is that proton-induced nuclear reactions produce radioactive ^{65}Zn with a half-life of 244 days and ^{62}Zn with a half-life of 9 hours. Thus the plates stay radioactive for quite a long time, which is not convenient when handling them after the irradiation.

4.1. Target Setup for Proton Irradiation

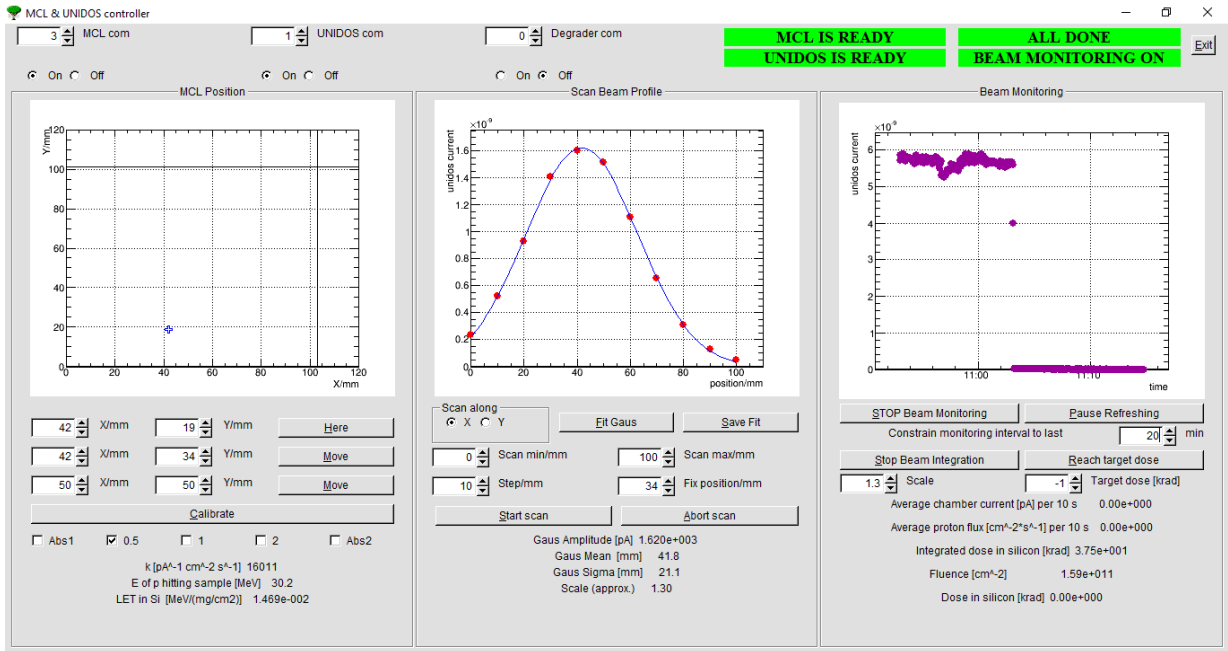


Figure 4.3: Screenshot of the control and monitoring software. Left-hand side part is for the position and energy degrader/beam stopper control, middle for the beam profile scanning and in the right-hand side part are controls for the beam monitoring.

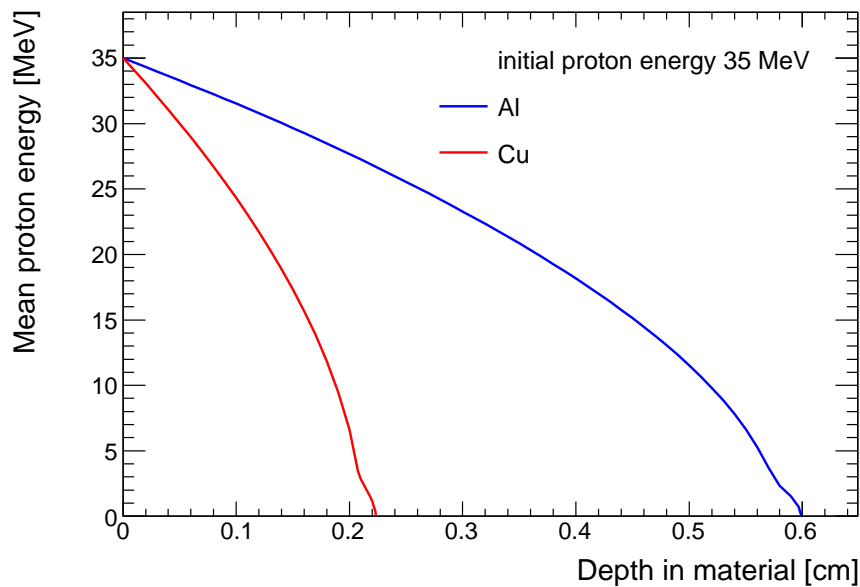


Figure 4.4: Comparison of mean proton energy in copper and aluminum as a function of traversed distance simulated by Geant4. Initial proton energy was 35 MeV.

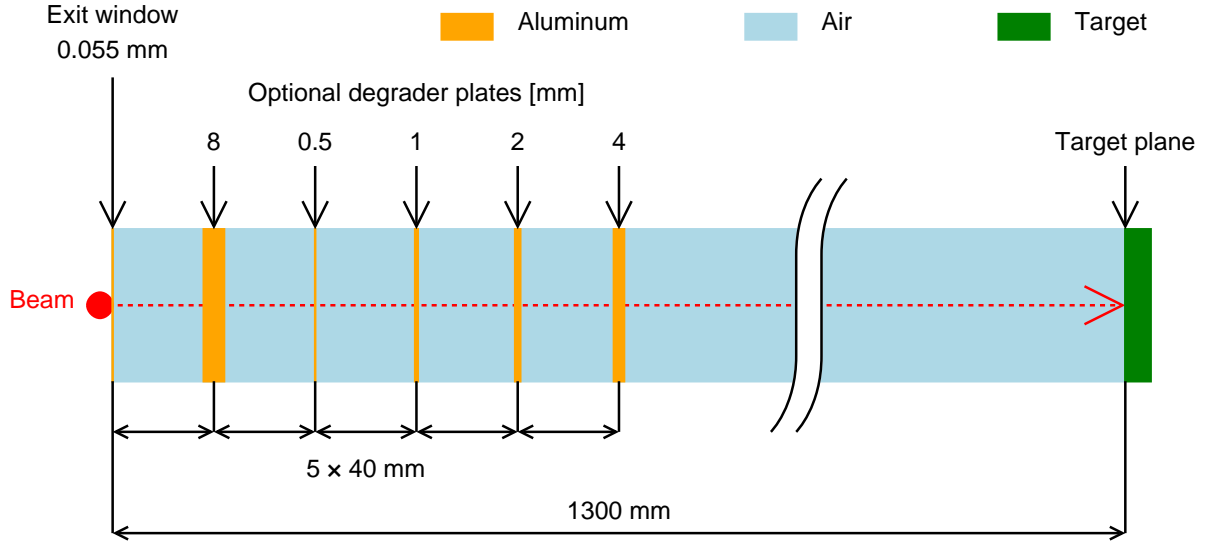


Figure 4.5: Geometry of the simulated setup with energy degrader. Protons fly through the setup from left to right. After being emitted by a proton source, marked by a red dot, protons first traverse the beam pipe exit window, then pass the optional configuration of degrader plates and finally fly through air until they reach the target plane.

Degrader thickness [mm]	Geant4			SRIM		
	σ_d [mm]	\overline{E} [MeV]	σ_E [MeV]	σ_d [mm]	\overline{E} [MeV]	σ_E [MeV]
0	10.6	32.3	0.12	9.6	32.0	0.12
0.5	19.9	30.3	0.17	15.5	30.1	0.18
1.0	25.1	28.2	0.20	20.2	28.1	0.21
1.5	31.2	25.8	0.24	25.0	26.0	0.25
2.0	34.0	24.1	0.27	29.2	23.8	0.30
2.5	40.2	21.4	0.32	34.0	21.3	0.35
3.0	45.6	18.6	0.37	39.1	18.6	0.40
3.5	52.7	15.2	0.45	45.2	15.6	0.50
4.0	55.8	11.6	0.55	49.5	12.0	0.61
4.5	67.3	6.0	0.91	58.7	7.2	0.91

Table 4.1: Results of Geant4 and SRIM simulation of the experimental setup shown in Fig. 4.5. For a given configuration of degrader plates we quote corresponding mean proton energy in front of the target (\overline{E}), proton energy resolution (σ_E) and the mean width of the beam profile in transverse plane (σ_d). Initial proton energy is 34.5 MeV. The parameters σ_d and σ_E represent a standard deviation of the Normal distribution, fitted on the results of 100 000 simulated trials. The corresponding energy spectra are also plotted in Fig. 4.6.

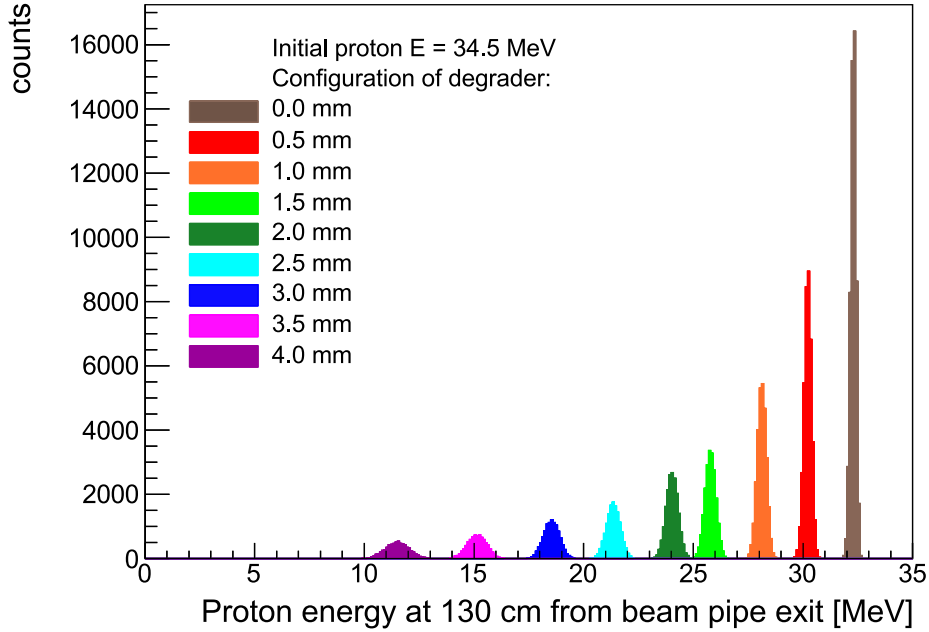


Figure 4.6: Energy spectra of protons at the target plane for different degrader configurations simulated by Geant4. The initial beam energy is 34.5 MeV.

as a function of spatial coordinate. Data were fitted with the Gaussian function

$$I_{\text{ch}}(\xi) = A \times \exp\left(-\frac{(\xi - \mu)^2}{2\sigma^2}\right) \quad (4.1)$$

where ξ stands for the coordinate of the x or y axis along which the scan was performed, A is the value of ionization chamber current in the beam center, σ represents the beam width and μ is the coordinate of the beam center for the given axis.

The chamber measures the mean value of the current density over its cross section. Because of the asymmetric shape of the ionization chamber ($\approx 21 \text{ mm} \times 6 \text{ mm}$) we did not know how much the measured beam profiles are distorted. Therefore a cross-check measurement of the beam profile was made using the Timepix detector. For the measurement, the degrader configuration with no plates in the beam was used. In such a configuration the beam width is the most narrow and it is expected that the effect of distortion is the most significant. Moreover, beam profile fits the area of the Timepix detector, so it can be captured without moving the detector and composing multiple images. For the reconstruction of the beam profile from Timepix, we used the fact that protons passing through the Timepix detector deposit so much energy, that it spreads across several neighboring pixels, creating a so-called cluster. Only clusters consisting of at least six pixels were marked as a proton hit. Smaller clusters were considered to be noise. Figure 4.8 shows both individual proton clusters in one captured frame and an integrated distribution of proton hits over the whole measurement. Figure 4.9 presents the distribution of proton cluster centroids along x and y axis together with the fitted Gaussian function. Extracted width

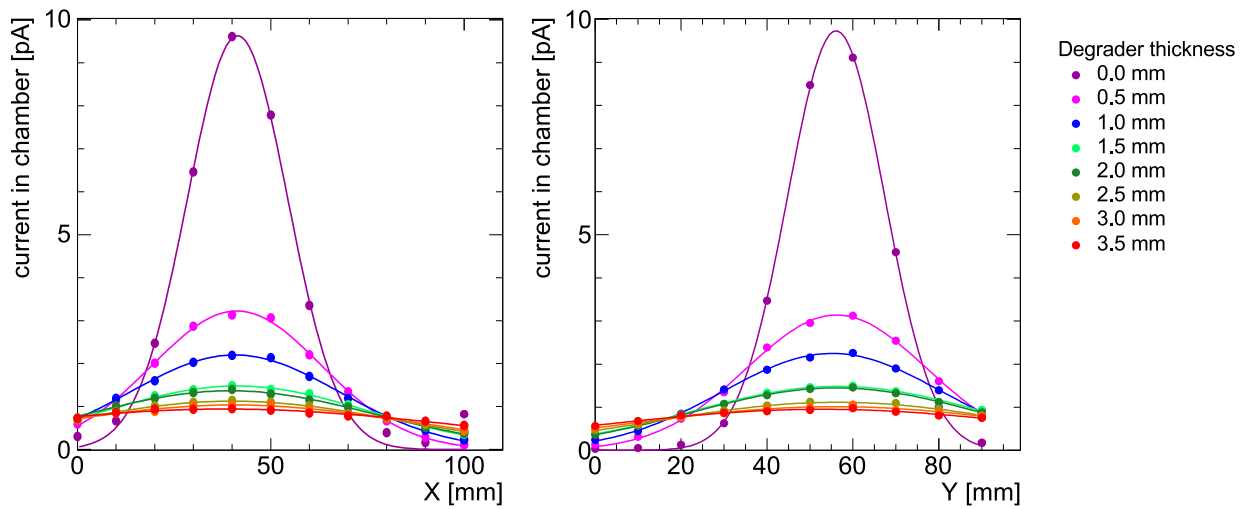


Figure 4.7: Transverse beam profiles measured with the ionization chamber along the x axis (left) and y axis (right) direction for different configurations of the energy degrader. Data are fitted with (4.1).

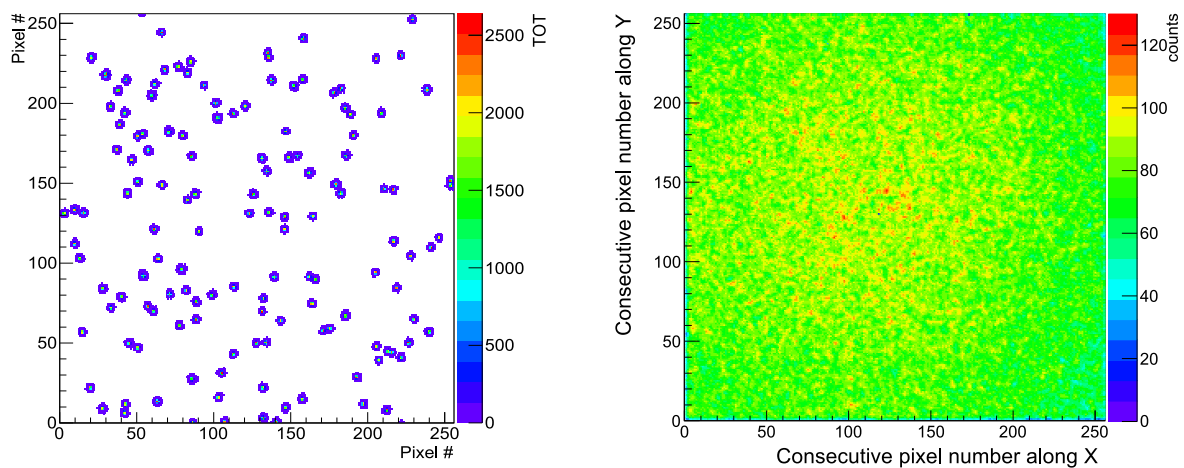


Figure 4.8: Beam profile as seen by the Timepix detector. Left: A single snapshot 1 ms frame of the beam, where individual proton clusters can be seen. Right: Data integrated from a series of snapshots. The color of each pixel represents how many times it was a part of a proton cluster.

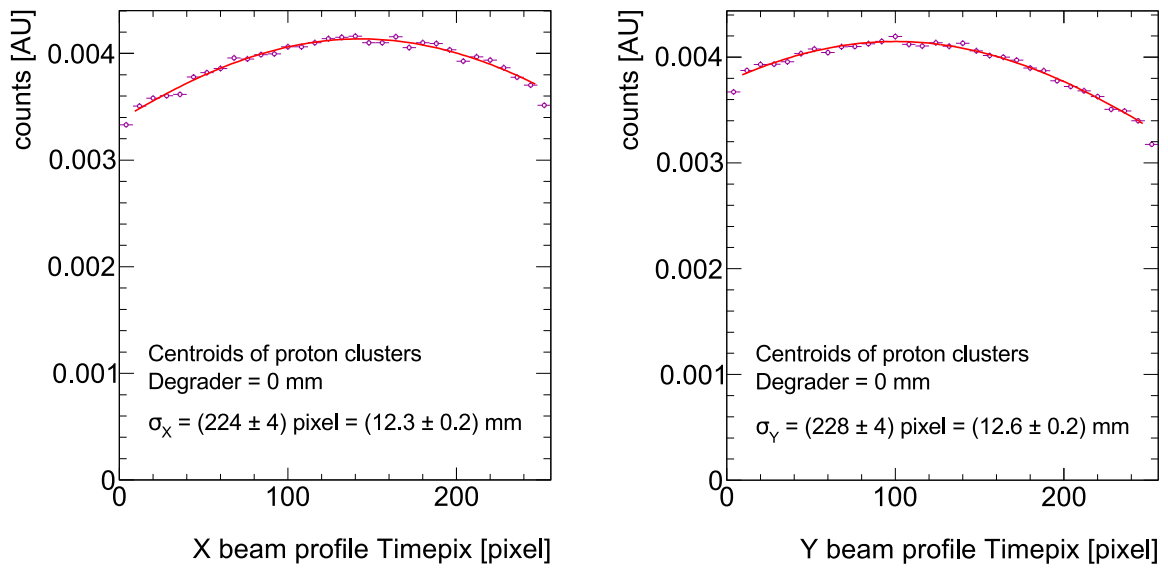


Figure 4.9: Beam profile as seen by the Timepix detector.

Distribution of proton cluster centroids on the Timepix chip in the x (left) and y (right) direction. The data are fitted with a Gaussian function. The known size of a Timepix pixel ($55 \mu\text{m}$) enables to convert the extracted beam width dimensions from pixels to millimeters.

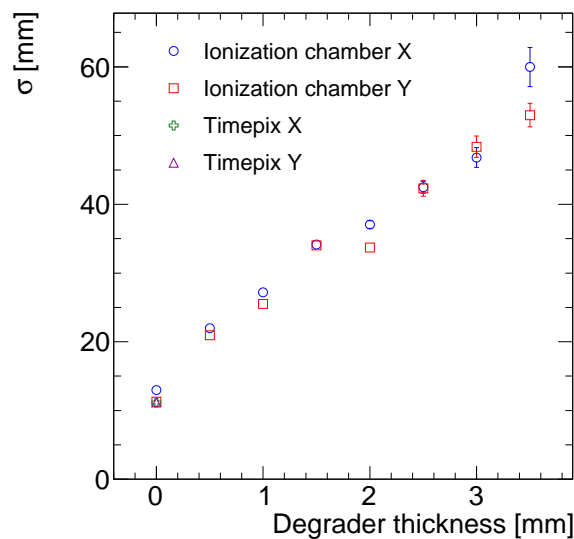


Figure 4.10: Beam profile width for different degrader thickness measured using ionization chamber. For the configuration without degrader plates in beam (0 mm), the profile was measured also using Timepix.

of the beam profile measured by Timepix agrees with the one, obtained by the ionization chamber measurement, see Fig. 4.10.

It can be concluded that even for the most narrow beam profile the ionization chamber gives a good projection of the beam profile dimensions and the effect of distortion is up to 1 mm only. For the wider beam profiles this effect can be neglected. Procedures of the Timepix data measurement and data evaluation are described in [97].

4.1.2 Flux Measurement

The on-line proton flux monitoring is based on the current measured by the ionization chamber. The chamber is designed and calibrated to measure gamma and electron radiation level in air or in phantom material [98]. In order to convert the measured current to proton flux, it was necessary to perform our own calibration measurements and verify linear response of the chamber as a function of the beam intensity. The desired output of the calibration process is a relation between the current in the ionization chamber I_{ch} provided by the UNIDOS dosimeter and the proton flux F to which the chamber is exposed.

In the regime of small proton fluxes, it is possible to measure the flux directly using the Timepix detector and counting individual protons in each captured frame. The minimum Timepix acquisition time of 1 ms, limits the maximal proton flux, for which it is possible to distinguish between individual protons in captured data. When proton flux is too high, clusters will start to blend. During the experiment, it was found that the limit for measuring proton flux using Timepix is approximately $10^5 \text{ cm}^{-2} \text{ s}^{-1}$. The setup, we used for the calibration, can be seen in Figure 4.11.

For each degrader configuration, a series ≈ 1000 of frames was captured by the Timepix detector at the beam center. Frames are assumed to be distributed randomly through the period of the cyclotron filling scheme. The current from the ionization chamber was measured simultaneously. In each frame, proton clusters were identified and counted. From the known acquisition time of each frame $T_f = 1 \text{ ms}$, the number of detected protons N_p in all frames, the number of frames N_f and the area of the Timepix detector chip $S_t = 1.982 \text{ cm}^2$, the proton flux F was calculated as:

$$F = \frac{N_p}{N_f \times T_f \times S_t}. \quad (4.2)$$

Figure 4.12 shows the correlation between the ionization chamber current I_{ch} measured at the beam center and the corresponding proton flux F measured using Timepix. The measured dependence is clearly linear, which allows to parametrize it as

$$F = k \times I_{\text{ch}}, \quad (4.3)$$

where k depends on the proton energy, thus on the degrader configuration. Similar relations obtained for other degrader configurations are shown in Fig. 4.13.

The validity of (4.3) relation for higher I_{ch} was then verified using an independent method, which measures the proton flux by means of activation of copper foils. From the

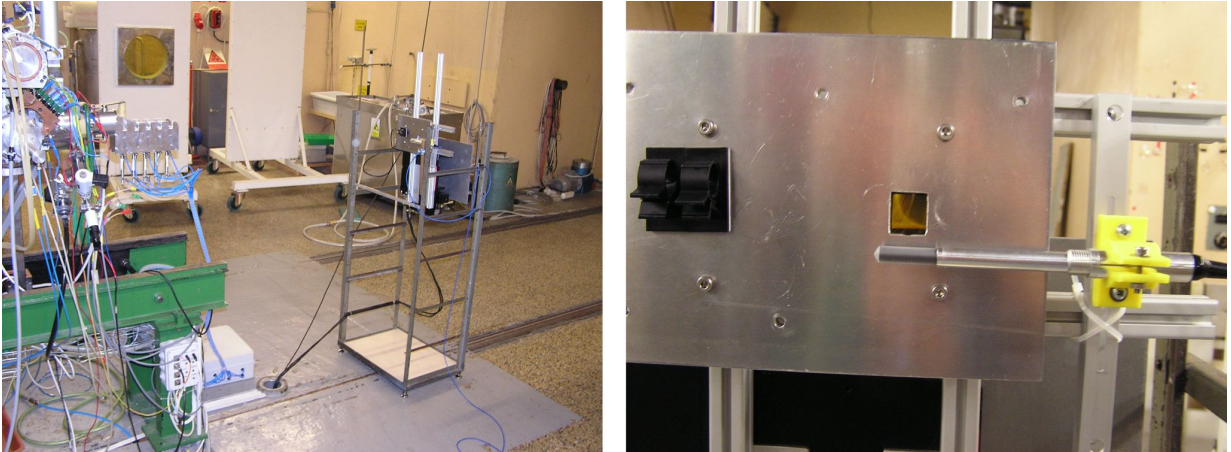


Figure 4.11: The experimental setup used for calibration of the ionization chamber by means of Timepix. Picture on the left shows the setup mounted on the movable X–Y cross table in front of the beam pipe terminated by the energy degrader. Cables from the setup run through the hole in the floor into the bunker. The right-hand side picture shows a detail of the ionization chamber and an 8 mm thick aluminum shielding plate, covering the Timepix detector electronics, with a window for the Timepix detector chip only.

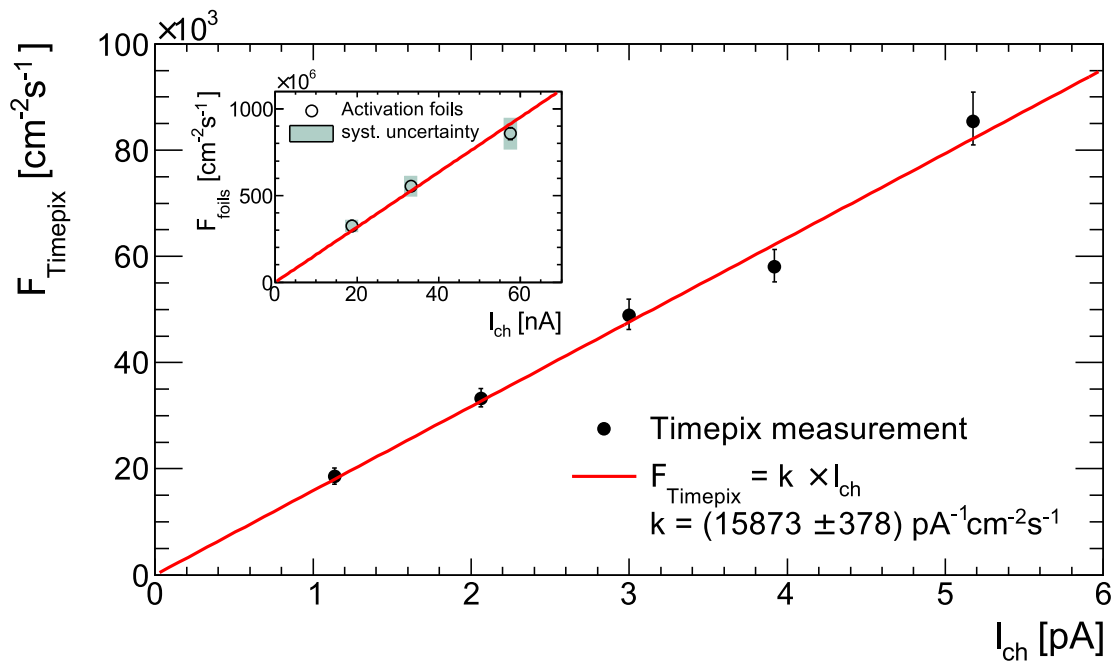


Figure 4.12: Correlation between the ionization chamber current I_{ch} and the corresponding proton flux F measured using Timepix, fitted with a linear function $F = k \times I_{ch}$ (red line). The embedded figure compares the measured relation between I_{ch} and F from activation foils with the extrapolated calibration curve obtained with Timepix. [99]

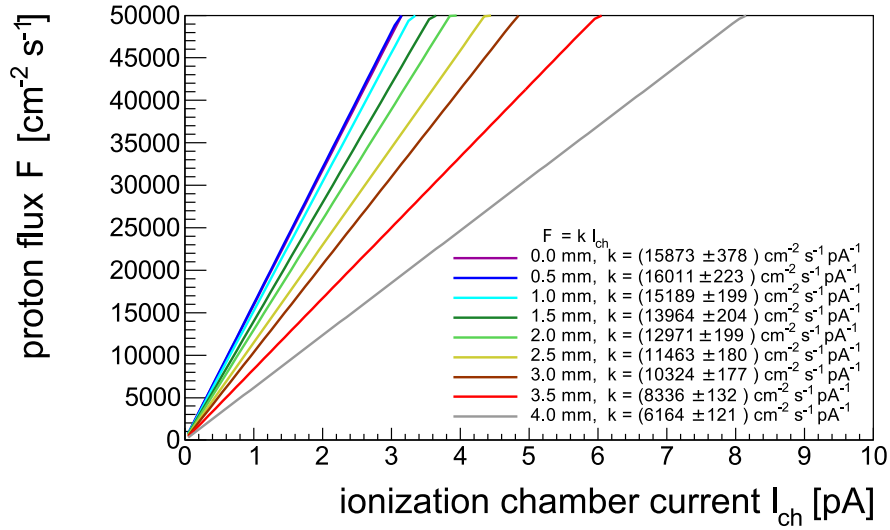


Figure 4.13: Proton flux versus ionization chamber current for different degrader configurations. The initial proton energy was 34.8 MeV, target was placed 130 cm away from the beam pipe exit window. Proton flux was measured using the Timepix detector. As the material budget placed to the beam increases, protons get slower and their ionization losses increase. Therefore the k factor gets smaller. Quoted errors are statistical only.

measured yields of reactions ${}^{\text{nat}}\text{Cu}(p,X){}^{62}\text{Zn}$ and ${}^{\text{nat}}\text{Cu}(p,X){}^{63}\text{Zn}$ and from the known cross section we calculated the flux. The resulting relation between the flux obtained using the activation foils method and ionization chamber current in the range of tens of nA is shown in the embedded figure in the top left part of Fig. 4.12. For even higher ionization chamber currents above 100 nA, activation foils indicate that the linearity is lost, see Fig. 4.14. This is a sign of a saturation effect in the ionization chamber.

Based on the presented data, we can say that the ionization chamber current is linearly dependent on the proton flux up to 100 nA. That fully covers the range of fluxes that are of our interest.

An approximate estimate of the k parameter value can be also obtained on the basis of a simple Geant4 simulation. The simulation calculates the mean energy deposited by protons in the working gas of the ionization chamber placed 130 cm away from the beam pipe exit window for initial proton energy 34.8 MeV. From the deposited energy $\overline{E}_{\text{dep}}$ it is possible to estimate the mean number of created electron-ion pairs by dividing the deposited energy by the mean value required to create one pair in the air, which equals $w = 34$ eV. If we further consider that the chamber has a cross section A , which is exposed to spatially uniform proton flux F , then the number created electron-ion pairs N will be

$$N = F \times A \times \frac{\overline{E}_{\text{dep}}}{w}. \quad (4.4)$$

The ionization current will be formed mainly by electrons due to their higher mobility.

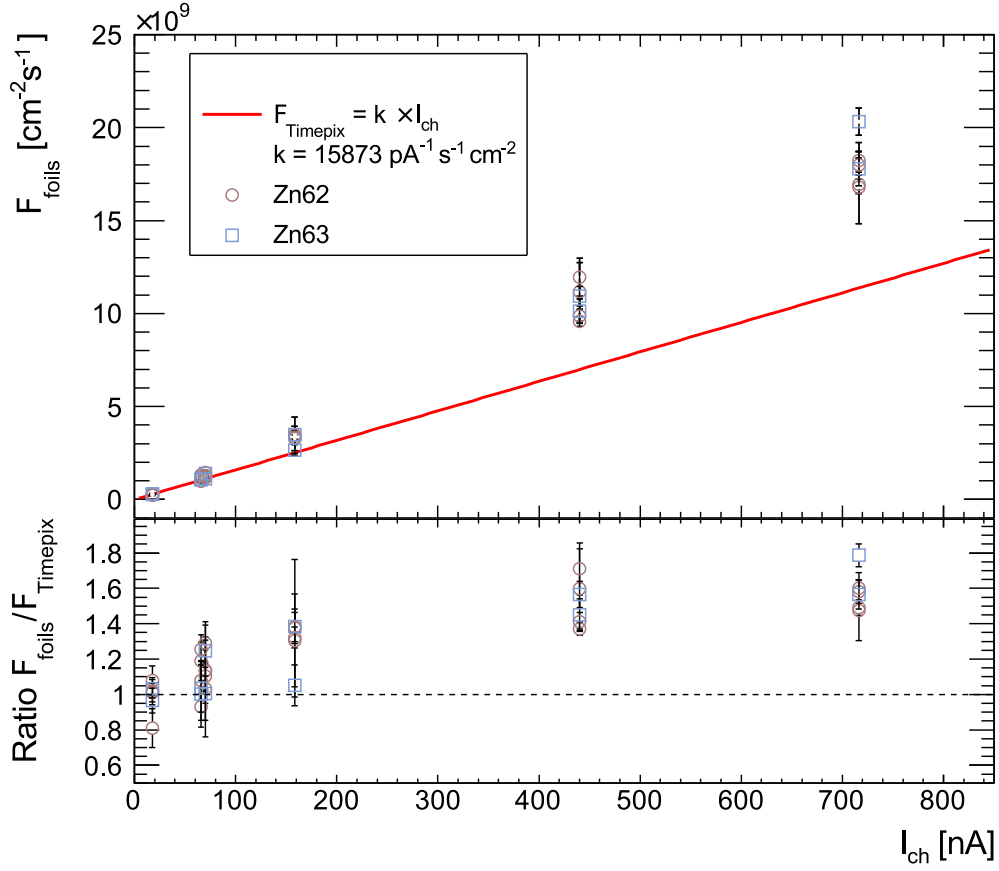


Figure 4.14: In the top part we can see the extrapolated parametrization $F = k \times I_{\text{ch}}$ from the Fig. 4.12 and the measured correlation between higher values of the ionization chamber current I_{ch} and proton flux F measured using activation foils. The bottom panel shows the ratio of the flux measured by the activation foil method to the extrapolated parametrization obtained using Timepix (red curve) in the upper panel. Credit: [99].

Since each electron carries elementary charge $e = 1.602 \times 10^{-19}$ C, the resulting ionization current will be

$$I_{\text{ch}} = e \times F \times A \times \frac{\overline{E_{\text{dep}}}}{w}. \quad (4.5)$$

Using 4.3 we see that

$$k = \frac{w}{\overline{E_{\text{dep}}} \times e \times A}. \quad (4.6)$$

For the initial proton energy of 34.8 MeV and no energy degrader plate in the beam, the mean energy loss in the ionization chamber is 7.956 keV. The corresponding calculated calibration factor k equals 1.78×10^{16} [$\text{A}^{-1} \text{cm}^{-2} \text{s}^{-1}$]. This value is in a good agreement (12%) with the k obtained from the measurement, providing us with confidence that simulations give realistic description of the setup. For lower energies, the agreement is

even better. A comparison of the simulated and measured k factors is in Tab. 4.2. The estimated uncertainty of the flux measurement is about 15%.

Degrader thickness [mm]	p energy at target [MeV]	$\overline{E}_{\text{dep}}$ [eV]	N	k [cm ⁻² s ⁻¹ pA ⁻¹]	
				simulated	measured
0.0	32.3	7 956	233	17 845	15 873
0.5	30.3	8 414	247	16 848	16 011
1.0	28.2	8 955	263	15 853	15 189
1.5	25.8	10 090	288	14 445	13 946
2.0	24.1	10 550	310	13 415	12 971
2.5	21.4	11 950	352	11 839	11 463
3.0	18.6	14 150	413	10 076	10 324
3.5	15.2	18 600	519	8 022	8 336
4.0	11.6	23 470	685	6 073	6 164

Table 4.2: Comparison of the calibration factors k for different degrader configurations, calculated from simulated data and obtained from the Timepix measurement. $\overline{E}_{\text{dep}}$ is the mean energy deposited by one proton in the ionization chamber and N is the mean number of electron-ion pairs created in the ionization chamber by one traversing proton. Both $\overline{E}_{\text{dep}}$ and N values are based on Geant4 simulations.

4.1.3 Estimation of the Energy Loss in Target Silicon Chip

When testing radiation hardness of silicon chips, it is essential to know the dose absorbed in the irradiated chip. The dose D absorbed by the chip can be calculated from the chip area a , proton fluence Φ , mean energy deposited in silicon die $\overline{E}_{\text{dep}}$ by one proton, proton (elementary) charge e , silicon density ρ_{Si} and chip thickness x :

$$\begin{aligned}
 D &= a [\text{cm}^2] \times \Phi [\text{cm}^{-2}] \times \frac{\overline{E}_{\text{dep}} [\text{eV}] \times e [\text{C}]}{\rho_{\text{Si}} [\text{kg}/\text{cm}^3] \times a [\text{cm}^2] \times x [\text{cm}]} = \\
 &= \Phi \times \frac{\overline{E}_{\text{dep}} \times e}{x \times \rho_{\text{Si}}} [\text{J}/\text{kg} = \text{Gy}].
 \end{aligned}
 \tag{4.7}$$

To get the dose in rad, we can simply multiple the value of D in gray by 100, since 100 rad equals to 1 Gy.

We can see from the equation above, that D is independent of a , provided that the fluence is homogeneous across the chip. Yet the formula requires as an input the thickness of the chip and the corresponding mean energy loss $\overline{E}_{\text{dep}}$. We will now make two assumptions, leading to a simpler prescription for dose:

1) The proton stopping power S equals to linear energy transfer LET .

This allows us to calculate the energy transferred into the chip material as a difference

of proton energies when entering the chip and when leaving it. The most significant component of a difference between S and LET is the radiative energy — bremsstrahlung. The loss by bremsstrahlung can be neglected for protons with energy below 50 MeV [23], since relative to other types of energy loses its contribution is less than 0.01 ‰. Thus we can safely consider $S = LET$.

2) The LET is constant along chip thickness x .

We know from the description of proton interaction with matter in Section 2.2.2, that the proton stopping power increases as the proton slows down, i.e. the energy deposition is not linear along the proton trajectory, see Fig. 4.15. But if we assume that the mean proton energy loss $\overline{E_{\text{dep}}}$ grows linearly with the increasing chip thickness x , we can use a constant LET parameter for the particular material (Si):

$$LET = \frac{d\overline{E_{\text{dep}}}}{dx} = \frac{\overline{E_{\text{dep}}}}{x}. \quad (4.8)$$

This approximation is valid for thin layers ($\lesssim 1$ mm) and proton energies $\gtrsim 25$ MeV only. From (4.7) it follows:

$$D = \Phi \times \frac{LET \times e}{\rho_{\text{Si}}} [\text{Gy}]. \quad (4.9)$$

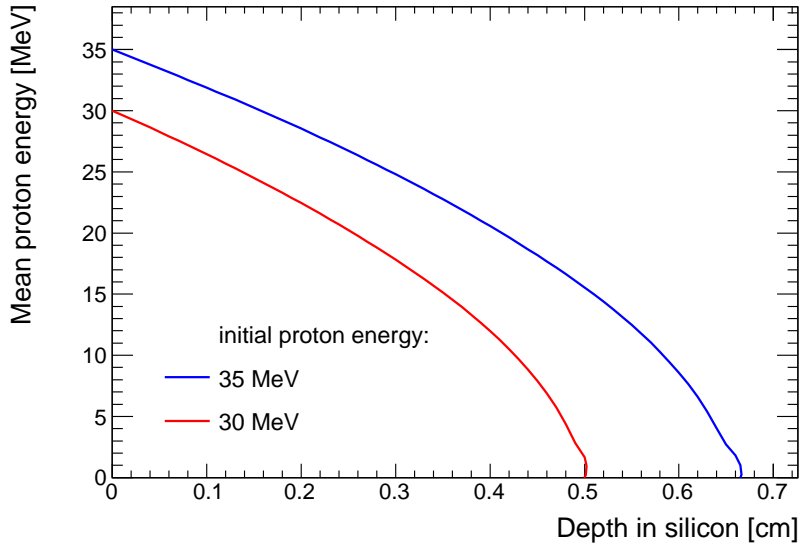


Figure 4.15: Mean energy of a proton as a function of a trajectory length in silicon. A result of Geant4 simulation.

Now, let's have a look on how big error was made by the assumption that LET is constant. Table 4.3 shows proton energies when entering and leaving a silicon die. The thickness of the die ranges from 50 μm to 1 mm. The simulation is made for a chip covered by a 500 μm thick package. The energy of a proton entering the package corresponds to the mean proton energy at the target area and is taken from the Table 4.1. The simulated

material of the package is Bismaleimide Triazine (BT) Resin [100] with density 1.16 g/cm^3 and empirical formula $\text{C}_1\text{H}_1\text{O}_1\text{N}_1$ [101]. Chip material is simulated as a pure silicon.

Degrader thickness [mm]	Mean proton energy \bar{E} [MeV]					
	when entering		when leaving Si die (die thickness)			
	package	Si die	50 μm	300 μm	500 μm	1000 μm
0	32.0	31.0	30.8	30.0	29.3	27.5
0.5	30.1	29.1	28.9	28.0	27.3	25.4
1.0	28.1	27.1	26.9	26.0	25.2	23.2
1.5	26.0	24.9	24.7	23.7	22.9	20.6
2.0	23.8	22.5	22.3	21.2	20.3	17.8
2.5	21.3	20.0	19.8	18.5	17.5	14.7
3.0	18.6	17.1	16.8	15.4	14.3	10.9
3.5	15.6	13.8	13.5	11.8	10.3	5.4
4.0	12.0	9.7	9.3	6.9	4.4	0.0
4.5	7.2	3.1	2.0	0.0	0.0	0.0

Table 4.3: Mean energies of protons when entering the silicon chip covered by a $500 \mu\text{m}$ thick BT resin package and when leaving it. Die thickness and degrader configuration were varied. The setup geometry with 130 cm of air between the degrader and target, shown in Fig. 4.5, was used. Initial proton energy was 34.5 MeV . Data are based on 10 000 runs of SRIM simulation.

Table 4.4 shows the average proton LET for different die thickness and degrader plate configuration calculated. Values are based on the data from Table 4.3. It also shows the average proton LET for the chip package. The last column gives the maximum relative error which we make if we use the average value of LET in $500 \mu\text{m}$ thick chip as an estimate of LET for chips having thickness between $50 \mu\text{m}$ and 1 mm . We can see that for proton energies above 25 MeV the relative error stays below 5% . This error gets however larger as proton energy gets smaller.

The same principle of average LET as for the silicon chip was used to assess the energy loss in the package. The assumed $500 \mu\text{m}$ thick package is the lowest estimation. The real package is likely to be thicker, so the energy loss in it can be expected to be greater.

4.2 Target Setup for Neutron Irradiation

We use a similar concept of the setup in case of neutron irradiation with a beam from FNG as for the proton irradiation. So far, we have used only the neutron source based on p-Be reactions, providing neutrons with energy spectrum ranging from 0 to 35 MeV and mean energy 14 MeV , see Section 2.6. The 1.5 m long FNG apparatus is attached at the end of the cyclotron negative mode beam pipe. Neutrons are generated from the beryllium target at its end and are emitted homogeneously in the direction away from the machine. The primary proton current hitting the FNG is high enough to be monitored by measuring

Degradation thickness [mm]	Proton [MeV] when entering package		Average LET [keV/ μm]					Max. relative error
	Si die	in package	in package	50 μm	300 μm	500 μm	1000 μm	
0	32.0	31.0	1.91	3.33	3.37	3.41	3.49	2.4 %
0.5	30.1	29.1	2.01	3.51	3.54	3.60	3.69	2.7 %
1.0	28.1	27.1	2.13	3.73	3.77	3.81	3.94	3.2 %
1.5	26.0	24.9	2.27	3.97	4.03	4.10	4.25	3.7 %
2.0	23.8	22.5	2.45	4.30	4.39	4.46	4.68	4.9 %
2.5	21.3	20.0	2.69	4.74	4.84	4.94	5.26	6.4 %
3.0	18.6	17.1	3.02	5.34	5.53	5.70	6.23	9.4 %
3.5	15.6	13.8	3.54	6.32	6.66	6.99	8.35	19.6 %
4.0	12.0	9.7	4.52	8.37	9.30	10.53	*	>20.5 %
4.5	7.2	3.1	8.19	21.96	*	*	*	

Table 4.4: Average LET values of a proton in the package and in the silicon chip for different die thickness and degrader configuration influencing the mean energy \bar{E} of the incoming proton. The last column gives a maximum error if a value of LET in 500 μm thick chip is used for a chip of thickness between 50 μm and 1 mm. Data are based on Table 4.3.

*: The proton was completely stopped before reaching the end of the die. Thus the average LET value for this thickness would not make sense.

the current from the stripping foil. The dependence of the emitted neutron flux on the primary proton current is linear [53], but might change in the long-term due to aging of the beryllium target.

4.2.1 Initial Calibration Measurement

A set of activation foils was placed at the position 156 mm away from the FNG during the irradiation. They were used to determine the total neutron fluence during the irradiation ex post, using the activation analysis method [54]. Again our ionization chamber was used to monitor the instantaneous flux on-line. Neutrons do not ionize directly, they have to interact with another particle or an atomic nucleus to emit a directly ionizing particle such as α or proton. Because neutrons do not have an electric charge, they are not influenced by electric forces and the only way they can interact is via a nuclear reaction. Thus the current, which can a neutron passing through a ionization chamber induce, is much smaller when compared to a proton, and is practically non-measurable. It is therefore appropriate to supplement the chamber with a piece of material, where neutrons can interact and produce directly ionizing particles, to increase the ionization current. The ionization chamber was thus used inside its protective cover made of PMMA.

The target setup with the ionization chamber in its PMMA cover was placed in four different positions successively. In each position, response of the chamber was measured for several values of the primary proton current. The dependence of the measured ionization

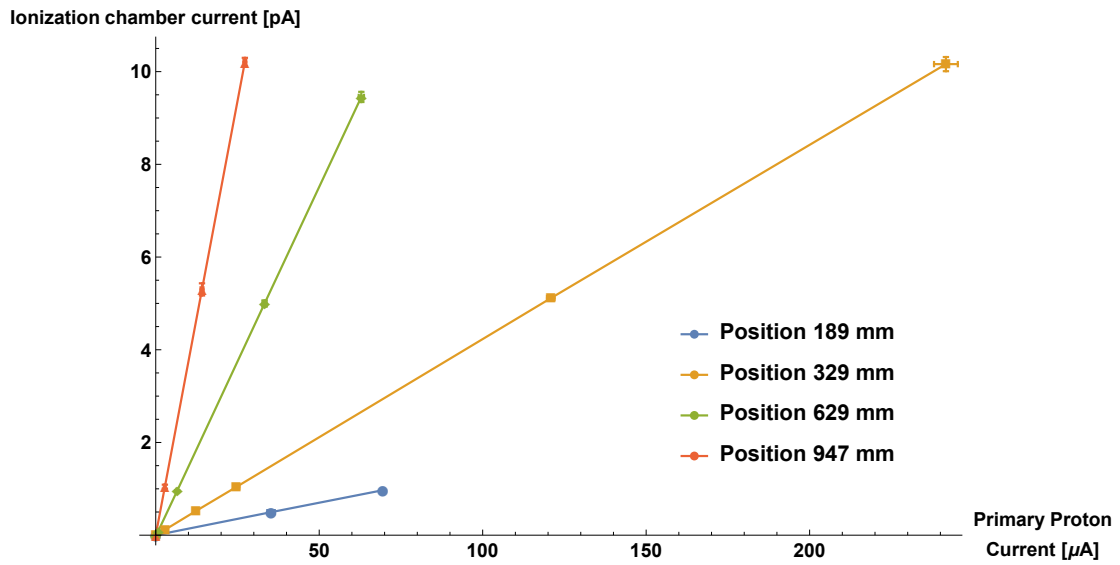


Figure 4.16: Ionization chamber current as a function of the primary proton current for different distances from the FNG. Data are parametrized with first order polynomials.

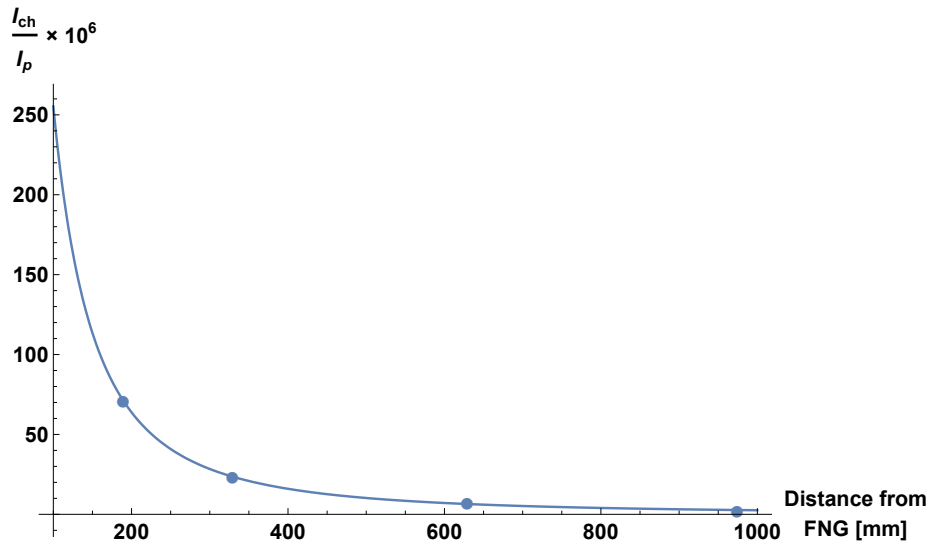


Figure 4.17: Ratio of ionization chamber current I_{ch} and primary proton current I_p as a function of the distance from the FNG. The data are fitted with $\frac{I_{ch}}{I_p} = 2.55 \times r^{-2}$ where r is the distance from FNG in mm.

chamber current on the primary proton current was found to be linear in each of the four positions, see Fig. 4.16. The neutron flux should decrease with the square of distance from FNG, assuming the Be target as a point-like source of neutrons. This is supported by Fig. 4.17 where we show the ratio of I_{ch} to the primary proton current as a function of the distance from FNG. The data is well approximated with the inverse square distance dependence. Based on Fig. 4.16 and Fig. 4.17 we can claim that the ionization chamber response to the incoming neutron flux is linear.

The profile of the neutron beam was found to be homogeneous within the range of the moving platform — potential variations in the measured ionization current were under the resolution of the measuring device.

The activation foils were analyzed by the FNG group. They found that the ratio of neutron flux in the position 156 mm from the FNG $F_{\text{neutron}}|_{156}$ to the primary proton current I_{p} over the whole irradiation time was

$$\frac{F_{\text{neutron}}|_{156}}{I_{\text{p}}} = 2.04 \times 10^{14} [\text{cm}^{-2} \text{s}^{-1} \text{A}^{-1}]. \quad (4.10)$$

This value differs by a factor of 1.06 relative to the value, which was determined by the same method three years earlier [53]. Based on the data in Fig. 4.17, I found that the corresponding ratio of the ionization chamber current I_{ch} to the primary proton current I_{p} at 156 mm from the FNG is

$$\frac{I_{\text{ch}}|_{156}}{I_{\text{p}}} = 1.05 \times 10^{-4}. \quad (4.11)$$

Thus, the calibration factor k for the neutron flux in any distance from the FNG equals

$$k = \frac{F_{\text{neutron}}|_{156}}{I_{\text{ch}}|_{156}} = 1.94 \times 10^{18} [\text{A}^{-1} \text{cm}^{-2} \text{s}^{-1}], \quad (4.12)$$

where F_{neutron} is the neutron flux and I_{ch} is the ionization chamber current.

The measured value of k is approximative only and its estimated systematic error is about 20%. Multiple measurements would be needed to obtain more precise value. The measurement has shown that it is possible to use FNG as a neutron source to irradiate electronics and at the same time have a reasonable on-line monitoring of the neutron flux using the same tools which are utilized for monitoring the proton flux.

4.3 Target Setup for Gamma Irradiation

The target setup for gamma irradiation was a simple stand holding a circuit board with irradiated FPGA, see Fig. 2.29. The ^{60}Co source apparatus described in Section 2.7 has a possibility of target alignment using an optical aiming director. Moreover, the gamma beam is wide enough to cover uniformly the whole board, thus the precise positioning is not crucial. The radiation was monitored using the ionization chamber again. Decrease of the source activity with the time is only minor and is apparent on the bottom margin of the ionization chamber resolution after at least ≈ 1 hour exposition.

4. NPI INFRASTRUCTURE EXTENSIONS

The activity of the ^{60}Co source was measured on 23rd April 2014 and was found to be 123.4 TBq. Its activity decreased to 106.9 TBq by the date of our measurement (8th June 2015). This was estimated from

$$A_m = A_c \times \exp\left(-\frac{\ln(2)}{T_{1/2}} \times (t_m - t_c)\right) [\text{Bq}], \quad (4.13)$$

where A_m is the activity at the time t_m , A_c is the activity in the moment of calibration t_c , and $T_{1/2}$ is a half-life of ^{60}Co .

One decay of ^{60}Co emits two photons, one with an energy of 1173 keV and one with energy 1332 keV. Assuming that the ^{60}Co source can be approximated as a point-like source, the gamma flux drops with the distance squared. We can calculate the flux F_γ of photons with a mean energy of $\frac{1173+1332}{2}$ keV at the distance r from the activity A_m and the mean number of γ particles emitted in one decay n as:

$$F_\gamma = A_m \times n \times \frac{1}{4\pi \times r^2} [\text{cm}^{-2} \text{s}^{-1}]. \quad (4.14)$$

For ^{60}Co we took $n = 2$.

Dependability and Characterization Measurements

This chapter describes our approach in the methods of measuring radiation related dependability parameters of FPGAs and ALPIDE chips as well as measurements required to characterize the behavior of the ALPIDE prototype detectors in the proton beam. A new method of measuring a SEU cross section in the configuration memory and DFFs of any FPGA was developed and tested using beams of protons, neutrons and gammas.

5.1 SEE in FPGAs

A common way of detecting SEUs in FPGA is using the bitstream readout, which can be described as follows. Any valid bitstream is loaded into the chip and read out periodically during the irradiation. By comparing the original (golden) bitstream with the one which was read out, it is possible to determine the exact number of faults in the configuration memory within the period between loading the bitstream and reading it back. However, this method is usually not able to detect faults in DFF, since their actual content is typically not a part of the bitstream.

The only way to detect a fault in the chips which do not have the possibility to read the bitstream back is by observing an output of the loaded circuit. Because such chips were also required to be tested, I have designed and developed a method how to detect faults also in FPGAs without the bitstream readout possibility.

5.1.1 Testing Circuit Design

My design of the testing circuit [A.7, A.5] is optimized to be used on FPGAs with a LUT and a DFF in one logic cell, as it is shown in Fig. 2.1. It can, however, be used for other FPGA architectures as well. The only requirement is, that it is possible to select the initial value of each flip-flop in the FPGA upon reset.

The schematic connection of the testing circuit for a 4-input-LUT-based FPGA is shown in Fig. 5.1. It is a long circular shift register, or a pipeline, which has no input and just one output. Its data word width is equal to the number of LUT inputs in a given FPGA. Every stage of the pipeline is identical and performs a conversion of data word between two encodings. The conversion C has the feature, that if it is applied twice on the word x , the output of the second conversion equals the input of the first one:

$$C(C(x)) = x. \tag{5.1}$$

The stage performing the conversion consists of i functions of i variables, one for each bit of the code word, performed by exactly one LUT. Functions have to be irreducible to force the synthesis tool to use all inputs of the LUT. An example of a possible conversion function for 4-input LUTs is given in Table 5.1. By applying a trivial test¹ to all LUTs, all their bits are tested.

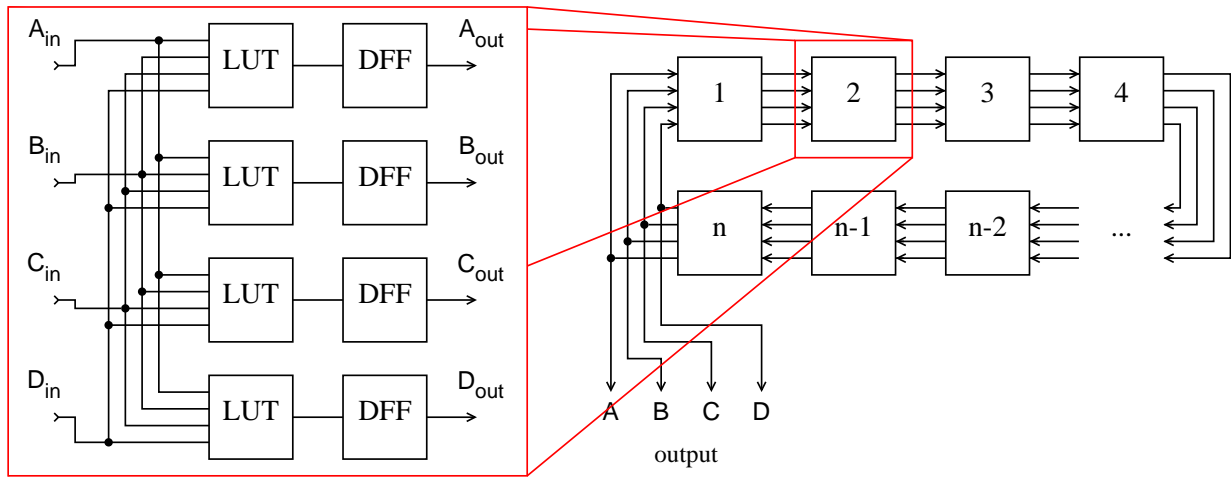


Figure 5.1: Right: Schematic connection of the testing circuit pipeline for 4-input LUTs. Left: A detail of one stage. All stages are identical and each of them completely occupies 4 LUTs. Each of these LUTs is evaluating one bit (A, B, C or D) of the next code word to be stored in the corresponding DFFs.

Let us suppose that the pipeline has $n = 2^i$ stages. Since it is i bits wide, every stage occupies i LUTs and i DFFs. The whole pipeline thus occupies $2^i \times i$ LUTs and the same number of DFFs. We can pre-load the data words into the pipeline by selecting the initial values of all DFFs. These data words will be shifted by one stage every clock cycle, while their encoding will alter between the two used codes. Since the pipeline is circular, data will circulate in the pipeline forever. If we pre-load the data in such a way, that they can be observed at the output as a sequence of all 2^i possible values, a complete trivial test of all used LUTs will be performed in $n + 2^i$ clock cycles. To make the evaluation

¹A trivial test is a sequence of 2^i input vectors, which contains all possible combinations of i input variables.

In	Out	In	Out	In	Out	In	Out	
0000	↔	1001	0100	↔	0011	1000	↔	1011
0001	↔	1010	0101	↔	0111	1001	↔	0000
0010	↔	1111	0110	↔	1100	1010	↔	0001
0011	↔	0110	0111	↔	0101	1011	↔	1000

Table 5.1: Example of an irreducible conversion function C for testing 4-input LUTs, fulfilling the requirement that $C(C(x)) = x$.

easier, the preloaded data create a Gray code [102] sequence at the output, see Fig. 5.2. By comparing the real output to the expected one, we can determine, whether the circuit is working correctly or not. The evaluation of the output will be described later together with a method that distinguishes between errors in DFF and configuration memory. The designed circuit is sensitive to all faults in all used LUTs and DFFs. The coverage of the routing network configuration and other configuration bits is not well defined though. However, no circuit can utilize 100% of the FPGA resources, nor be sensitive to faults on all configuration bits. According to [103], only 5% of SEUs in the FPGA will have an effect on the circuit behavior in an average design. In the worst case it should never exceed 10%.

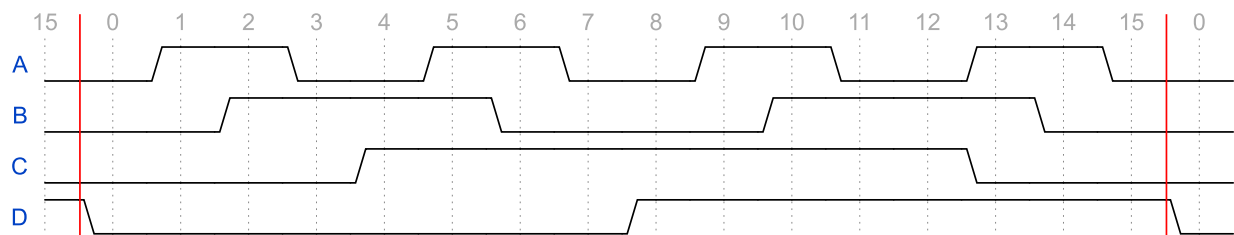


Figure 5.2: Output of the testing circuit. The waveform between the red lines represents a trivial test of LUTs and DFFs in one stage in the Gray code. The characteristic property of the Gray code is that only one bit changes in consecutive data words. Each word is marked with a number 0–15.

We will describe how to fill the whole FPGA with the testing circuit now. If the number of available logic cells in the FPGA is a multiple of $2^i \times i$, the above mentioned 2^i stages long segment can be simply copied one by one until it fills the whole chip with the circuit. Otherwise one incomplete segment has to be added. The last stage in this incomplete segment has to perform a different function, replacing the missing stages. This will ensure the consistent output flow. In some cases, depending on the particular function it performs, this stage might not be sensitive to all faults in LUT content.

If the number of logic cells is not divisible even by the number of LUT inputs i , remaining logic cells (less than i cells) will not be used at all. In all cases, the sequence length needed to test all stages will be equal to $n + 2^i$, where n is the number of pipeline stages and i is the data word width corresponding to the number of LUT inputs.

The proposed testing circuit allows to distinguish between a fault in the DFF, or in the configuration memory, provided that the mean fault rate is much lower than the period of the whole pipeline turnaround. The principle of distinguishing between faults in different parts of the FPGA can be following:

- If the observed sequence contains one wrong word only, it originates from a single fault in DFF. Since the pipeline is circled, it appears again after the pipeline turnaround period, otherwise it was an error in communication with the evaluating device. The error disappears when the DFFs in the circuit are reset to the initial state. The bitstream does not need to be reloaded.
- If one wrong word repeats with the period of one segment length (2^i), its source is a single fault in a LUT content. Bitstream reload is required to correct the error.
- If there are more wrong words in the output sequence repeating with the same 2^i period, multiple faults in the configuration memory have occurred. Bitstream reload is required to correct the error.
- If the output is continuously wrong or errors repeat with a different period than 2^i , a fault corrupting the clock distribution network, creating a loopback on a routing network or some other serious fault has occurred. Bitstream reload is required to correct the error.

It should be possible to change the size of the fault-sensitive part of the configuration memory, used for routing and interconnections by constraining the placement of logical blocks in an FPGA, e.g. by means of a design tool. If the blocks are placed as they logically follow, the utilized interconnection resources are very low, so the circuit should be less sensitive to faults in it. On the other hand, if following blocks are placed far away, their interconnections utilize a large portion of the routing network, making the circuit more sensitive to faults. An estimate of SEE cross section corresponding to the routing network could be made by comparing error rates for both cases. However, this technique has not been tested yet.

5.1.1.1 Evaluation Device

The output of the testing circuit has to be evaluated in another device because the testing circuit utilizes the whole FPGA. It is of course possible to make the testing circuit smaller and to place the evaluation device (ED) into the remaining space of the same FPGA. Then the fault coverage is lower and there is a risk of ED failing due to a SEE. Hence, I used an external ED for our tests. The output of the tested FPGA was converted to differential signals using external LVDS drivers and sent through twisted-pair cables to a remote ED. There it was automatically evaluated and the number of detected failures was counted. The ED was based on the Digilent Spartan-3 Starter Board [104], equipped with the XC3S200 FPGA, to which a custom made external communication board with differential receivers and transmitters was connected, see Fig. 5.3. It received the output from the tested device

and compared it to the expected predefined sequence. For timing synchronization the characteristic property of the Gray code was used — two subsequent words differ in one bit exactly. Thus the phase-locked loop at the receiver side was synchronized each time an input bit changed within the allowed time window. If it changed outside that window or an unexpected bit was changed, a fault was detected. The ED was able to automatically reset the tested device or reload its configuration remotely, so the automatic fault distinguishing mechanism could be implemented into it using the methods described in the previous subsection. It counted the number of detected faults separately for each category and sent logs into the connected PC via a serial line.



Figure 5.3: Digilent Spartan-3 Starter Board (right-hand side) connected to a custom-made communication board with differential transmitters and receivers and 4 connectors for twisted-pair cables (left-hand side). One device was used for evaluating the SEE in a tested FPGA and the second as a DUT in tests of the Spartan-3 FPGA.

5.1.2 SEE Measurements

First we will describe an experimental lay-out which was used for SEE cross section measurement and show the raw results. Later, in the Section 5.1.4, we will discuss the results. The proposed test methods were verified using the SRAM-based Xilinx Spartan-3 fabricated using 90 nm technology as the device under test (DUT). I used the same type of the Digilent Spartan-3 Starter Board, equipped with the XC3S200 FPGA, as was used for the evaluation. To reduce the risk of failure in other components on the board due to radiation, the board was shielded with an 8 mm thick aluminum plate with a hole for the tested FPGA chip only, see Fig. 5.4.

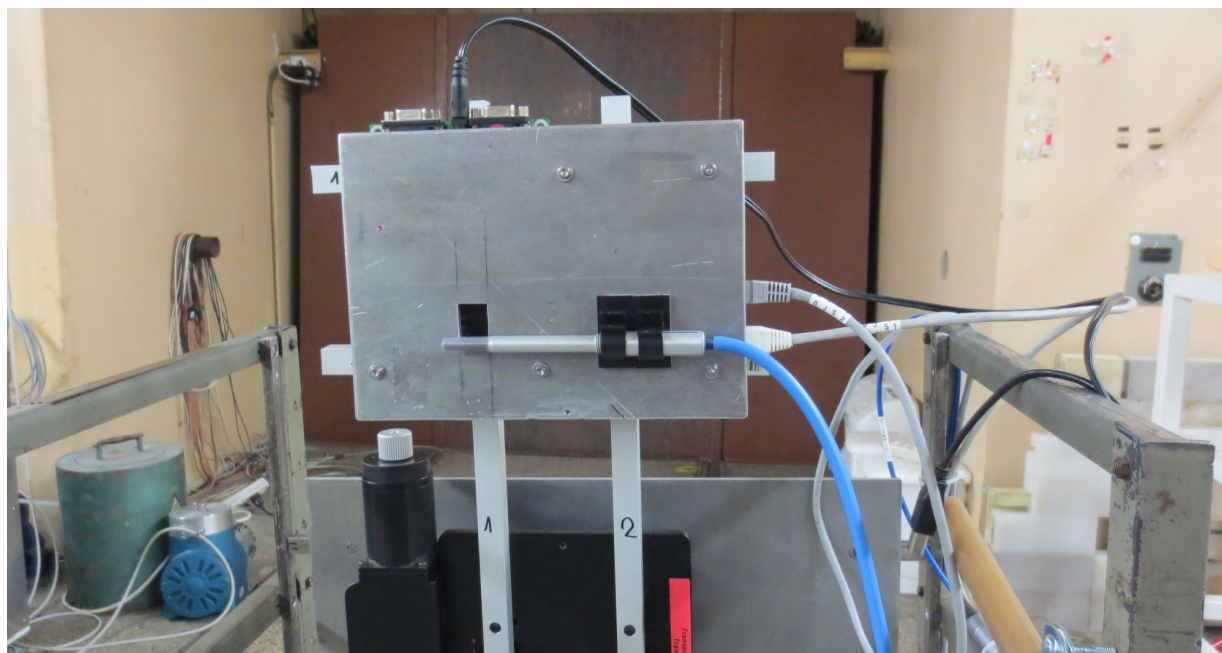


Figure 5.4: The target setup for irradiation of the Spartan-3 chip. The circuit board is shielded with an aluminum plate with a hole in the place of the tested FPGA. The ionization chamber, which measured proton flux, is attached below the hole.

5.1.2.1 Measurement of SEE Cross section for Protons, Neutrons and Gammas

The DUT was exposed to proton beam provided by the NPI cyclotron in the first series of experiments. Energy of the protons was varied using the degrader unit. The DUT was placed 130 cm from the beam pipe exit window. I present the measured cross sections of SEE in configuration memory and in DFFs, respectively, calculated according to (2.18) in Fig. 5.5 and in Fig. 5.6. The corresponding number of sensitive bits used for the cross section calculation was exactly 3650 for DFFs and it was estimated to be 500 000 for the configuration memory. Data show a clear rise with the energy with a possible onset of saturation around 20 MeV. The quoted error bars give a statistical uncertainty for cross section and a variance for proton energy.

A similar measurement was carried out also using neutron beam generated by FNG with the Be target. The mean energy of the neutron beam was 14 MeV and its energy spectrum shown in Fig. 2.28 was reaching up to 34 MeV [54]. The DUT was placed at 329, 629 and 947 mm from the FNG. In each position the cross sections was constant, and the fault rate correspond to the neutron flux intensity dependence on the square of the distance from the FNG. The corresponding average cross section is quoted in Fig. 5.5 and 5.6 and is comparable with the proton data. Used particle fluxes varied from approx. 10^6 to $10^8 \text{ cm}^{-2} \text{ s}^{-1}$ both for neutrons and for protons. Results are published in [A.3].

The SEE measurement was performed also with the NPI ^{60}Co gamma source, described

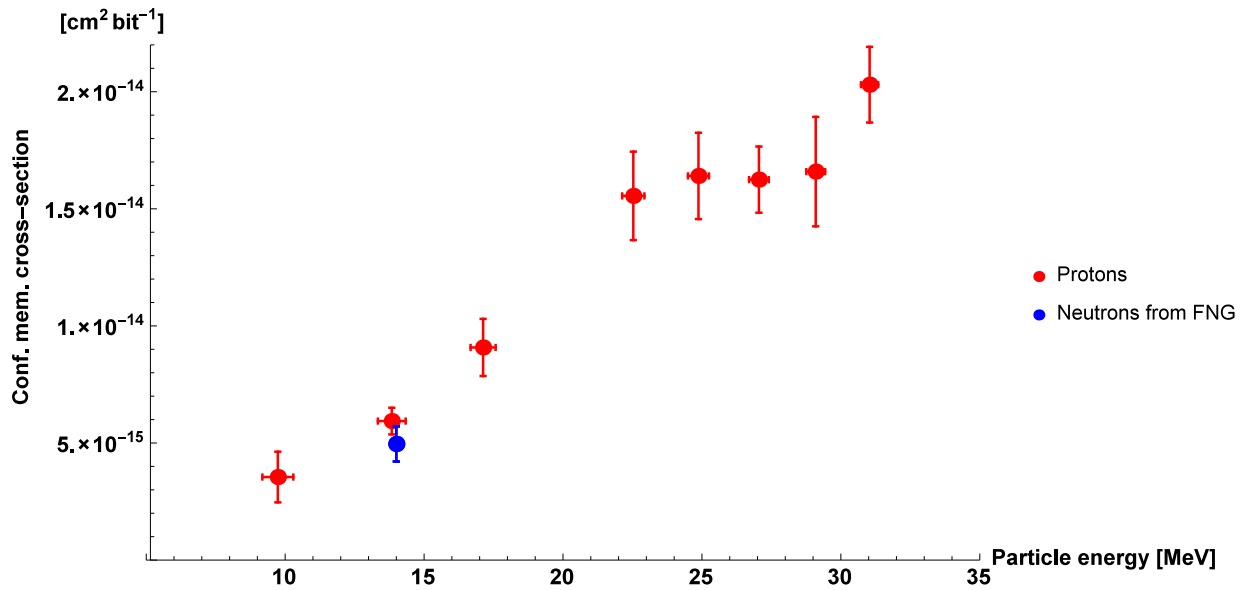


Figure 5.5: Measured SEE cross sections for configuration memory of Spartan-3 (XC3S200) FPGA using proton beam of various energies and neutrons from the FNG with the mean energy of 14 MeV. The estimated number of memory bits used in the configuration memory was 500 000.

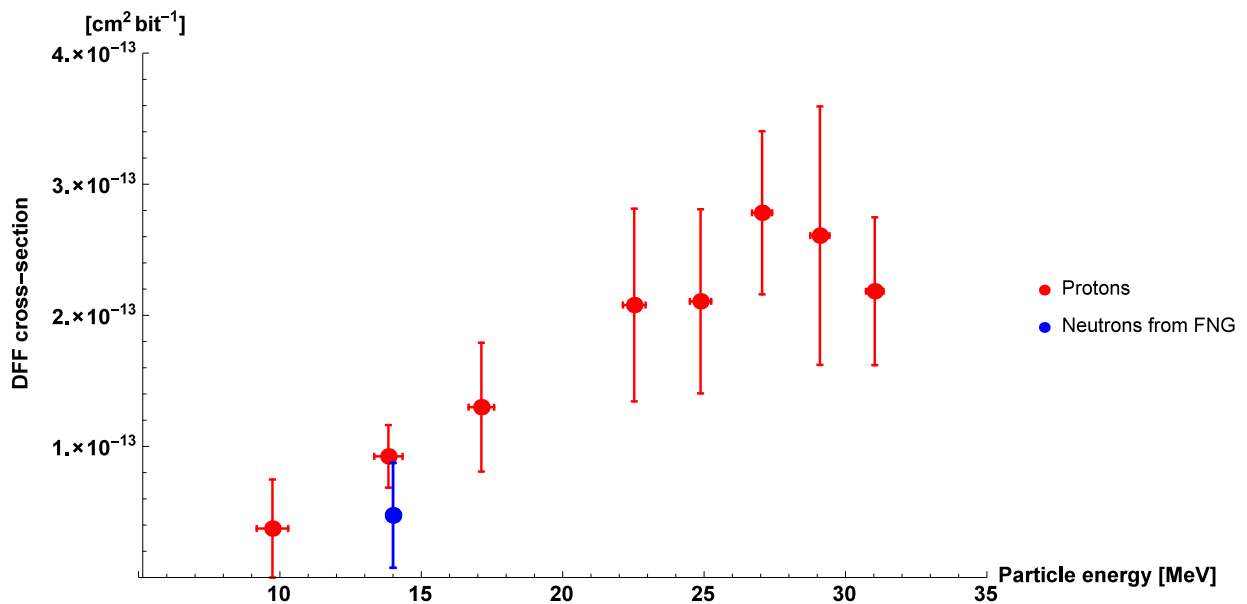


Figure 5.6: Measured SEE cross sections for DFFs of Spartan-3 (XC3S200) FPGA using proton beam of various energies and neutrons from the FNG with the mean energy of 14 MeV. The number of used DFFs was exactly 3650 — all available in the FPGA.

in Sec. 2.7. The first measurement was performed in the distance of 1000 mm from the gamma source and took 4046 s. Then the distance was set to 500 mm and the measurement continued for 8876 s. The activity of the ^{60}Co source was 106.9 TBq. The obtained ionizing dose during the measurement was approximately 13 krad. There was no SEU observed in this case, up to the gamma (photon) fluence of $6.7 \times 10^{13} \text{ cm}^{-2}$. Thus the estimated upper limit of the cross section on ^{60}Co γ is approximately $4 \times 10^{-18} \text{ cm}^2 \text{ bit}^{-1}$ for DFF and $3 \times 10^{-20} \text{ cm}^2 \text{ bit}^{-1}$ for the configuration memory.

5.1.2.2 SEE rate vs. Clock Phase

Measurement of transient events in FPGA has not been described in literature to our knowledge yet. I proposed a setup to study a potential transient events, which is illustrated in Fig. 5.7. We were able to affect at which phase of the clock cycle protons arrive to the chip using this setup. Transient events should be seen at most when protons arrive close to the clock edge and they are captured by the following DFF. If protons arrive too early, transient events are likely to subside. I can also imagine, that the increased power consumption at the time of a clock transition might influence also the sensitivity of memory cells to a SEU, for example if the power supply voltage locally drops due to the increased current consumption and the energy required to change the state of the memory cell lowers for a while.

The cyclotron provided protons with energy 34.8 MeV during this measurement. The setup with the SRAM-based XC3S200 FPGA was placed in the usual position, 130 cm away from the beam pipe exit window.

The output of the cyclotron radiofrequency generator was brought out and connected to the synchronization and trigger input of the Agilent 33250A function generator [105]. The function generator was set to the same frequency as the cyclotron RF generator, with the possibility to adjust their relative phase. Its output was used as a clock input of the DUT which then run on the same frequency as the cyclotron. The rest of the connections were the same as in the standard setup, see Fig. 4.1.

I used a scintillator coupled with a photomultiplier (PMT), placed next to the tested FPGA, to measure the relative delay on all signals and in the acceleration process and to determine the zero phase shift. Proton passing the scintillator generate photons, which were registered by the photomultiplier. The maximal time resolution of the used scintillator and PMT is 20 ns, corresponding to 50 MHz. That is enough to distinguish separate bunches from the cyclotron which was operated at the maximum frequency of approximately 25.8 MHz. The delay of a signal from PMT and to the clock input of the DUT on 40 m coaxial cables was measured to be 165 ns on each cable. We could check the relative phase of the clock and PMT signals and determine the zero phase using the oscilloscope. The zero phase shift thus means that the clock signal comes $2 \times 165 \text{ ns}$ before the PMT signal. The scintillator with PMT were used only for determining the zero phase using a low intensity proton flux ($\approx 10^3 \text{ cm}^{-2} \text{ s}^{-1}$) and were removed for the measurement of SEE with higher flux. The phase alignment has to be considered as an approximative only, since the delay of the PMT was not considered in the measurement and some other timing paramet-

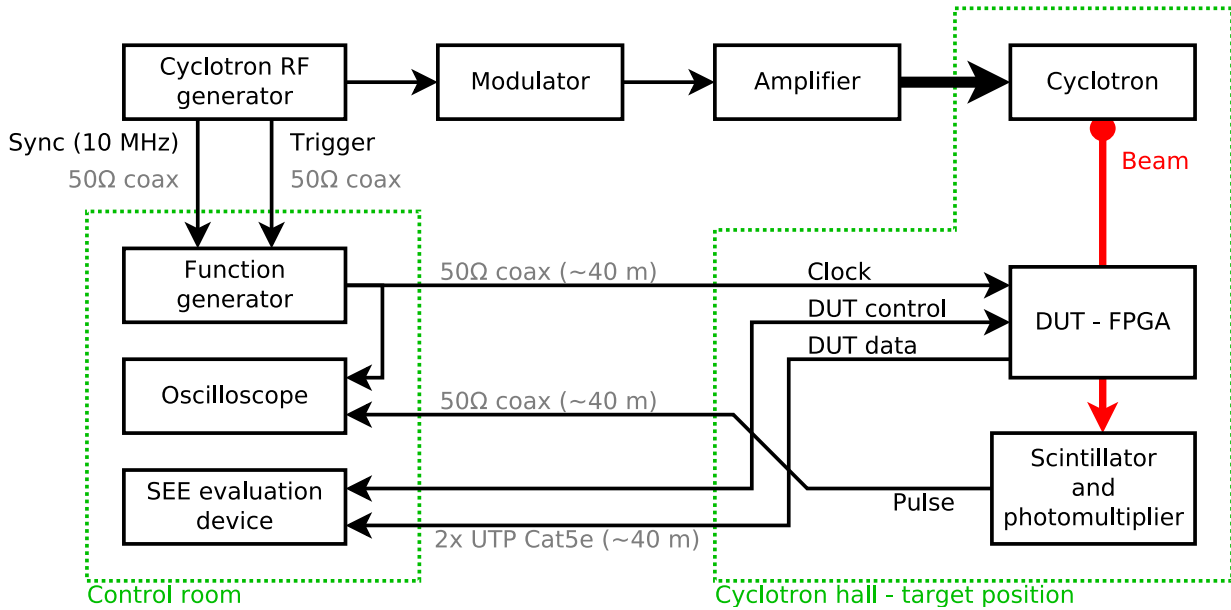


Figure 5.7: Setup for measurement of transient events effects. Clock frequency of the DUT is synchronized with the cyclotron RF generator determining the frequency of proton bunches. It is possible to select the exact time within the clock period when the protons arrive to the chip by shifting the clock phase against the cyclotron frequency. The scintillator was used only for initial aligning of the phase using a very low proton flux and was not present during the measurement.

ers of the proton beam might have changed when switching to higher fluxes used for SEE measurement. The proton flux used for measuring the SEE was about $5 \times 10^7 \text{ cm}^{-2} \text{ s}^{-1}$.

The time distribution of protons in a cyclotron bunch is shown in Fig. 5.8. It was simulated numerically [106] and cross-checked with an indicative measurement using the PMT signal. The bunch length was approximately 6 ns, which is about 1/6 of the 38.8 ns bunch period. The design loaded in the FPGA, running at 25.8 MHz, was synthesized to run at 150 MHz. That corresponds to the longest combinatorial path delay of about 6 ns. Thus the transient events should not influence the circuit, if their effects subside at latest 6 ns before the clock signal.

The dependence of the SEE cross section on the clock phase was measured in two independent runs. Both measurements were made with the phase shifting step of 36° (0.1 period), corresponding to about 3.9 ns. One measurement started at the phase shift of 0° and the second started at the phase shift of 18° . The measured cross sections are shown in Fig. 5.9.

5.1.2.3 SEE in Flash-Based FPGA

A flash-based Microsemi SmartFusion2 [107] fabricated using a 65 nm technology was also tested for SEE. SmartFusion2 is a System-on-Chip (SoC) device, containing an FPGA

5. DEPENDABILITY AND CHARACTERIZATION MEASUREMENTS

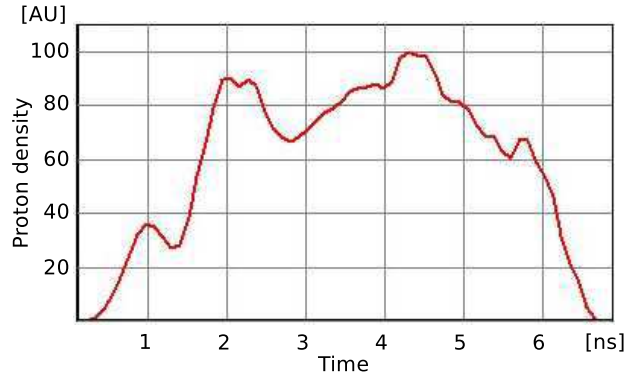


Figure 5.8: Simulated time distribution of proton density in a cyclotron bunch for the energy 34.8 MeV. The corresponding bunch period (cyclotron frequency) is 38.8 ns (25.8 MHz). Credit: [106].

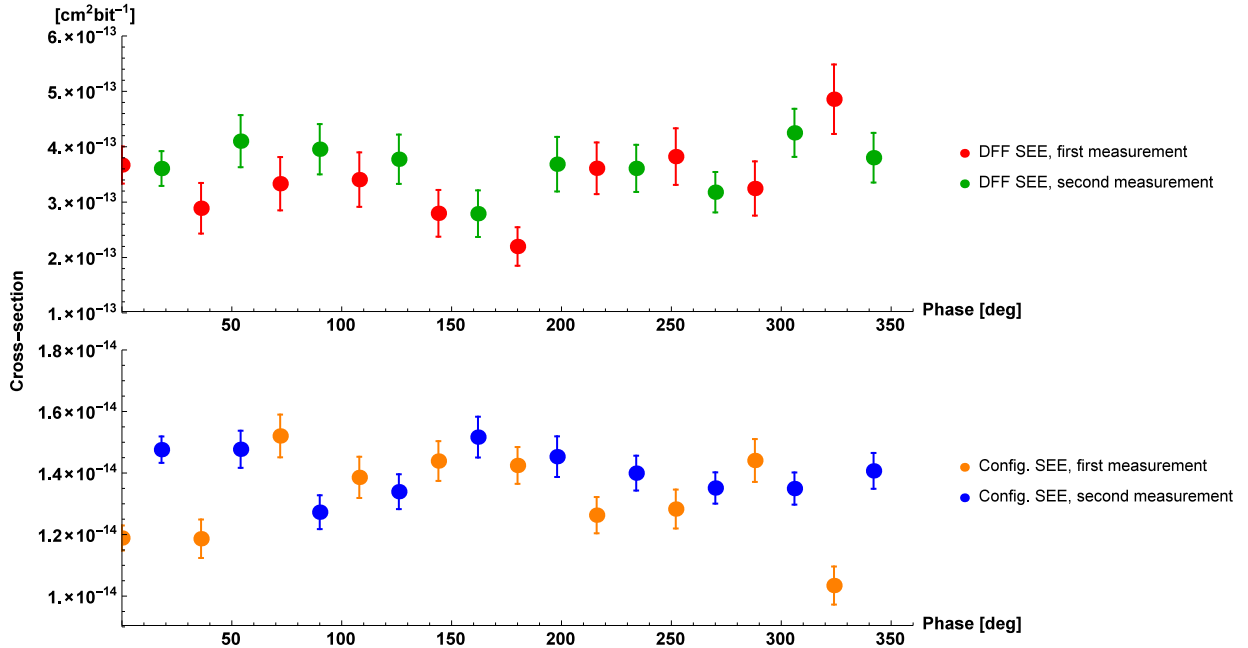


Figure 5.9: Measured SEE cross sections of the configuration memory and DFF in the Spartan-3 (XC3S200) FPGA induced by ≈ 32 MeV protons, coming in different phases of the clock cycle. Error bars show the standard deviation derived from the number of measured SEEs. The whole period corresponds to 38.8 ns.

fabric, ARM processor core, SRAM memory and other peripherals. Only the FPGA part of the device was tested for SEE using protons. No errors were observed in the flash configuration memory during the whole testing. However, errors in DFFs were observed. The SEE cross section was measured for three energies and the results are presented in Table 5.2. All 56 340 DFFs present in the device were utilized during the measurement.

Proton energy at target [MeV]	Total fluence [cm ⁻²]	Obtained TID [krad]	SEE cross section [cm ² bit ⁻¹]	
			conf. mem.	DFFs
32	1×10^{11}	27	0	$(2.2 \pm 0.2) \times 10^{-14}$
26	8×10^{10}	32	0	$(2.0 \pm 0.2) \times 10^{-14}$
15	5×10^{10}	27	0	0

Table 5.2: Measured proton beam cross section in the configuration memory and DFFs of the flash-based SmartFusion2 (M2S050) SoC FPGA fabric.

5.1.3 Total Dose Effects

Although no SEEs were observed in the configuration memory of flash-based FPGAs, they turned out to be more sensitive to the long-term radiation effects. The tested SRAM FPGAs obtained ionizing doses in order ranging from $\approx 10^4$ to $\approx 10^5$ rad and no difference in their performance was observed. On the other hand, all tested flash-based FPGAs were permanently damaged after obtaining a TID by order of 10^3 to 10^4 rad (depending on the particular FPGA type).

The behavior of all flash-based FPGAs after an irradiation was similar. The loaded design worked fine, until an attempt to reprogram the configuration memory was made. The memory was successfully erased, but it was not possible to write it again. Based on the behavior and a communication with the manufacturer, the most likely source of the problem were the transistors in the charge pump circuit, providing the programming voltage for the memory. Their threshold was shifted due to an excessive free charge accumulated inside the gate oxide, released there by ionizing radiation.

Similar observations were made also by a team preparing the upgrade of another ALICE subdetector (TPC). They were using the SmartFusion2 SoC device, built on the same technology and having the same FPGA fabric as Iglou2 [108].

Because of the resistance of its configuration memory to SEE, the flash-based FPGA, namely Microsemi Iglou2, was one of the candidates to be used in the Readout Unit of the upgraded ITS. Thus it was required to measure whether it can sustain the TID load specified by the project proposal. The expected dose for the RU, including a safety factor, is about 10 krad in 4 years. The FPGA was irradiated with 30 MeV protons (energy at the target) in steps. In each step, the chip was irradiated for the given time with a defined flux intensity. The chip was powered and working during the irradiation — the SEU testing circuit was running in it. The beam was stopped and programming functionality was tested

after each irradiation period. The chip was powered off for 5 seconds at the beginning of the programming test, afterwards it was powered on again and reprogrammed. If the programming ended successfully, irradiation continued with the next step. Otherwise, the irradiation was stopped. Because a relatively expensive device is permanently damaged after the test, only two M2GL010T FPGA chips were tested.

The first Igloo2 chip was irradiated with the proton flux of $10^7 \text{ cm}^{-2} \text{ s}^{-1}$, corresponding to the dose rate 3 rad/s. Each irradiation step took 6 minutes, corresponding to 1 krad dose. After the first step, the programming was already not working. The ability of the chip to be programmed was tested approximately each 2 or 3 days after the irradiation. The programming become possible again after 30 days. The irradiation continued three months after the first irradiation, when the chip seemed to be working normally again. The flux was significantly lower this time — $4.4 \times 10^5 \text{ cm}^{-2} \text{ s}^{-1}$, corresponding to the dose rate of 0.15 rad/s and the step was approximately 0.25–0.5 krad (30–60 minutes). The flux and the dose time flow are shown in Fig. 5.10. The programming failed after 3.5 krad. The quoted dose includes also the dose accumulated in the first irradiation. Partial recovery was observed after three weeks, when about $1/4$ of the programming attempts were successful and the rest failed. Complete recovery was never achieved and after another week all programming attempts were failing.

The second Igloo2 chip was irradiated by protons with the low dose rate (0.15 rad/s) from the beginning. The step was again ≈ 0.25 krad. The first programming failure was observed at 4.4 krad and the chip recovered in 10 minutes. After that, the irradiation continued up to 5.4 krad, when the programming failed to work completely. A recovery was observed 21 days after the irradiation. The irradiation continued with the same parameters of the dose rate three months later. The programming failure was observed at 6.4 krad (quoted dose includes again the dose from the first irradiation) and another successful attempt to program was after 30 minutes without the beam. Then the irradiation continued up to 7.9 krad, after which the chip has never recovered and was not able to be programmed even 18 months after the irradiation. The flux and the dose time flow are shown in Fig. 5.11.

Figure 5.12 shows the time flow of the TID and flux for the flash-based **ProASIC3** chip for comparison. No programming error was observed for this chip at least up to ≈ 10 krad. The chip was then used for different experiments, during which it obtained over 200 krad of TID with quite high dose rate up to 200 rad/s. After such dose it failed to work completely.

5.1.4 Discussion of Results from FPGA Measurements

The results of our measurements show, that gamma rays from ^{60}Co do not cause single event effects in SRAM FPGAs. We were able to give just the upper limits on the cross section.

We obtained a similar size of SEE cross sections for protons and neutrons which have the similar mean energy. That might indicate, that the significant source of SEEs are nuclear reactions and the secondary ionization caused by products of these reactions. Such conclusion is supported also by comparing SEE cross sections obtained for protons with

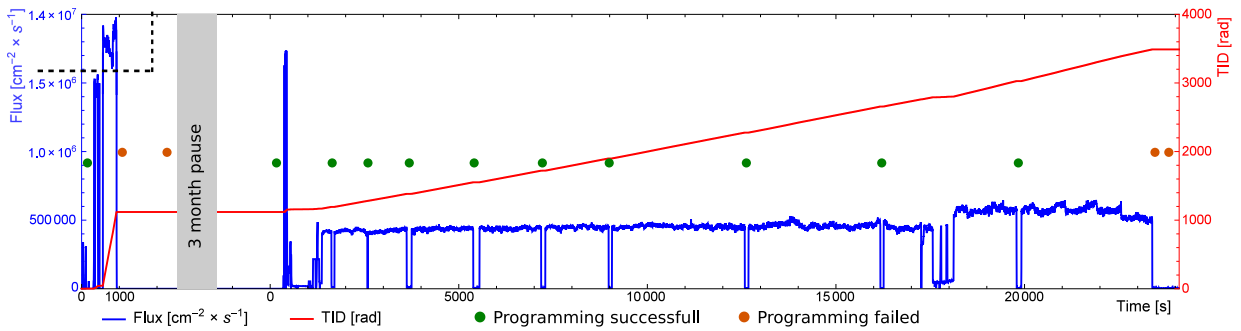


Figure 5.10: Time flow of the TID accumulated in the first tested Igloo2 (M2GL010T) chip and the corresponding proton flux. Dots illustrate programming attempts. Mind the adjusted flux axis in the top left corner.

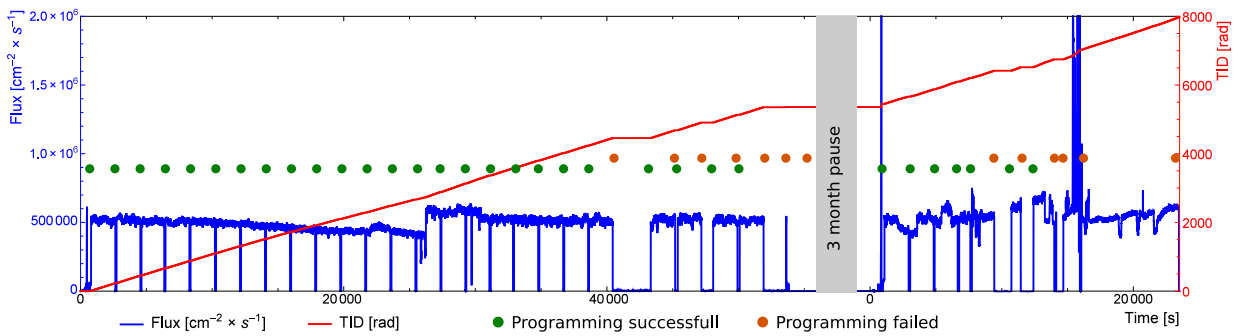


Figure 5.11: Time flow of the TID accumulated in the second tested Igloo2 (M2GL010T) chip and the corresponding proton flux. Dots illustrate programming attempts.

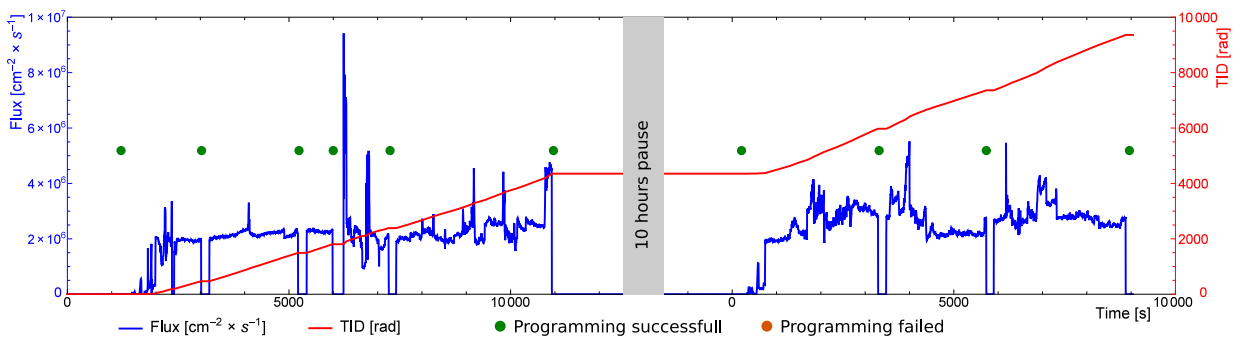


Figure 5.12: Time flow of the TID accumulated in the tested ProASIC3 (M1A3P1000L) chip and the corresponding proton flux. Dots illustrate programming attempts.

different stopping power (different energy). It can be seen from Figure 5.13, that protons which ionize more (i.e. have lower energy and bigger stopping power dE/dx) have the SEE cross section lower than protons which ionize less (i.e. have bigger energy and lower dE/dx). Cross section data for flash-based FPGA in the Tab. 5.2 also support this observation.

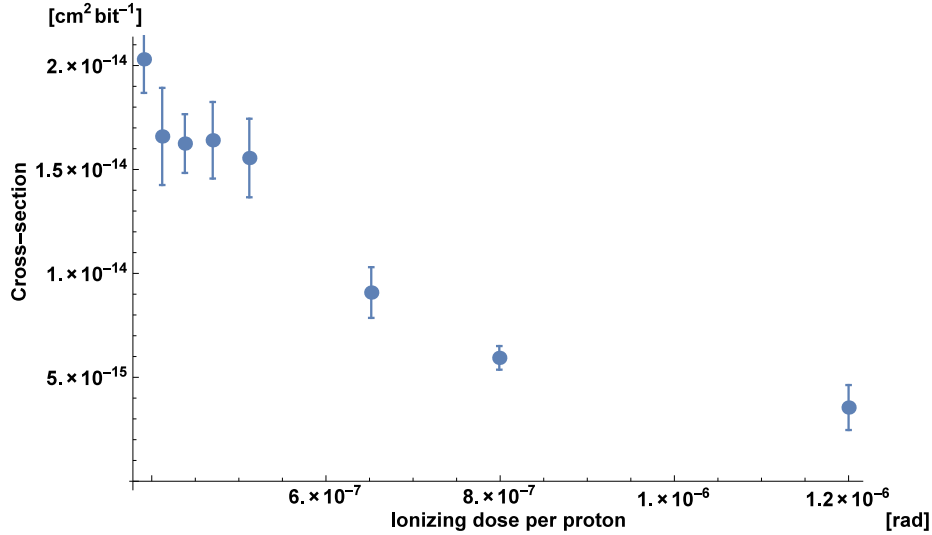


Figure 5.13: Dependence of SEE in configuration memory of XC3S200 on the ionizing dose delivered by a single proton.

Average SEE cross section in configuration memory of logic block for Spartan-3 for neutrons > 10 MeV published by Xilinx in [78] is $2.87 \times 10^{-14} \text{ cm}^2 \text{ bit}^{-1}$. The values we measured using protons is in the range from 5×10^{-15} to $2 \times 10^{-14} \text{ cm}^2 \text{ bit}^{-1}$ depending on energy. Since the used particle energy spectrum was different, the values are not directly comparable, but are very close.

We can say, based on the data shown in Fig. 5.9, that the variation of SEE cross section for different clock phase shifts is not significant enough to use clock phase alignment with the beam as a SEE mitigation technique. There are just hints of possible dependence (lower cross section at $\approx 170^\circ$ and higher at $\approx 330^\circ$), but more measurements would be necessary to reach necessary statistical significance and to confirm it.

Although only two measurements of the TID damage effects were done on the same flash-based FPGA Igloo2 chip because of too big costs of the tests, we can say that the dose resistance of the flash-based device depends not only on the total dose, but also on the dose rate. The higher the dose rate is, the lower is the TID threshold when the chip fails. The coarse estimate is that for ≈ 2 orders less flux we can achieve ≈ 4 times higher dose until the programming fails. The same behavior of the programming ability was observed also on other flash-based devices (SmartFusion2 and ProASIC3) during other tests, but the exact dose was not measured in that case.

It should be noted that none of the tested chips was specified as a radiation-tolerant device.

5.2 ITS Readout Unit Tests

A first prototype of the RU board (RUv0) was already built at CERN to test the concept of the design and to test radiation hardness of critical components. The RUv0 board was subsequently tested at NPI cyclotron. The tests and a comparison of soft error mitigation techniques and securing the design on different levels is described in [A.1] and is still ongoing. Testing of optical transceivers is described in [A.2].

Our measurements of TID hardness of FPGAs helped to select the final version of FPGA to be used in the RU of the upgraded ITS and also the design techniques used for fault mitigation. The RU will use the high-performance SRAM-based Kintex-7 for data processing together with the low-performance, yet enough radiation tolerant, flash-based ProASIC3 as a circuit supervising the function of the RU and scrubbing the Kintex-7 configuration memory [109].

The proton SEU cross sections measured on RUv0 equipped with Kintex-7 (KC7325T) at the NPI cyclotron equals $3.07 \times 10^{-15} \text{ cm}^2 \text{ bit}^{-1}$. The value is consistent with other tests of this chip carried out at different facilities [83]. However the results are not directly comparable, since different particles and different energies were used.

The developed beam dosimetry and experience gained during previous experiments was used also during the radiation tests of other components for ITS Upgrade project, like cables, conductive glue and ALPIDE chips.

5.3 ALPIDE Measurements

The cyclotron and the elaborated beam monitoring and dosimetry system was used also for characterization measurements of prototypes of the ALPIDE chips. The measured data contributed to the development of the final version of the detector chip and investigation of its properties using proton beam [110].

5.3.1 Delay Scan

Besides TID hardness studies we performed a measurement of time dependence of a signal generated in the chip by incoming 30 MeV protons. The measurements were performed on the 3rd prototype version of the chip, pALPIDE-3, which was the last prototype before the mass production. The pixel matrix of this prototype version was divided into 8 sectors of the same size, each utilizing a different circuit design and its layout on the silicon. The sectors were arranged in adjacent columns of equal width (128 pixels) and height (512 pixels). The goal of the measurement was to compare the charge collection time in these segments. The new ITS requires that sensors have as low charge collection time as possible, so the trace of a particle does not overlap with hits from subsequent events. Results of the measurement were used as a basis for a decision on the selection of layout used for the final chip.

5. DEPENDABILITY AND CHARACTERIZATION MEASUREMENTS



Figure 5.14: 3rd prototype version of the ALPIDE chip placed on a carrier board. On the left-hand side is a front view of the carrier board with the chip bonded in the middle of it. On the right-hand side, there is the back side of the same carrier board with a technological hole in it, located under a part of the chip. The hole was utilized for measuring false proton hits (see text for details).

The chip was placed on the carrier board shown in Fig. 5.14. Behind the chip, a scintillator with a PMT registering incoming protons was placed. The signal from the PMT was optionally delayed using a function generator and sent to the chip as a trigger signal for data acquisition, see Fig. 5.15. The proton flux was decreased down to $\approx 100 \text{ cm}^{-2} \text{ s}^{-1}$, so that only one proton is captured in each frame. Due to a high noise in the scintillator and PMT, the PMT gain had to be set as low as possible to prevent the output saturation with amplified noise and only protons with high energy were registered. The circuit board carrying the ALPIDE chip had a technological hole below the upper part of the chip, as it can be seen in Fig. 5.14. The bottom part of the chip was overlapping with the circuit board from behind. Protons passing through the board lost a large part of their energy and their signal from the scintillator was below the threshold. Thus the trigger signal was issued only for protons, passing through the upper half of the ALPIDE chip, see Fig. 5.16. Based on this, it was possible to estimate also the contribution of proton clusters from events with false trigger signal. We can see in Fig. 5.17, that for the lowest delay and after tuning the PMT gain and threshold levels, we captured predominantly protons passing through the hole. The number of protons registered in the bottom part of the chip increases with increasing delay of the data acquisition trigger. These are considered as false coincidence and we can assume, that the same amount of false proton hits was also in the upper part.

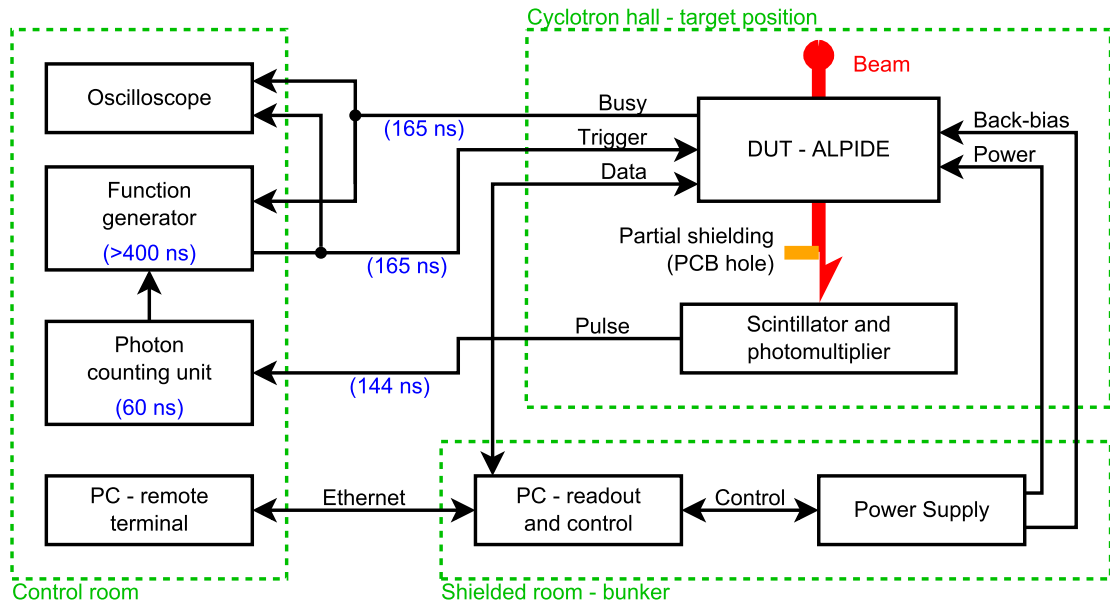


Figure 5.15: Schematic connection of the setup for the ALPIDE delay scan. Signal delays on individual cables and components are marked in blue. The minimal delay between registering the proton by PMT and receiving the trigger signal by ALPIDE is ≈ 780 ns and can be increased at the function generator. The standard dosimetry and positioning equipment and its connection is not shown and can be found in Fig. 4.1.

A statistical correction was performed to eliminate them [111], cf. Fig. 5.16.

The mean number of pixels in a proton cluster in different sectors as a function of trigger signal delay is presented in Fig. 5.18. Only events with a single proton hit in the full chip area were selected for data analysis. Data for analysis of each sector were further selected only from events, where all pixels of the proton cluster were located within the area of the given sector.

We can see from the measured data that there are differences between various sectors. Pixels in the fastest sectors 6 and 7 collect the charge released by 30 MeV proton in about $6\ \mu\text{s}$, while in sectors 0 and 1 the same charge is collected in more than $9\ \mu\text{s}$.

Figure 5.19 presents several examples of proton clusters for a given sector and delay. The fading of pixels in the center of the cluster earlier than of those at the edge is caused by a shaping circuit that initiates a reset if too much charge is being collected in one pixel for a long time. The shaping circuit is one of the used techniques to shorten the readout time and its different design was one of the variations among the eight different sectors on the prototype version of the ALPIDE chip.

5. DEPENDABILITY AND CHARACTERIZATION MEASUREMENTS

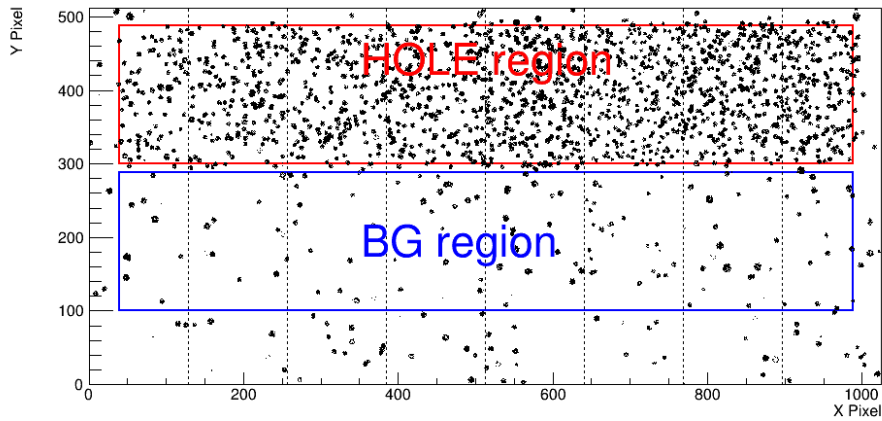


Figure 5.16: Definition of the HOLE region where the chip registers contributions from signal and background clusters and the BG region dominated by contributions from background clusters. The background component of measured data is removed on statistical basis, by subtracting the corresponding distributions in BG region from the HOLE region. Source: [A.9].

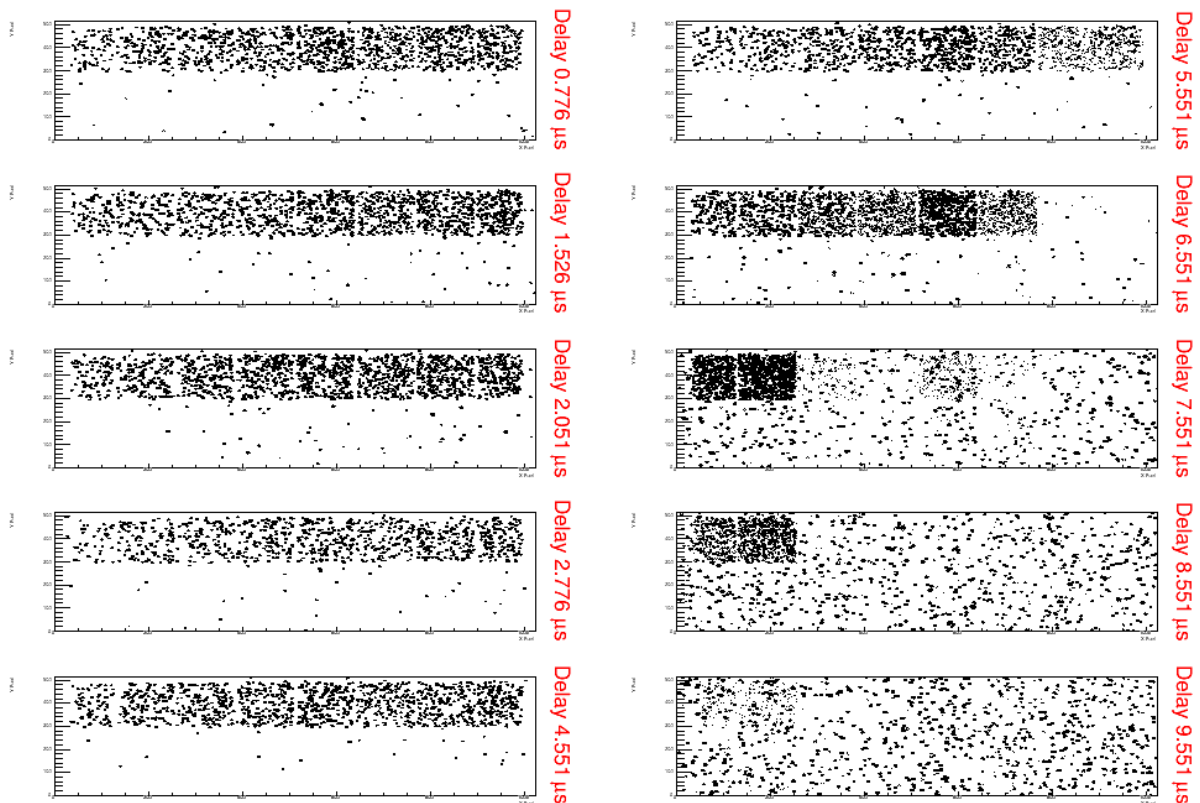


Figure 5.17: Example distribution of the clusters across the chip for different delays between the PMT trigger signal and the start of data acquisition. The visible borders between sectors are created artificially by the selection of events where there is only one cluster per chip area and all pixels of that cluster are located in one sector only. Source: [A.9].

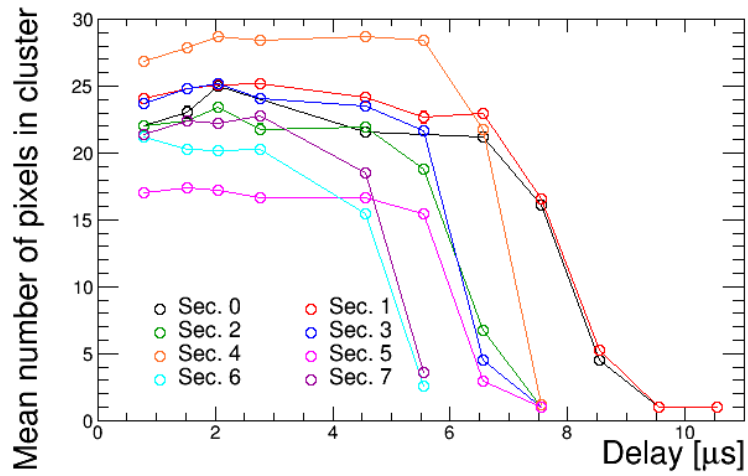


Figure 5.18: Mean number of pixels in cluster versus the delay between the PMT trigger signal and the start of data acquisition. Source: [A.9].



Figure 5.19: Typical proton clusters for each sector and different delay between the PMT trigger signal and the start of data acquisition. Source: [A.9].

Conclusions

Radiation hardness tests of various electronic components are important parts of engineering and scientific projects in the fields of space research, aviation, nuclear and particle physics and many others. With a continuously decreasing dimensions of electronic chip technology, the sensitivity to the effects caused by ionizing radiation increases, although based on the ever increasing understanding of these effects the techniques to mitigate them are also improving. This ensures the importance of radiation hardness tests and this field of the research also for the future.

I worked on the extensions of the existing infrastructure available in the Nuclear Physics Institute within my dissertation thesis, so that it is usable for the purposes of testing radiation hardness of electronic components for the ALICE Inner Tracking System (ITS) Upgrade project. This primarily required to provide an on-line monitoring of the beam and the dosimetry, which allowed to study the evolving properties of tested components under exactly defined beam conditions. Within this effort I focused on controlling the beam parameters like flux and profile. A number of measurements required very low fluxes in the order of tens or hundreds of protons per second per cm^2 . In the cooperation with cyclotron operators and engineers, we elaborated procedures and methods to reach such stable conditions. In addition, I promoted the construction of the energy degrader unit with integrated beam stop, which allows very fast change of the beam energy and immediate stop and restart of the beam, both with the possibility of external and computer automated control. The NPI U-120M cyclotron now offers a better and more convenient environment for operation in low proton flux regimes, which widens the range of possible experiments and can be appreciated also by other users.

A method of detecting faults and measuring a single event effects (SEE) cross section in a configuration memory and flip-flops of any FPGA using accelerated life testing (ALT) was developed and used for characterization of the radiation hardness of programmable hardware. It is based on a special firmware design, that utilizes maximum of the FPGA fabric resources and is sensitive to all bit flips in used configuration memory and in all flip-flops storing the data. The method is usable for any FPGA and gives results equivalent to other methods.

It was clearly demonstrated, that the direct proton ionization up to 30 MeV does not have a significant effect on the probability of causing a SEE in 90 nm technology FPGA. The main contribution to SEE probability is the ability of proton to induce a nuclear reaction in the chip material with reaction products of lower energies causing the high ionization. Therefore in first approximation, proton SEE cross section is very approximately equivalent to SEE cross section of neutron with the same mean energy. Although the used particle energy range was limited to 30 MeV, the statement is valid also for higher energies since the effect of direct proton ionization is most significant for lowest proton energy.

It was also confirmed, that the configuration memory of flash-based FPGAs is resistant to SEE in the used proton energy range, but the chips are more sensitive to the effects of total dose. While the SRAM-based FPGAs were operational after obtaining hundreds of krads, the flash-based ones were failing after several krads or tens of krads. The manifestation of the failure in all cases was the loss of the reprogramming ability. However, the design loaded in the chip was working correctly until an attempt to reprogram it was made.

The extended NPI U-120M cyclotron infrastructure and SEE measurement methods were used to characterize candidate FPGAs for the new readout unit of the upgraded ITS of the ALICE experiment in CERN and helped to choose the optimal one. The project currently focuses on the architecture of the readout unit (RU) in which the high-performance SRAM-based Kintex-7 will be used for data processing together with the low-performance yet enough radiation tolerant flash-based ProASIC3 as a circuit supervising the function of the RU and scrubbing the Kintex-7 configuration memory. As the final specification of the RU is coming out and first firmware designs are being developed, the particular fault-tolerant design techniques and their application on different levels of the circuit are currently being tested and evaluated.

The infrastructure was also extensively used for testing and characterization of the new silicon pixel sensors which will be used in the upgraded ITS. These measurements provided information on radiation hardness and timing characteristics of the chip and confirmed that it meets the requirements given in the project proposal. Other radiation hardness measurements involved for example studies of material degradation, dependability of transmission over fast signal cables during their aging, degradation of conductive glue or measurement of bit error rate of optical transceivers.

6.1 Contributions of the Dissertation Thesis

The main contributions of the dissertation thesis can be summarized as follows:

- An architecture of the system for measuring single event effects cross section in FPGAs was developed. The system can be used for any FPGA and can measure SEE cross section separately for the configuration memory and D-flip-flops. These characteristics of FPGA are useful for developers of fault-tolerant systems, especially in radiation environment. Published in [A.5, A.6, A.7].

- A beam monitoring system for on-line measurement of low proton fluxes at the NPI cyclotron was developed, cross-calibrated using set of different techniques and verified by simulation for energies, being used at the cyclotron. The system can be used also for measurements with neutrons from the Fast Neutron Generator (FNG). Published in [A.4].
- Experiments to verify both the dosimetry system and the FPGA SEE detection architecture were carried out at the NPI cyclotron, FNG and gamma source.
- Comparison of the behavior of FPGAs based on different technologies in radiation environment was made. Published in [A.11].
- Comparison of the SEE cross section for different particles and their interaction mechanisms was made. Published in [A.3].
- Developed systems and methods helped to characterize and select the suitable components and technologies for the new ITS detector of the ALICE experiment. Published in [A.1, A.2, A.9].

6.2 Future Work

The author of the dissertation thesis suggests to explore the following:

- Measure more precisely the SEE cross section in FPGA for different phase shifts of the clock signal and incoming proton bunches and try to identify the possible correlation.
- Characterize the ability of flash-based FPGAs to be programmed as a function of a dose rate, characterize the annealing process and compare the results for different FPGAs and technologies. The measurement would be however costly, since the measured FPGA is permanently damaged and a considerable number of them has to be used to obtain a statistically significant data sample. Nevertheless, it might be possible to perform these measurements also on the standalone flash memory chips made with comparable technology which might deliver equivalent results.

Bibliography

- [1] Evans, L. R.; Bryant, P. “LHC Machine”. *Journal of Instrumentation*, volume 3, 2008: p. S08001. 164 p, this report is an abridged version of the LHC Design Report (CERN-2004-003). Available from: <https://cds.cern.ch/record/1129806>
- [2] The ALICE Collaboration. “Technical Design Report for the Upgrade of the ALICE Inner Tracking System”. Technical report CERN-LHCC-2013-024. ALICE-TDR-017, CERN, Nov 2013. Available from: <https://cds.cern.ch/record/1625842>
- [3] The ALICE Collaboration. “The ALICE experiment at the CERN LHC”. *Journal of Instrumentation*, volume 3, 2008: p. S08002. 259 p, also published by CERN Geneva in 2010. Available from: <https://cds.cern.ch/record/1129812>
- [4] Moore, A. “*FPGAs for Dummies*”. John Wiley and Sons, 2014, ISBN 978-1-118-94220-8.
- [5] Xilinx. “*Field Programmable Gate Array (FPGA)*”. Available from: <https://www.xilinx.com/training/fpga/fpga-field-programmable-gate-array.htm>
- [6] Kuon, I.; Tessier, R.; Rose, J. “FPGA Architecture: Survey and Challenges”. *Foundations and Trends in Electronic Design Automation*, volume 2, no. 2, 2007: p. 135253.
- [7] Microsemi (Actel). “*ProASIC3 FPGA Fabric Users Guide*”. Available from: <http://www.microsemi.com/>
- [8] IEEE. “*1149.7-2009 - IEEE Standard for Reduced-Pin and Enhanced-Functionality Test Access Port and Boundary-Scan Architecture*”. IEEE Standard 1149.7 (JTAG).
- [9] Garey, M. R.; Johnson, D. S. “*Computers and Intractability; A Guide to the Theory of NP-Completeness*”. New York, NY, USA: W. H. Freeman & Co., 1990, ISBN 0716710455.

- [10] Xilinx. “*Partial Reconfiguration User Guide*”. v12.1 edition, 2010. Available from: https://www.xilinx.com/support/documentation/sw_manuals/xilinx12_1/ug702.pdf
- [11] Guterman, D. C.; Rimawi, I. H.; Chiu, T.-L.; et al. “An electrically alterable non-volatile memory cell using a floating-gate structure”. *IEEE Transactions on Electron Devices*, volume 26, no. 4, Apr 1979: pp. 576–586, ISSN 0018-9383, doi: 10.1109/T-ED.1979.19462.
- [12] Speers, T.; Wang, J. J.; Cronquist, B.; et al. “0.25 μm FLASH Memory Based FPGA for Space Applications”. Available from: <http://www.actel.com/documents/FlashSpaceApps.pdf>
- [13] Carlson, I.; Andersson, S.; Natarajan, S.; et al. “A high density, low leakage, 5T SRAM for embedded caches”. In *Proceedings of the 30th European Solid-State Circuits Conference*, Sept 2004, pp. 215–218, doi:10.1109/ESSCIR.2004.1356656.
- [14] Hamdy, E.; McCollum, J.; Chen, S. O.; et al. “Dielectric based antifuse for logic and memory ICs”. In *Technical Digest., International Electron Devices Meeting*, Dec 1988, ISSN 0163-1918, pp. 786–789, doi:10.1109/IEDM.1988.32929.
- [15] Microsemi (Actel). “*SX Family FPGAs*”. Available from: <http://www.microsemi.com/>
- [16] Jandl, J.; Petr, I. “*Ionizující záření v životním prostředí*”. Populární přednášky o fyzice, SNTL, 1988.
- [17] Olive, K. A.; Agashe, K.; Amsler, C.; et al. “Review of Particle Physics, 2014-2015. Review of Particle Properties”. *Chin. Phys. C*, volume 38, 2014: p. 090001. Available from: <https://cds.cern.ch/record/1753419>
- [18] NIST, Physical Measurement Laboratory. “Stopping Power and Range Tables for Electrons”. Online. Available from: <http://physics.nist.gov/PhysRefData/Star/Text/ESTAR.html>
- [19] NIST, Physical Measurement Laboratory. “Stopping Power and Range Tables for Protons”. Online. Available from: <http://physics.nist.gov/PhysRefData/Star/Text/PSTAR.html>
- [20] Ziegler, J.; Ziegler, M.; Biersack, J. “SRIM - The stopping and range of ions in matter (2010)”. *Nuclear Instruments and Methods in Physics Research Section B 268*, 2010.
- [21] Wagenaar, D. J. “Radiation Physics Principles”. 1995. Available from: <http://www.med.harvard.edu/jpnm/physics/nmltd/radprin/main.html>
- [22] Jiř i. V. “Radioaktivita.cz — Detekce ionizujícího záření”. Available from: <http://www.radioaktivita.cz/jednotky.html>

-
- [23] Leroy, C.; Rancoita, P. “*Principles of Radiation Interaction in Matter*”. World Scientific, 2009.
- [24] Bethe, H. A.; Low, F.; Watson, K. M.; et al. “Theoretical calculations of pion-nucleon scattering”. In *3rd Annual Rochester Conference on High Energy Nuclear Physics (ICHEP 52 - Rochester)*, 1953, p. 74–88.
- [25] Newhauser, W. D.; Zhang, R. “The physics of proton therapy”. *Physics in Medicine and Biology*, volume 60, no. 8, 2015: p. R155. Available from: <http://stacks.iop.org/0031-9155/60/i=8/a=R155>
- [26] Baumann, R. C. “Radiation-induced soft errors in advanced semiconductor technologies”. *IEEE Transactions on Device and Materials Reliability*, volume 5, no. 3, Sept 2005: pp. 305–316, ISSN 1530-4388, doi:10.1109/TDMR.2005.853449.
- [27] Kvasnička, J. “*Reliability Analysis of SRAM-based Field-Programmable Gate Arrays*”. Dissertation thesis, Faculty of Information Technology, Czech Technical University in Prague, August 2013.
- [28] Messenger, G. C. “Collection of Charge on Junction Nodes from Ion Tracks”. *IEEE Transactions on Nuclear Science*, volume 29, no. 6, Dec 1982: pp. 2024–2031, ISSN 0018-9499, doi:10.1109/TNS.1982.4336490.
- [29] Ferlet-Cavrois, V.; Massengill, L. W.; Gouker, P. “Single Event Transients in Digital CMOS - A Review”. *IEEE Transactions on Nuclear Science*, volume 60, no. 3, June 2013: pp. 1767–1790, ISSN 0018-9499, doi:10.1109/TNS.2013.2255624.
- [30] Reed, R. A.; Carts, M. A.; Marshall, P. W.; et al. “Heavy ion and proton-induced single event multiple upset”. *IEEE Transactions on Nuclear Science*, volume 44, no. 6, Dec 1997: pp. 2224–2229, ISSN 0018-9499, doi:10.1109/23.659039.
- [31] Oldham, T. R.; McLean, F. B. “Total ionizing dose effects in MOS oxides and devices”. *IEEE Transactions on Nuclear Science*, volume 50, no. 3, June 2003: pp. 483–499, ISSN 0018-9499, doi:10.1109/TNS.2003.812927.
- [32] Agostinelli, S.; Allison, J.; Amako, K.; et al. “Geant4a simulation toolkit”. *Nuclear Instruments and Methods in Physics Research Section A: Accelerators, Spectrometers, Detectors and Associated Equipment*, volume 506, no. 3, 2003: pp. 250 – 303, ISSN 0168-9002, doi:[http://dx.doi.org/10.1016/S0168-9002\(03\)01368-8](http://dx.doi.org/10.1016/S0168-9002(03)01368-8). Available from: <http://www.sciencedirect.com/science/article/pii/S0168900203013688>
- [33] Holmes-Siedle, A. G.; Adams, L. “*Handbook of radiation effects*”. Oxford University Press, second edition edition, 2002.

- [34] Schrimpf, R. D.; Fleetwood, D. M. “Radiation effects and soft errors in integrated circuits and electronic devices”. Selected topics in electronics and systems, Hackensack, NJ: World Scientific, 2004. Available from: <https://cds.cern.ch/record/1701628>
- [35] Srour, J. R.; Marshall, C. J.; Marshall, P. W. “Review of displacement damage effects in silicon devices”. *IEEE Transactions on Nuclear Science*, volume 50, no. 3, June 2003: pp. 653–670, ISSN 0018-9499, doi:10.1109/TNS.2003.813197.
- [36] Vasilescu, A.; Lindstroem, G. “Displacement damage in silicon”. on-line compilation. Available from: <http://rd50.web.cern.ch/RD50/NIEL/default.html>
- [37] ASTM. “Standard Practice for Characterizing Neutron Fluence Spectra in Terms of an Equivalent Monoenergetic Neutron Fluence for Radiation-Hardness Testing of Electronics”. ASTM Standard E722-14.
- [38] Shuryak, E. V. “Quantum chromodynamics and the theory of superdense matter”. *Physics Reports*, volume 61, no. 2, 1980: pp. 71 – 158, ISSN 0370-1573, doi:10.1016/0370-1573(80)90105-2. Available from: <http://www.sciencedirect.com/science/article/pii/0370157380901052>
- [39] Collins, J. C.; Perry, M. J. “Superdense Matter: Neutrons or Asymptotically Free Quarks?”. *Phys. Rev. Lett.*, volume 34, May 1975: pp. 1353–1356, doi:10.1103/PhysRevLett.34.1353. Available from: <http://link.aps.org/doi/10.1103/PhysRevLett.34.1353>
- [40] The ALICE Collaboration. “Upgrade of the ALICE Experiment: Letter Of Intent”. Technical report CERN-LHCC-2012-012. LHCC-I-022. ALICE-UG-002, CERN, Geneva, Aug 2012. Available from: <https://cds.cern.ch/record/1475243>
- [41] Mager, M. “ALPIDE, the Monolithic Active Pixel Sensor for the ALICE ITS upgrade”. *Nuclear Instruments and Methods in Physics Research Section A: Accelerators, Spectrometers, Detectors and Associated Equipment*, volume 824, 2016: pp. 434 – 438, ISSN 0168-9002, doi:10.1016/j.nima.2015.09.057, frontier Detectors for Frontier Physics: Proceedings of the 13th Pisa Meeting on Advanced Detectors. Available from: <http://www.sciencedirect.com/science/article/pii/S0168900215011122>
- [42] TowerJazz. “TowerJazz CMOS Image Sensor Technology”. Available from: <http://www.jazzsemi.com/cmos-image-sensor.html>
- [43] Buncic, P.; Krzewicki, M.; Vande Vyvre, P. “Technical Design Report for the Upgrade of the Online-Offline Computing System”. Technical report CERN-LHCC-2015-006. ALICE-TDR-019, CERN, Apr 2015. Available from: <https://cds.cern.ch/record/2011297>

-
- [44] Štursa, J.; Bejšovec, V.; Borková, A.; et al. “The Axial Injection System of the Isochronous Cyclotron”. In *Proceedings of the 3rd European Particle Accelerator Conference*, Berlin, Germany, 1992, p. 1513.
- [45] Čihák, M.; Lacman, J.; Štursa, J. “New Control System for the Isochronous Cyclotron U-120M”. In *Proceedings of the 15th International Conference on Cyclotrons and their Applications*, Caen, France, 1998, p. 567.
- [46] Štursa, J.; Čihák, M.; Křivánek, M.; et al. “New Radionuclides Production on the Isochronous Cyclotron U-120M”. In *Proceedings of the 15th International Conference on Cyclotrons and their Applications*, Caen, France, 1998, p. 108.
- [47] CANAM. “Center of Accelerators and Nuclear Analytical Methods, Nuclear Physics Institute of the CAS”. Available from: <http://canam.ujf.cas.cz/>
- [48] Wikipedia. “Cyclotron”. Available from: <https://en.wikipedia.org/wiki/Cyclotron>
- [49] Lawrence, E. O. “Method and apparatus for the acceleration of ions”. US Patent 1,948,384, February 1934.
- [50] Matlocha, T. “*Návrh Urychlovací Elektrody Izochronního Cyklotronu*”. Master’s thesis, Czech Technical University in Prague, Faculty of Electrical Engineering, 2006.
- [51] Schmidt, C. W. “Review of Negative Hydrogen Ion Sources”. In *Proceedings of the Linear Accelerator Conference 1990*, Albuquerque, New Mexico, USA, 1990, p. 14.
- [52] Matlocha, T. “Ion Source for a Single Particle Accelerator”. In *Šimáně 2016 — Czecho-Slovak Student Conference on Nuclear Engineering*, volume 4, edited by V. Caha; M. Cesnek; A. Kecek; M. Ševeček; M. Štefánik, Czech Technical University in Prague, 2016, ISBN 978-80-01-06069-8, pp. 50–55.
- [53] Štefánik, M.; Bem, P.; Gotz, M.; et al. “High-flux white neutron source based on p(35)-Be reactions for activation experiments at NPI”. *Radiation Physics and Chemistry*, volume 104, 2014: pp. 306 – 309, ISSN 0969-806X, doi:<http://dx.doi.org/10.1016/j.radphyschem.2014.06.009>, 1st International Conference on Dosimetry and its Applications. Available from: <http://www.sciencedirect.com/science/article/pii/S0969806X14002576>
- [54] Štefánik, M. “*Experimental Determination of Accelerator-Driven Neutron Generators Spectra*”. Dissertation thesis, Czech Technical University in Prague, Faculty of Nuclear Sciences and Physical Engineering, Department of Nuclear Reactors, 2015.
- [55] PTW. “*User Manual — Ionization Chamber Type 30010, 30011, 30012, 30013*”. Freiburg, Germany, 09 2006.

- [56] Llopart, X.; Ballabriga, R.; Campbell, M.; et al. “Timepix, a 65k programmable pixel readout chip for arrival time, energy and/or photon counting measurements”. *Nuclear Instruments and Methods in Physics Research Section A* 581, 2007.
- [57] Kraus, V.; Holik, M.; Jakubek, J.; et al. “FITPix fast interface for Timepix pixel detectors”. *Journal of Instrumentation*, volume 6, no. 01, 2011: p. C01079. Available from: <http://stacks.iop.org/1748-0221/6/i=01/a=C01079>
- [58] Musílek, L. “Úvod do fyziky ionizujícího záření”. Populární přednášky o fyzice, SNTL, 1979.
- [59] PTW. “User Manual — UNIDOS E - Universal dosemeter”. Freiburg, Germany, 08 2012, type 10008, Type 10009, Type 10010, firmware 1.1 or higher.
- [60] TSL. “The Svedberg Laboratory”. Available from: <http://www.tsl.uu.se/>
- [61] PSI. “Paul Scherrer Institute”. Available from: <https://www.psi.ch/>
- [62] Merl, R.; Gallegos, F.; Pillai, C.; et al. “A multiwire proportional chamber system for monitoring low momentum beam in accelerators”. In *Proceedings of the 2003 Particle Accelerator Conference*, volume 4, May 2003, ISSN 1063-3928, pp. 2515–2517 vol.4, doi:10.1109/PAC.2003.1289172.
- [63] Lin, S.; Boehringer, T.; Coray, A.; et al. “More than 10 years experience of beam monitoring with the Gantry 1 spot scanning proton therapy facility at PSI”. *Medical Physics*, volume 36, no. 11, 2009: pp. 5331–5340, ISSN 2473-4209, doi:10.1118/1.3244034. Available from: <http://dx.doi.org/10.1118/1.3244034>
- [64] Basile, E.; Carloni, A.; Castelluccio, D. M.; et al. “An online proton beam monitor for cancer therapy based on ionization chambers with micro pattern readout”. *Journal of Instrumentation*, volume 7, no. 03, 2012: p. C03020. Available from: <http://stacks.iop.org/1748-0221/7/i=03/a=C03020>
- [65] Medin, J.; Andreo, P.; Grusell, E.; et al. “Ionization chamber dosimetry of proton beams using cylindrical and plane parallel chambers. N w versus N K ion chamber calibrations”. *Physics in Medicine and Biology*, volume 40, no. 7, 1995: p. 1161. Available from: <http://stacks.iop.org/0031-9155/40/i=7/a=002>
- [66] Berkeley Accelerator Space Effects (BASE). “88-Inch Cyclotron”. Available from: <http://user88.lbl.gov/base-rad-effects/protons>
- [67] Wady, P.; Draude, A.; Shubeita, S.; et al. “Accelerated radiation damage test facility using a 5 {MV} tandem ion accelerator”. *Nuclear Instruments and Methods in Physics Research Section A: Accelerators, Spectrometers, Detectors and Associated Equipment*, volume 806, 2016: pp. 109 – 116, ISSN 0168-9002, doi:<http://dx.doi.org/10.1016/j.nima.2015.09.088>. Available from: <http://www.sciencedirect.com/science/article/pii/S0168900215011596>

- [68] Cyclotron Institute, Texas A&M University. “Radiation Effects Facility”. Available from: <http://cyclotron.tamu.edu/ref/>
- [69] Cambria, R.; Hrault, J.; Brassart, N.; et al. “Proton beam dosimetry: A comparison between the Faraday cup and an ionization chamber”. *Physics in Medicine and Biology*, volume 42, no. 6, 1997: p. 1185. Available from: <http://stacks.iop.org/0031-9155/42/i=6/a=014>
- [70] Grusell, E.; Isacson, U.; Montelius, A.; et al. “Faraday cup dosimetry in a proton therapy beam without collimation”. *Physics in Medicine and Biology*, volume 40, no. 11, 1995: p. 1831. Available from: <http://stacks.iop.org/0031-9155/40/i=11/a=005>
- [71] Wyss, J.; Bisello, D.; Pantano, D. “SIRAD: an irradiation facility at the {LNL} Tandem accelerator for radiation damage studies on semiconductor detectors and electronic devices and systems”. *Nuclear Instruments and Methods in Physics Research Section A: Accelerators, Spectrometers, Detectors and Associated Equipment*, volume 462, no. 3, 2001: pp. 426 – 434, ISSN 0168-9002, doi:[http://dx.doi.org/10.1016/S0168-9002\(01\)00193-0](http://dx.doi.org/10.1016/S0168-9002(01)00193-0). Available from: <http://www.sciencedirect.com/science/article/pii/S0168900201001930>
- [72] Glaser, M.; Ravotti, F.; Moll, M. “Dosimetry Assessments in the Irradiation Facilities at the CERN-PS Accelerator”. In *2005 8th European Conference on Radiation and Its Effects on Components and Systems*, Sept 2005, ISSN 0379-6566, pp. PI5-1–PI5-7, doi:10.1109/RADECS.2005.4365632.
- [73] Dervan, P.; French, R.; Hodgson, P.; et al. “The Birmingham Irradiation Facility”. *Nuclear Instruments and Methods in Physics Research Section A: Accelerators, Spectrometers, Detectors and Associated Equipment*, volume 730, 2013: pp. 101 – 104, ISSN 0168-9002, doi:<http://dx.doi.org/10.1016/j.nima.2013.05.156>. Available from: <http://www.sciencedirect.com/science/article/pii/S0168900213007675>
- [74] Kopecký, P. “Proton beam monitoring via the Cu(p, x) 58Co, 63Cu(p, 2n) 62Zn and 65Cu(p, n) 65Zn reactions in copper”. *The International Journal of Applied Radiation and Isotopes*, volume 36, no. 8, 1985: pp. 657 – 661, ISSN 0020-708X, doi:[http://dx.doi.org/10.1016/0020-708X\(85\)90008-0](http://dx.doi.org/10.1016/0020-708X(85)90008-0). Available from: <http://www.sciencedirect.com/science/article/pii/0020708X85900080>
- [75] Karlsruhe Institute of Technology (KIT). “Institute of Experimental Nuclear Physics (IKEP)”. Available from: <http://www.ekp.kit.edu/english/264.php>
- [76] Mountain, R.; Gui, B.; Wang, J.; et al. “FPGA Irradiation at NPTC-MGH”. LHCb Electronics Upgrade Meeting, 10/14/2010.
- [77] Barbero, S. M.; Hoffgen, S. K.; Berger, G.; et al. “Compendium of International Irradiation Test Facilities”. RADECS 2011, Sevilla Spain, 2011. Available

- from: <https://twiki.cern.ch/twiki/pub/FPGARadTol/InformationOfInterest/IrradiationFacilitiesCatalogueRADECS2011.pdf>
- [78] Lesea, A.; Drimer, S.; Fabula, J. J.; et al. “The rosetta experiment: atmospheric soft error rate testing in differing technology FPGAs”. *IEEE Transactions on Device and Materials Reliability*, volume 5, no. 3, Sept 2005: pp. 317–328, ISSN 1530-4388, doi:10.1109/TDMR.2005.854207.
- [79] Rezzak, N.; Wang, J.-J.; Dsilva, D.; et al. “TID and SEE characterization of Microsemi 4th generation radiation tolerant RTG4 flash-based FPGA”. Technical report, Microsemi, 2015.
- [80] iRoC. “Radiation Results of the SER Test of Actel, Xilinx and Altera FPGA instances”. Available from: http://www.microsemi.com/document-portal/doc_download/131628-radresultsirocreport
- [81] Swift, G. M. “Virtex-Ii Static SEU Characterization”. Technical report, Jet Propulsion Laboratory, California Institute of Technology, Jan 2004. Available from: https://parts.jpl.nasa.gov/wp-content/uploads/virtex2_0104-11.pdf
- [82] Hiemstra, D. M.; Chayab, F.; Szajek, L. “Dynamic single event upset characterization of the Virtex-II and Spartan-3 SRAM field programmable gate arrays using proton irradiation”. In *2004 IEEE Radiation Effects Data Workshop (IEEE Cat. No.04TH8774)*, July 2004, pp. 79–84, doi:10.1109/REDW.2004.1352909.
- [83] Wirthlin, M. J.; Takai, H.; Harding, A. “Soft error rate estimations of the Kintex-7 FPGA within the ATLAS Liquid Argon (LAr) Calorimeter”. *Journal of Instrumentation*, volume 9, no. 01, 2014: p. C01025. Available from: <http://stacks.iop.org/1748-0221/9/i=01/a=C01025>
- [84] Cannon, M.; Wirthlin, M.; Camplani, A.; et al. “Evaluating Xilinx 7 Series GTX Transceivers for Use in High Energy Physics Experiments Through Proton Irradiation”. *IEEE Transactions on Nuclear Science*, volume 62, no. 6, Dec 2015: pp. 2695–2702, ISSN 0018-9499, doi:10.1109/TNS.2015.2497216.
- [85] Lee, D. S.; Wirthlin, M.; Swift, G.; et al. “Single-Event Characterization of the 28 nm Xilinx Kintex-7 Field-Programmable Gate Array under Heavy Ion Irradiation”. In *2014 IEEE Radiation Effects Data Workshop (REDW)*, July 2014, ISSN 2154-0519, pp. 1–5, doi:10.1109/REDW.2014.7004595.
- [86] Roed, K.; Alme, J.; Fehlker, D.; et al. “Radiation tolerance of an SRAM based FPGA used in a large tracking detector”. *PoS*, volume RD09, 2009: p. 043.
- [87] Frber, C.; Uwer, U.; Wiedner, D.; et al. “Radiation tolerance tests of SRAM-based FPGAs for the potential usage in the readout electronics for the LHCb experiment”. *Journal of Instrumentation*, volume 9, no. 02, 2014: p. C02028. Available from: <http://stacks.iop.org/1748-0221/9/i=02/a=C02028>

- [88] Vink, W.; Pellegrino, A. “LHCb: FPGA-based, radiation-tolerant on-detector electronics for the upgrade of the LHCb Outer Tracker Detector”. Sep 2013. Available from: <https://cds.cern.ch/record/1603672>
- [89] Hlavička, J.; Racek, S.; Golan, P.; et al. “Číslicové systémy odolné proti poruchám”. ČVUT, 1992, ISBN 80-01-00852-5.
- [90] Czajkowski, D. R.; Samudrala, P. K.; Pagey, M. P. “SEU mitigation for reconfigurable FPGAs”. In *2006 IEEE Aerospace Conference*, 2006, ISSN 1095-323X, pp. 7 pp.–, doi:10.1109/AERO.2006.1655957.
- [91] Xilinx. “*Soft Error Mitigation Controller*”. v4.1 edition, 2015. Available from: https://www.xilinx.com/support/documentation/ip_documentation/sem/v4_1/pg036_sem.pdf
- [92] Bagnato, A.; Indrusiak, L. S.; Quadri, I. R.; et al. “*Handbook of Research on Embedded Systems Design*”. Hershey, PA, USA: IGI Global, 2014, ISBN 1466661941, 9781466661943.
- [93] Borecký, J.; Kohlík, M.; Vít, P.; et al. “Enhanced Duplication Method with TMR-Like Masking Abilities”. In *2016 Euromicro Conference on Digital System Design (DSD)*, Limassol, Cyprus, 2016, ISBN 978-1-5090-2817-7, pp. 690–693.
- [94] Lang. “MCL”. Available from: <http://www.lang.de/product-overview/automation-systems/positioning-systems/mcl.html>
- [95] Rybáček, T. “*System for collecting and analyzing data from radiation measurements*”. Master’s thesis, Czech Technical University in Prague, Faculty of Information Technology, 2016.
- [96] Brun, R.; Rademakers, F. “ROOT - An Object Oriented Data Analysis Framework”. In *New computing techniques in physics research V. Proceedings, 5th International Workshop, AIHENP '96, Lausanne, Switzerland, September 2-6, 1996*, volume A389, 1997, pp. 81–86, doi:10.1016/S0168-9002(97)00048-X. Available from: <http://root.cern.ch/>
- [97] Vysoká, K. “*Low Proton Flux Measurements at the U-120M Cyclotron for Radiation Hardness Studies*”. Master’s thesis, Czech Technical University in Prague, Faculty of Nuclear Sciences and Physical Engineering, 2016.
- [98] PTW. “PTW website”. Available from: <http://www.ptw.de/>
- [99] Tabachová, Z.; Raskina, V. private communication and presentations at technical meetings in Řež. 2015, NPI summer students.
- [100] Microsemi. “*Packaging FAQs*”. June 2011. Available from: http://www.microsemi.com/document-portal/doc_view/130761-packagefaq

BIBLIOGRAPHY

- [101] Strait, L. “Thermo-Mechanical Fatigue of Polymer Matrix Composites”. Technical report, The Pennsylvania State University, Applied Research Lab., 1994. Available from: <http://www.dtic.mil/dtic/tr/fulltext/u2/a285931.pdf>
- [102] Gray, F. “Pulse code communication”. Mar. 17 1953, uS Patent 2,632,058. Available from: <https://www.google.com/patents/US2632058>
- [103] Xilinx. “*Device Reliability Report*”. v10.5.1 edition, 2016. Available from: http://www.xilinx.com/support/documentation/user_guides/ug116.pdf
- [104] Digilent inc. “Digilent website”. Available from: <http://www.digilentinc.com/>
- [105] Keysight Technologies. “Keysight (Agilent) website”. Available from: <http://www.keysight.com/>
- [106] Čihák, M. private communication. 2016, NPI cyclotron engineer and developer.
- [107] Microsemi. “*SmartFusion2 SoC FPGA Family and IGLOO2 FPGA Family*”. Available from: <http://www.microsemi.com/>
- [108] Zhao, C.; Red, K.; Alme, J.; et al. “First irradiation tests results of the ALICE TPC Readout Control Unit 2”. *Journal of Instrumentation*, volume 10, no. 01, 2015: p. C01016. Available from: <http://stacks.iop.org/1748-0221/10/i=01/a=C01016>
- [109] Sielewicz, K. M. “Report on radiation testing of the FPGA”. Technical report, ALICE coloboration, 2017. Available from: https://indico.cern.ch/event/580057/contributions/2357424/attachments/1397071/2136157/fpga_rad_report.pdf
- [110] ALICE coloboration. “ITS Upgrade - Pixel Chip Production Readiness Review”. 2016. Available from: <https://indico.cern.ch/event/576906/>
- [111] Křížek, F. private communication. 2015, 2016, NPI researcher.

Reviewed Publications of the Author Relevant to the Thesis

- [A.1] Sielewicz, K. M.; Rinella, G. A.; Bonora, M.; Ferencei, J.; Giubilato, P.; Rossewij, M. J.; Schambach, J.; Vaňát T. “Prototype readout electronics for the upgraded ALICE Inner Tracking System”. In *Journal of Instrumentation*, volume 12, no. 01, 2017: p. C01008. doi:10.1088/1748-0221/12/01/C01008, ISSN: 1748-0221 Available from: <http://stacks.iop.org/1748-0221/12/i=01/a=C01008>
- [A.2] Schambach, J.; Rossewij, M.; Sielewicz, K. M.; Rinella, G. A.; Bonora, M.; Ferencei, J.; Giubilato, P.; Vaňát T. “ALICE inner tracking system readout electronics prototype testing with the CERN “Giga Bit Transceiver””. In *Journal of Instrumentation*, volume 11, no. 12, 2016: p. C12074. doi:10.1088/1748-0221/11/12/C12074, ISSN: 1748-0221 Available from: <http://iopscience.iop.org/article/10.1088/1748-0221/11/12/C12074>
- [A.3] Vaňát, T.; Křížek, F.; Ferencei, J.; Kubátová H. “Comparing proton and neutron induced SEU cross section in FPGA”. In *2016 IEEE 19th International Symposium on Design and Diagnostics of Electronic Circuits Systems (DDECS)*, IEEE, April 2016, pp. 1–4, doi:10.1109/DDECS.2016.7482480, ISBN: 978-1-5090-2467-4. Available from: <http://ieeexplore.ieee.org/document/7482480/>
- [A.4] Vaňát, T.; Pospíšil, J.; Křížek, F.; Ferencei, J.; Kubátová H. “A System for Radiation Testing and Physical Fault Injection into the FPGAs and Other Electronics”. In *2015 Euromicro Conference on Digital System Design*, IEEE, Aug 2015, pp. 205–210, doi:10.1109/DSD.2015.98, ISBN: 978-1-4673-8035-5. Available from: <http://ieeexplore.ieee.org/document/7302271/>
- [A.5] Vaňát, T.; Kubátová, H. “System for Radiation Testing of FPGAs”. In *26th International Conference on Architecture of Computing Systems 2013*, VDE VERLAG, Feb 2013, pp. 1–5, ISBN: 978-3-8007-3492-4. Available from: <http://ieeexplore.ieee.org/document/6468874/>

- [A.6] Vaňát, T.; Kubátová, H. “Physical Injection of Errors Into the FPGA”. In *Počítačové architektury & diagnostika*, Bratislava, Slovakia: STU v Bratislave, 2011, ISBN: 978-80-227-3552-0.
- [A.7] Vaňát, T.; Kubátová, H. “Experiments with Physical Error Injection into FPGA Circuits”. In *Proceedings of the Work in Progress Session - DSD 2011*, Oulu, Finland: University of Oulu, 2011, ISBN: 978-3-902457-30-1.
- [A.8] Vaňát, T.; Kubátová, H. “SEU Experiments Using Real FPGAs”. In *POSTER 2011 - 15th International Student Conference on Electrical Engineering*, Prague, Czech Republic: CTU, Faculty of Electrical Engineering, 2011, ISBN: 978-80-01-04806-1.

Remaining Publications of the Author Relevant to the Thesis

- [A.9] Křížek, F.; Vaňát, T.; Ferencei, J.; “Response of pAlpide3 to 30 MeV proton beam”. In *ITS upgrade characterisation meeting*, Geneva, Switzerland: CERN, 4 Feb 2016. Available from: <https://indico.cern.ch/event/493629/>
- [A.10] Pospíšil, J.; Vaňát, T.; Schmidt, J. “Towards Trusted Devices in FPGA by Modeling Radiation Induced Errors – First ALT Results”. In *Joint MEDIAN TRUDEVICE Open Forum*, Amsterdam, The Netherlands, 2014.
- [A.11] Vaňát, T.; Pospíšil, J.; Ferencei, J. “Single Event Upset Characterization of Commercial Grade SRAM and FLASH-based Field Programmable Gate Array Using Proton Irradiation”. In *SEFUW: Space FPGA Users Workshop, 2nd Edition*, Noordwijk, The Netherlands: European Space Research and Technology Centre, 2014.
- [A.12] Pospíšil, J.; Vaňát, T.; Schmidt, J. “Towards Trusted Devices in FPGA by Modeling”. In *Proceedings of the 2nd Prague Embedded Systems Workshop*, 2014, p. 16.
- [A.13] Vaňát, T.; Pospíšil, J.; Schmidt, J. “Towards Trusted Devices in FPGA by Modeling Radiation Induced Errors”. In *The Working Groups meeting of the TRUDEVICE Action*, Freiburg, Germany, 2013.
- [A.14] Vaňát, T.; Pospíšil, J. “Towards Dependable Devices in FPGA”. In *PhD Forum at Biannual European - Latin American Summer School on Design, Test and Reliability*, Tallinn, Estonia, 2013.
- [A.15] Vaňát, T. “*Physical Fault Injection*”. Ph.D. Minimum Thesis, Faculty of Information Technology, Prague, Czech Republic, 2012.

Remaining Publications of the Author

- [A.16] J. Adam *et al.* [ALICE Collaboration], “Flow dominance and factorization of transverse momentum correlations in Pb-Pb collisions at the LHC”. arXiv:1702.02665 [nucl-ex]
- [A.17] D. Adamova *et al.* [ALICE Collaboration], “Azimuthally differential pion femtoscopy in Pb-Pb collisions at $\sqrt{s_{\text{NN}}} = 2.76$ TeV”. arXiv:1702.01612 [nucl-ex]
- [A.18] S. Acharya *et al.* [ALICE Collaboration], “Production of muons from heavy-flavour hadron decays in p-Pb collisions at $\sqrt{s_{\text{NN}}} = 5.02$ TeV”. arXiv:1702.01479 [nucl-ex]
- [A.19] S. Acharya *et al.* [ALICE Collaboration], “Production of π^0 and η mesons up to high transverse momentum in pp collisions at 2.76 TeV”. arXiv:1702.00917 [nucl-ex]
1 citation counted in INSPIRE as of 25 Feb 2017
- [A.20] S. Acharya *et al.* [ALICE Collaboration], “First measurement of jet mass in Pb-Pb and p-Pb collisions at the LHC”. arXiv:1702.00804 [nucl-ex]
- [A.21] S. Acharya *et al.* [ALICE Collaboration], “Measurement of D-meson production at mid-rapidity in pp collisions at $\sqrt{s} = 7$ TeV”. arXiv:1702.00766 [nucl-ex]
- [A.22] S. Acharya *et al.* [ALICE Collaboration], “Energy dependence of forward-rapidity J/ψ and $\psi(2S)$ production in pp collisions at the LHC”. arXiv:1702.00557 [nucl-ex]
1 citation counted in INSPIRE as of 25 Feb 2017
- [A.23] J. Adam *et al.* [ALICE Collaboration], “ $K^*(892)^0$ and $\phi(1020)$ meson production at high transverse momentum in pp and Pb-Pb collisions at $\sqrt{s_{\text{NN}}} = 2.76$ TeV”. arXiv:1702.00555 [nucl-ex]
2 citations counted in INSPIRE as of 25 Feb 2017
- [A.24] D. Adamova *et al.* [ALICE Collaboration], “Production of $\Sigma(1385)^\pm$ and $\Xi(1530)^0$ in p-Pb collisions at $\sqrt{s_{\text{NN}}} = 5.02$ TeV”. arXiv:1701.07797 [nucl-ex]

- [A.25] J. Adam *et al.* [ALICE Collaboration], “Insight into particle production mechanisms via angular correlations of identified particles in pp collisions at $\sqrt{s} = 7$ TeV”. arXiv:1612.08975 [nucl-ex]
- [A.26] J. Adam *et al.* [ALICE Collaboration], “Centrality dependence of the pseudorapidity density distribution for charged particles in Pb-Pb collisions at $\sqrt{s_{NN}} = 5.02$ TeV”. arXiv:1612.08966 [nucl-ex]
- [A.27] J. Adam *et al.* [ALICE Collaboration], “W and Z boson production in p-Pb collisions at $\sqrt{s_{NN}} = 5.02$ TeV”. JHEP **1702**, 077 (2017) doi:10.1007/JHEP02(2017)077 arXiv:1611.03002 [nucl-ex]
2 citations counted in INSPIRE as of 25 Feb 2017
- [A.28] J. Adam *et al.* [ALICE Collaboration], “Determination of the event collision time with the ALICE detector at the LHC”. arXiv:1610.03055 [physics.ins-det]
2 citations counted in INSPIRE as of 25 Feb 2017
- [A.29] J. Adam *et al.* [ALICE Collaboration], “Measurement of the production of high- p_T electrons from heavy-flavour hadron decays in Pb-Pb collisions at $\sqrt{s_{NN}} = 2.76$ TeV”. arXiv:1609.07104 [nucl-ex]
1 citations counted in INSPIRE as of 25 Feb 2017
- [A.30] J. Adam *et al.* [ALICE Collaboration], “Evolution of the longitudinal and azimuthal structure of the near-side jet peak in Pb-Pb collisions at $\sqrt{s_{NN}} = 2.76$ TeV”. arXiv:1609.06667 [nucl-ex]
3 citations counted in INSPIRE as of 25 Feb 2017
- [A.31] J. Adam *et al.* [ALICE Collaboration], “Anomalous evolution of the near-side jet peak shape in Pb-Pb collisions at $\sqrt{s_{NN}} = 2.76$ TeV”. arXiv:1609.06643 [nucl-ex]
2 citations counted in INSPIRE as of 25 Feb 2017
- [A.32] J. Adam *et al.* [ALICE Collaboration], “Measurement of electrons from beauty-hadron decays in p-Pb collisions at $\sqrt{s_{NN}} = 5.02$ TeV and Pb-Pb collisions at $\sqrt{s_{NN}} = 2.76$ TeV”. arXiv:1609.03898 [nucl-ex]
2 citations counted in INSPIRE as of 25 Feb 2017
- [A.33] J. Adam *et al.* [ALICE Collaboration], “Jet-like correlations with neutral pion triggers in pp and central PbPb collisions at 2.76 TeV”. Phys. Lett. B **763**, 238 (2016) doi:10.1016/j.physletb.2016.10.048 arXiv:1608.07201 [nucl-ex]
3 citations counted in INSPIRE as of 25 Feb 2017
- [A.34] J. Adam *et al.* [ALICE Collaboration], “J/ ψ suppression at forward rapidity in Pb-Pb collisions at $\sqrt{s_{NN}} = 5.02$ TeV”. Phys. Lett. B **766**, 212 (2016) doi:10.1016/j.physletb.2016.12.064 arXiv:1606.08197 [nucl-ex]
13 citations counted in INSPIRE as of 25 Feb 2017

- [A.35] J. Adam *et al.* [ALICE Collaboration], “Multiplicity-dependent enhancement of strange and multi-strange hadron production in proton-proton collisions at $\sqrt{s} = 7$ TeV”. arXiv:1606.07424 [nucl-ex]
25 citations counted in INSPIRE as of 25 Feb 2017
- [A.36] J. Adam *et al.* [ALICE Collaboration], “Higher harmonic flow coefficients of identified hadrons in Pb-Pb collisions at $\sqrt{s_{NN}} = 2.76$ TeV”. JHEP **1609**, 164 (2016) doi:10.1007/JHEP09(2016)164 arXiv:1606.06057 [nucl-ex]
10 citations counted in INSPIRE as of 25 Feb 2017
- [A.37] J. Adam *et al.* [ALICE Collaboration], “Elliptic flow of electrons from heavy-flavour hadron decays at mid-rapidity in Pb-Pb collisions at $\sqrt{s_{NN}} = 2.76$ TeV”. JHEP **1609**, 028 (2016) doi:10.1007/JHEP09(2016)028 arXiv:1606.00321 [nucl-ex]
8 citations counted in INSPIRE as of 25 Feb 2017
- [A.38] J. Adam *et al.* [ALICE Collaboration], “D-meson production in p-Pb collisions at $\sqrt{s_{NN}} = 5.02$ TeV and in pp collisions at $\sqrt{s} = 7$ TeV”. Phys. Rev. C **94**, no. 5, 054908 (2016) doi:10.1103/PhysRevC.94.054908 arXiv:1605.07569 [nucl-ex]
- [A.39] J. Adam *et al.* [ALICE Collaboration], “Measurement of azimuthal correlations of D mesons and charged particles in pp collisions at $\sqrt{s} = 7$ TeV and p-Pb collisions at $\sqrt{s_{NN}} = 5.02$ TeV”. arXiv:1605.06963 [nucl-ex]
5 citations counted in INSPIRE as of 25 Feb 2017
- [A.40] J. Adam *et al.* [ALICE Collaboration], “Pseudorapidity dependence of the anisotropic flow of charged particles in Pb-Pb collisions at $\sqrt{s_{NN}} = 2.76$ TeV”. Phys. Lett. B **762**, 376 (2016) doi:10.1016/j.physletb.2016.07.017 arXiv:1605.02035 [nucl-ex]
11 citations counted in INSPIRE as of 25 Feb 2017
- [A.41] J. Adam *et al.* [ALICE Collaboration], “Correlated event-by-event fluctuations of flow harmonics in Pb-Pb collisions at $\sqrt{s_{NN}} = 2.76$ TeV”. Phys. Rev. Lett. **117**, 182301 (2016) doi:10.1103/PhysRevLett.117.182301 arXiv:1604.07663 [nucl-ex]
29 citations counted in INSPIRE as of 25 Feb 2017
- [A.42] J. Adam *et al.* [ALICE Collaboration], “Measurement of transverse energy at midrapidity in Pb-Pb collisions at $\sqrt{s_{NN}} = 2.76$ TeV”. Phys. Rev. C **94**, no. 3, 034903 (2016) doi:10.1103/PhysRevC.94.034903 arXiv:1603.04775 [nucl-ex]
11 citations counted in INSPIRE as of 25 Feb 2017
- [A.43] J. Adam *et al.* [ALICE Collaboration], “Centrality dependence of charged jet production in pPb collisions at $\sqrt{s_{NN}} = 5.02$ TeV”. Eur. Phys. J. C **76**, no. 5, 271 (2016) doi:10.1140/epjc/s10052-016-4107-8 arXiv:1603.03402 [nucl-ex]
7 citations counted in INSPIRE as of 25 Feb 2017

- [A.44] J. Adam *et al.* [ALICE Collaboration], “Centrality dependence of $\psi(2S)$ suppression in p-Pb collisions at $\sqrt{s_{\text{NN}}} = 5.02$ TeV”. JHEP **1606**, 050 (2016) doi:10.1007/JHEP06(2016)050 arXiv:1603.02816 [nucl-ex]
8 citations counted in INSPIRE as of 25 Feb 2017
- [A.45] J. Adam *et al.* [ALICE Collaboration], “Measurement of D-meson production versus multiplicity in p-Pb collisions at $\sqrt{s_{\text{NN}}} = 5.02$ TeV”. JHEP **1608**, 078 (2016) doi:10.1007/JHEP08(2016)078 arXiv:1602.07240 [nucl-ex]
6 citations counted in INSPIRE as of 25 Feb 2017
- [A.46] J. Adam *et al.* [ALICE Collaboration], “Particle identification in ALICE: a Bayesian approach”. Eur. Phys. J. Plus **131**, no. 5, 168 (2016) doi:10.1140/epjp/i2016-16168-5 arXiv:1602.01392 [physics.data-an]
8 citations counted in INSPIRE as of 25 Feb 2017
- [A.47] J. Adam *et al.* [ALICE Collaboration], “Anisotropic flow of charged particles in Pb-Pb collisions at $\sqrt{s_{\text{NN}}} = 5.02$ TeV”. Phys. Rev. Lett. **116**, no. 13, 132302 (2016) doi:10.1103/PhysRevLett.116.132302 arXiv:1602.01119 [nucl-ex]
29 citations counted in INSPIRE as of 25 Feb 2017
- [A.48] J. Adam *et al.* [ALICE Collaboration], “Production of $K^*(892)^0$ and $\phi(1020)$ in pPb collisions at $\sqrt{s_{\text{NN}}} = 5.02$ TeV”. Eur. Phys. J. C **76**, no. 5, 245 (2016) doi:10.1140/epjc/s10052-016-4088-7 arXiv:1601.07868 [nucl-ex]
10 citations counted in INSPIRE as of 25 Feb 2017
- [A.49] J. Adam *et al.* [ALICE Collaboration], “Multiplicity dependence of charged pion, kaon, and (anti)proton production at large transverse momentum in p-Pb collisions at $\sqrt{s_{\text{NN}}} = 5.02$ TeV”. Phys. Lett. B **760**, 720 (2016) doi:10.1016/j.physletb.2016.07.050 arXiv:1601.03658 [nucl-ex]
16 citations counted in INSPIRE as of 25 Feb 2017
- [A.50] J. Adam *et al.* [ALICE Collaboration], “Multipion Bose-Einstein correlations in pp,p -Pb, and Pb-Pb collisions at energies available at the CERN Large Hadron Collider”. Phys. Rev. C **93**, no. 5, 054908 (2016) doi:10.1103/PhysRevC.93.054908 arXiv:1512.08902 [nucl-ex]
6 citations counted in INSPIRE as of 25 Feb 2017
- [A.51] J. Adam *et al.* [ALICE Collaboration], “Multi-strange baryon production in p-Pb collisions at $\sqrt{s_{\text{NN}}} = 5.02$ TeV”. Phys. Lett. B **758**, 389 (2016) doi:10.1016/j.physletb.2016.05.027 arXiv:1512.07227 [nucl-ex]
19 citations counted in INSPIRE as of 25 Feb 2017
- [A.52] J. Adam *et al.* [ALICE Collaboration], “Centrality dependence of the charged-particle multiplicity density at midrapidity in Pb-Pb collisions at $\sqrt{s_{\text{NN}}} = 5.02$ TeV”. Phys. Rev. Lett. **116**, no. 22, 222302 (2016) doi:10.1103/

- PhysRevLett.116.222302 arXiv:1512.06104 [nucl-ex]
 37 citations counted in INSPIRE as of 25 Feb 2017
- [A.53] J. Adam *et al.* [ALICE Collaboration], “Charge-dependent flow and the search for the chiral magnetic wave in Pb-Pb collisions at $\sqrt{s_{NN}} = 2.76$ TeV”. Phys. Rev. C **93**, no. 4, 044903 (2016) doi:10.1103/PhysRevC.93.044903 arXiv:1512.05739 [nucl-ex]
 15 citations counted in INSPIRE as of 25 Feb 2017
- [A.54] J. Adam *et al.* [ALICE Collaboration], “Measurement of an excess in the yield of J/ψ at very low p_T in Pb-Pb collisions at $\sqrt{s_{NN}} = 2.76$ TeV”. Phys. Rev. Lett. **116**, no. 22, 222301 (2016) doi:10.1103/PhysRevLett.116.222301 arXiv:1509.08802 [nucl-ex]
 18 citations counted in INSPIRE as of 25 Feb 2017
- [A.55] J. Adam *et al.* [ALICE Collaboration], “Pseudorapidity and transverse-momentum distributions of charged particles in protonproton collisions at $\sqrt{s} = 13$ TeV”. Phys. Lett. B **753**, 319 (2016) doi:10.1016/j.physletb.2015.12.030 arXiv:1509.08734 [nucl-ex]
 26 citations counted in INSPIRE as of 25 Feb 2017
- [A.56] J. Adam *et al.* [ALICE Collaboration], “Inclusive quarkonium production at forward rapidity in pp collisions at $\sqrt{s} = 8$ TeV”. Eur. Phys. J. C **76**, no. 4, 184 (2016) doi:10.1140/epjc/s10052-016-3987-y arXiv:1509.08258 [nucl-ex]
 9 citations counted in INSPIRE as of 25 Feb 2017
- [A.57] J. Adam *et al.* [ALICE Collaboration], “Charged-particle multiplicities in proton-proton collisions at $\sqrt{s} = 0.9$ to 8 TeV”. Eur. Phys. J. C **77**, no. 1, 33 (2017) doi:10.1140/epjc/s10052-016-4571-1 arXiv:1509.07541 [nucl-ex]
 24 citations counted in INSPIRE as of 25 Feb 2017
- [A.58] J. Adam *et al.* [ALICE Collaboration], “Measurement of electrons from heavy-flavour hadron decays in p-Pb collisions at $\sqrt{s_{NN}} = 5.02$ TeV”. Phys. Lett. B **754**, 81 (2016) doi:10.1016/j.physletb.2015.12.067 arXiv:1509.07491 [nucl-ex]
 20 citations counted in INSPIRE as of 25 Feb 2017
- [A.59] J. Adam *et al.* [ALICE Collaboration], “Azimuthal anisotropy of charged jet production in $\sqrt{s_{NN}} = 2.76$ TeV Pb-Pb collisions”. Phys. Lett. B **753**, 511 (2016) doi:10.1016/j.physletb.2015.12.047 arXiv:1509.07334 [nucl-ex]
 10 citations counted in INSPIRE as of 25 Feb 2017
- [A.60] J. Adam *et al.* [ALICE Collaboration], “Direct photon production in Pb-Pb collisions at $\sqrt{s_{NN}} = 2.76$ TeV”. Phys. Lett. B **754**, 235 (2016) doi:10.1016/j.physletb.2016.01.020 arXiv:1509.07324 [nucl-ex]
 49 citations counted in INSPIRE as of 25 Feb 2017

- [A.61] J. Adam *et al.* [ALICE Collaboration], “Centrality evolution of the charged-particle pseudorapidity density over a broad pseudorapidity range in Pb-Pb collisions at $\sqrt{s_{\text{NN}}} = 2.76$ TeV”. *Phys. Lett. B* **754**, 373 (2016) doi:10.1016/j.physletb.2015.12.082 arXiv:1509.07299 [nucl-ex]
8 citations counted in INSPIRE as of 25 Feb 2017
- [A.62] J. Adam *et al.* [ALICE Collaboration], “Measurement of D_s^+ production and nuclear modification factor in Pb-Pb collisions at $\sqrt{s_{\text{NN}}} = 2.76$ TeV”. *JHEP* **1603**, 082 (2016) doi:10.1007/JHEP03(2016)082 arXiv:1509.07287 [nucl-ex]
25 citations counted in INSPIRE as of 25 Feb 2017
- [A.63] J. Adam *et al.* [ALICE Collaboration], “Multiplicity and transverse momentum evolution of charge-dependent correlations in pp, pPb, and PbPb collisions at the LHC”. *Eur. Phys. J. C* **76**, no. 2, 86 (2016) doi:10.1140/epjc/s10052-016-3915-1 arXiv:1509.07255 [nucl-ex]
7 citations counted in INSPIRE as of 25 Feb 2017
- [A.64] J. Adam *et al.* [ALICE Collaboration], “Transverse momentum dependence of D-meson production in Pb-Pb collisions at $\sqrt{s_{\text{NN}}} = 2.76$ TeV”. *JHEP* **1603**, 081 (2016) doi:10.1007/JHEP03(2016)081 arXiv:1509.06888 [nucl-ex]
63 citations counted in INSPIRE as of 25 Feb 2017
- [A.65] J. Adam *et al.* [ALICE Collaboration], “Coherent $\psi(2S)$ photo-production in ultra-peripheral Pb Pb collisions at $\sqrt{s_{\text{NN}}} = 2.76$ TeV”. *Phys. Lett. B* **751**, 358 (2015) doi:10.1016/j.physletb.2015.10.040 arXiv:1508.05076 [nucl-ex]
14 citations counted in INSPIRE as of 25 Feb 2017
- [A.66] J. Adam *et al.* [ALICE Collaboration], “Precision measurement of the mass difference between light nuclei and anti-nuclei”. *Nature Phys.* **11**, no. 10, 811 (2015) doi:10.1038/nphys3432 arXiv:1508.03986 [nucl-ex]
12 citations counted in INSPIRE as of 25 Feb 2017
- [A.67] J. Adam *et al.* [ALICE Collaboration], “Study of cosmic ray events with high muon multiplicity using the ALICE detector at the CERN Large Hadron Collider”. *JCAP* **1601**, no. 01, 032 (2016) doi:10.1088/1475-7516/2016/01/032 arXiv:1507.07577 [astro-ph.HE]
7 citations counted in INSPIRE as of 25 Feb 2017
- [A.68] J. Adam *et al.* [ALICE Collaboration], “Centrality dependence of pion freeze-out radii in Pb-Pb collisions at $\sqrt{s_{\text{NN}}} = 2.76$ TeV”. *Phys. Rev. C* **93**, no. 2, 024905 (2016) doi:10.1103/PhysRevC.93.024905 arXiv:1507.06842 [nucl-ex]
13 citations counted in INSPIRE as of 25 Feb 2017
- [A.69] J. Adam *et al.* [ALICE Collaboration], “Event shape engineering for inclusive spectra and elliptic flow in Pb-Pb collisions at $\sqrt{s_{\text{NN}}} = 2.76$ TeV”. *Phys. Rev. C* **93**, no.

- 3, 034916 (2016) doi:10.1103/PhysRevC.93.034916 arXiv:1507.06194 [nucl-ex]
 14 citations counted in INSPIRE as of 25 Feb 2017
- [A.70] J. Adam *et al.* [ALICE Collaboration], “Elliptic flow of muons from heavy-flavour hadron decays at forward rapidity in PbPb collisions at $\sqrt{s_{\text{NN}}} = 2.76$ TeV”. Phys. Lett. B **753**, 41 (2016) doi:10.1016/j.physletb.2015.11.059 arXiv:1507.03134 [nucl-ex]
 20 citations counted in INSPIRE as of 25 Feb 2017
- [A.71] J. Adam *et al.* [ALICE Collaboration], “Production of light nuclei and anti-nuclei in pp and Pb-Pb collisions at energies available at the CERN Large Hadron Collider”. Phys. Rev. C **93**, no. 2, 024917 (2016) doi:10.1103/PhysRevC.93.024917 arXiv:1506.08951 [nucl-ex]
 35 citations counted in INSPIRE as of 25 Feb 2017
- [A.72] J. Adam *et al.* [ALICE Collaboration], “ ϕ -meson production at forward rapidity in p-Pb collisions at $\sqrt{s_{\text{NN}}} = 5.02$ TeV and in pp collisions at $\sqrt{s} = 2.76$ TeV”. doi:10.1016/j.physletb.2017.01.074 arXiv:1506.09206 [nucl-ex]
 13 citations counted in INSPIRE as of 25 Feb 2017
- [A.73] J. Adam *et al.* [ALICE Collaboration], “Centrality dependence of inclusive J/ψ production in p-Pb collisions at $\sqrt{s_{\text{NN}}} = 5.02$ TeV”. JHEP **1511**, 127 (2015) doi:10.1007/JHEP11(2015)127 arXiv:1506.08808 [nucl-ex]
 32 citations counted in INSPIRE as of 25 Feb 2017
- [A.74] J. Adam *et al.* [ALICE Collaboration], “Differential studies of inclusive J/ψ and $\psi(2S)$ production at forward rapidity in Pb-Pb collisions at $\sqrt{s_{\text{NN}}} = 2.76$ TeV”. JHEP **1605**, 179 (2016) doi:10.1007/JHEP05(2016)179 arXiv:1506.08804 [nucl-ex]
 38 citations counted in INSPIRE as of 25 Feb 2017
- [A.75] J. Adam *et al.* [ALICE Collaboration], “ ${}^3_{\Lambda}\text{H}$ and ${}^3_{\Lambda}\bar{\text{H}}$ production in Pb-Pb collisions at $\sqrt{s_{\text{NN}}} = 2.76$ TeV”. Phys. Lett. B **754**, 360 (2016) doi:10.1016/j.physletb.2016.01.040 arXiv:1506.08453 [nucl-ex]
 27 citations counted in INSPIRE as of 25 Feb 2017
- [A.76] J. Adam *et al.* [ALICE Collaboration], “Forward-central two-particle correlations in p-Pb collisions at $\sqrt{s_{\text{NN}}} = 5.02$ TeV”. Phys. Lett. B **753**, 126 (2016) doi:10.1016/j.physletb.2015.12.010 arXiv:1506.08032 [nucl-ex]
 27 citations counted in INSPIRE as of 25 Feb 2017
- [A.77] J. Adam *et al.* [ALICE Collaboration], “One-dimensional pion, kaon, and proton femtoscopy in Pb-Pb collisions at $\sqrt{s_{\text{NN}}} = 2.76$ TeV”. Phys. Rev. C **92**, no. 5, 054908 (2015) doi:10.1103/PhysRevC.92.054908 arXiv:1506.07884 [nucl-ex]
 15 citations counted in INSPIRE as of 25 Feb 2017

- [A.78] J. Adam *et al.* [ALICE Collaboration], “Search for weakly decaying $\bar{\Lambda}n$ and $\Lambda\Lambda$ exotic bound states in central Pb-Pb collisions at $\sqrt{s_{NN}} = 2.76$ TeV”. *Phys. Lett. B* **752**, 267 (2016) doi:10.1016/j.physletb.2015.11.048 arXiv:1506.07499 [nucl-ex]
18 citations counted in INSPIRE as of 25 Feb 2017
- [A.79] J. Adam *et al.* [ALICE Collaboration], “Centrality dependence of the nuclear modification factor of charged pions, kaons, and protons in Pb-Pb collisions at $\sqrt{s_{NN}} = 2.76$ TeV”. *Phys. Rev. C* **93**, no. 3, 034913 (2016) doi:10.1103/PhysRevC.93.034913 arXiv:1506.07287 [nucl-ex]
28 citations counted in INSPIRE as of 25 Feb 2017
- [A.80] J. Adam *et al.* [ALICE Collaboration], “Centrality dependence of high- p_T D meson suppression in Pb-Pb collisions at $\sqrt{s_{NN}} = 2.76$ TeV”. *JHEP* **1511**, 205 (2015) doi:10.1007/JHEP11(2015)205 arXiv:1506.06604 [nucl-ex]
40 citations counted in INSPIRE as of 25 Feb 2017
- [A.81] J. Adam *et al.* [ALICE Collaboration], “Measurement of jet quenching with semi-inclusive hadron-jet distributions in central Pb-Pb collisions at $\sqrt{s_{NN}} = 2.76$ TeV”. *JHEP* **1509**, 170 (2015) doi:10.1007/JHEP09(2015)170 arXiv:1506.03984 [nucl-ex]
34 citations counted in INSPIRE as of 25 Feb 2017
- [A.82] J. Adam *et al.* [ALICE Collaboration], “Measurement of charm and beauty production at central rapidity versus charged-particle multiplicity in proton-proton collisions at $\sqrt{s} = 7$ TeV”. *JHEP* **1509**, 148 (2015) doi:10.1007/JHEP09(2015)148 arXiv:1505.00664 [nucl-ex]
32 citations counted in INSPIRE as of 25 Feb 2017
- [A.83] J. Adam *et al.* [ALICE Collaboration], “Inclusive, prompt and non-prompt J/ψ production at mid-rapidity in Pb-Pb collisions at $\sqrt{s_{NN}} = 2.76$ TeV”. *JHEP* **1507**, 051 (2015) doi:10.1007/JHEP07(2015)051 arXiv:1504.07151 [nucl-ex]
40 citations counted in INSPIRE as of 25 Feb 2017
- [A.84] J. Adam *et al.* [ALICE Collaboration], “Measurement of pion, kaon and proton production in protonproton collisions at $\sqrt{s} = 7$ TeV”. *Eur. Phys. J. C* **75**, no. 5, 226 (2015) doi:10.1140/epjc/s10052-015-3422-9 arXiv:1504.00024 [nucl-ex]
36 citations counted in INSPIRE as of 25 Feb 2017
- [A.85] J. Adam *et al.* [ALICE Collaboration], “Coherent ρ^0 photoproduction in ultra-peripheral Pb-Pb collisions at $\sqrt{s_{NN}} = 2.76$ TeV”. *JHEP* **1509**, 095 (2015) doi:10.1007/JHEP09(2015)095 arXiv:1503.09177 [nucl-ex]
21 citations counted in INSPIRE as of 25 Feb 2017
- [A.86] J. Adam *et al.* [ALICE Collaboration], “Rapidity and transverse-momentum dependence of the inclusive J/ψ nuclear modification factor in p-Pb collisions at $\sqrt{s_{NN}} = 5.02$ TeV”. *JHEP* **1506**, 055 (2015) doi:10.1007/JHEP06(2015)055

arXiv:1503.07179 [nucl-ex]

46 citations counted in INSPIRE as of 25 Feb 2017

- [A.87] J. Adam *et al.* [ALICE Collaboration], “Measurement of dijet k_T in pPb collisions at $\sqrt{s_{NN}} = 5.02$ TeV”. *Phys. Lett. B* **746**, 385 (2015) doi:10.1016/j.physletb.2015.05.033 arXiv:1503.03050 [nucl-ex]
12 citations counted in INSPIRE as of 25 Feb 2017
- [A.88] J. Adam *et al.* [ALICE Collaboration], “Measurement of charged jet production cross sections and nuclear modification in p-Pb collisions at $\sqrt{s_{NN}} = 5.02$ TeV”. *Phys. Lett. B* **749**, 68 (2015) doi:10.1016/j.physletb.2015.07.054 arXiv:1503.00681 [nucl-ex]
27 citations counted in INSPIRE as of 25 Feb 2017
- [A.89] J. Adam *et al.* [ALICE Collaboration], “Measurement of jet suppression in central Pb-Pb collisions at $\sqrt{s_{NN}} = 2.76$ TeV”. *Phys. Lett. B* **746**, 1 (2015) doi:10.1016/j.physletb.2015.04.039 arXiv:1502.01689 [nucl-ex]
55 citations counted in INSPIRE as of 25 Feb 2017
- [A.90] J. Adam *et al.* [ALICE Collaboration], “Two-pion femtoscopy in p-Pb collisions at $\sqrt{s_{NN}} = 5.02$ TeV”. *Phys. Rev. C* **91**, 034906 (2015) doi:10.1103/PhysRevC.91.034906 arXiv:1502.00559 [nucl-ex]
22 citations counted in INSPIRE as of 25 Feb 2017
- [A.91] J. Adam *et al.* [ALICE Collaboration], “Forward-backward multiplicity correlations in pp collisions at $\sqrt{s} = 0.9, 2.76$ and 7 TeV”. *JHEP* **1505**, 097 (2015) doi:10.1007/JHEP05(2015)097 arXiv:1502.00230 [nucl-ex]
14 citations counted in INSPIRE as of 25 Feb 2017
- [A.92] J. Adam *et al.* [ALICE Collaboration], “Centrality dependence of particle production in p-Pb collisions at $\sqrt{s_{NN}} = 5.02$ TeV”. *Phys. Rev. C* **91**, no. 6, 064905 (2015) doi:10.1103/PhysRevC.91.064905 arXiv:1412.6828 [nucl-ex]
93 citations counted in INSPIRE as of 25 Feb 2017
- [A.93] B. B. Abelev *et al.* [ALICE Collaboration], “Production of inclusive $\Upsilon(1S)$ and $\Upsilon(2S)$ in p-Pb collisions at $\sqrt{s_{NN}} = 5.02$ TeV”. *Phys. Lett. B* **740**, 105 (2015) doi:10.1016/j.physletb.2014.11.041 arXiv:1410.2234 [nucl-ex]
46 citations counted in INSPIRE as of 25 Feb 2017